

# Renormalizing one-point probability distribution function for cosmological counts in cells

---

Anton Chudaykin<sup>1a,b,c</sup> Mikhail M. Ivanov<sup>2d,e</sup> Sergey Sibiryakov<sup>3a,b</sup>

<sup>a</sup>*Department of Physics & Astronomy, McMaster University,  
1280 Main Street West, Hamilton, ON L8S 4M1, Canada*

<sup>b</sup>*Perimeter Institute for Theoretical Physics, Waterloo, Ontario, N2L 2Y5, Canada*

<sup>c</sup>*Institute for Nuclear Research of the Russian Academy of Sciences,  
60th October Anniversary Prospect, 7a, 117312 Moscow, Russia*

<sup>d</sup>*Center for Theoretical Physics, Massachusetts Institute of Technology,  
Cambridge, MA 02139, USA*

<sup>e</sup>*School of Natural Sciences, Institute for Advanced Study,  
1 Einstein Drive, Princeton, NJ 08540, USA*

**ABSTRACT:** We study the one-point probability distribution function (PDF) for matter density averaged over spherical cells. The leading part to the PDF is defined by spherical collapse dynamics, whereas the next-to-leading part comes from the integration over fluctuations around the saddle-point solution. The latter calculation receives sizable contributions from short modes and must be renormalized. We propose a new approach to renormalization by modeling the effective stress-energy tensor for short perturbations. The model contains three free parameters. Two of them are related to the counterterms in the one-loop matter power spectrum and bispectrum, one more parameterizes their redshift dependence. This relation can be used to impose priors in fitting the model to the PDF data. We confront the model with the results of high-resolution N-body simulations and find excellent agreement for cell radii  $r_* \geq 10 \text{ Mpc}/h$  at all redshifts down to  $z = 0$ . Discrepancies at a few per cent level are detected at low redshifts for  $r_* \leq 10 \text{ Mpc}/h$  and are associated with two-loop corrections to the model.

*Dedicated to the memory of Valery Rubakov, great scientist and teacher.*

---

<sup>1</sup>chudayka@mcmaster.ca

<sup>2</sup>ivanov99@mit.edu

<sup>3</sup>ssibiryakov@perimeterinstitute.ca

---

## Contents

<b>1</b>	<b>Introduction and Summary</b>	<b>1</b>
<b>2</b>	<b>One-Point Probability Distribution Function</b>	<b>4</b>
2.1	Saddle-point expansion	4
2.2	Aspherical prefactor	8
2.3	Contribution of UV modes	10
<b>3</b>	<b>Counterterm prefactor and its relation to correlators</b>	<b>13</b>
<b>4</b>	<b>Counterterm model</b>	<b>17</b>
4.1	Stress tensor in EFT of LSS	17
4.2	Shell-crossing in the background of spherical collapse	21
4.3	Counterterm stress for spherical collapse	25
4.4	Synthesis	27
<b>5</b>	<b>Comparison with N-body data</b>	<b>30</b>
5.1	Large cells	32
5.2	Small cells	36
<b>6</b>	<b>Conclusions</b>	<b>38</b>
<b>A</b>	<b>Conventions</b>	<b>39</b>
<b>B</b>	<b>Spherical PDF</b>	<b>41</b>
<b>C</b>	<b>A fit for the aspherical prefactor</b>	<b>44</b>
<b>D</b>	<b>Dynamical equations</b>	<b>47</b>
D.1	Background evolution	47
D.2	Linearized perturbations with $\ell > 0$	48
D.3	Quadratic perturbations in the monopole sector	49
D.4	Redefining sources for second-order perturbations	51
<b>E</b>	<b>WKB expansion for UV modes</b>	<b>53</b>
E.1	Equations and sources	53
E.2	Evaluation of the $\varkappa$ -integrals	56
<b>F</b>	<b>Alternative estimates of shell-crossing scale</b>	<b>59</b>
<b>G</b>	<b>Sensitivity of the “speed of sound” to cosmology</b>	<b>61</b>

<b>H</b>	<b>Transients from Zeldovich initial conditions</b>	<b>63</b>
<b>I</b>	<b>Reduced models for counterterm prefactor</b>	<b>68</b>

---

## 1 Introduction and Summary

Motivated by the rapid accumulation of observational data, there has been a lot of progress in the analytic modeling of the Large-Scale-Structure (LSS) of the Universe. To a large extent, this progress is associated with the development of the cosmological perturbation theory. The latter is built on a diagrammatic expansion quite similar to that in perturbative quantum field theory. Various cosmological correlators are obtained as a sum of the leading tree-level contribution and corrections ordered by the number of loops in the diagram [1]. An important step was the realization that the loop contributions must be renormalized because they involve unphysical integration over modes with short wavelengths which are beyond the perturbative regime. This renormalization is systematically carried out within the framework of effective field theory (EFT) where the contribution of short modes is accounted for by an effective stress tensor added to the equations of motion for the long modes [2–8]. The effect of short-scale dynamics on the LSS correlators is thereby captured by a few free parameters which are to be fixed from the data. The EFT approach, combined with other developments, such as resummation of large bulk flows [9–12] and FFTLog computation of the loop integrals [13], has been shown to provide an efficient and accurate method for calculation of the LSS power spectrum [14] and bispectrum [15, 16]. It has been implemented in numerical codes [17–19]. Recently, it has been successfully used to extract cosmological parameters from the data [20–35], including analyses with controlled theoretical uncertainty [36–38].

In this paper we go beyond the perturbation theory and consider non-perturbative one-point probability distribution function (PDF), also known as counts-in-cells (CiC) statistics. To define it, one separates the density field in spherical cells of radius  $r_*$  in position space and takes the average value of the density inside each cell.<sup>1</sup> The one-point PDF is then the probability of finding a given average density. It is estimated as the number of cells with this density divided by the total number of cells. Note that the deviation of this averaged density from the mean density of the universe does not need to be small, so evaluation of the PDF requires a non-perturbative treatment.

CiC statistics was introduced by E. Hubble [39] and has been measured in galaxy surveys [40–42]. Related one-point statistics of the matter field have been used in

---

<sup>1</sup>In the case of discrete tracers, one counts the number of objects inside each cell.

the analysis of weak lensing maps [43–45]. The PDF is known to contain information from all  $n$ -point correlation functions in a compressed way [1] and is also sensitive to rare fluctuations. Thus, it is a promising probe of LSS, complementary to the perturbative observables. Combining the PDF with the matter power spectrum can significantly enhance the constraining power on the standard cosmological parameters and the neutrino mass [46], as well as on the extended models of gravity and dark energy [47, 48]. The PDF and its generalizations [49] also provide a promising tool for probing primordial non-Gaussianity [50, 51] and for analyzing future 21cm intensity mapping data [52].

There are several theoretical approaches to PDF modeling. Pioneering studies of the counts-in-cell statistics used perturbative methods [53, 54]. They were extended beyond perturbation theory in Refs. [55, 56] which show that the most probable configuration producing a given averaged density inside a spherical cell respects the symmetry of the problem, i.e. it is given by the spherical collapse. These results were generalized to several concentric cells [57] and interpreted in the context of Large Deviation Principle [58]. Ref. [59] suggested applying the logarithmic transformation of the density field to improve the accuracy of the method. This approach uses the non-linear density variance as an input and has proven to be successful in describing the results of high-resolution simulations, see Refs. [46, 47, 60–62]. An alternative approach to the counts-in-cells statistics was developed in Refs. [63–66] based on the Lagrangian-space description of LSS. This method involves the relation between the initial (Lagrangian) PDF and the physical (Eulerian) PDF that was addressed in Refs. [67–69]. Ref. [70] discusses application of this method to  $(1 + 1)$ -dimensional toy model and convergence of the perturbative series for PDF.

Here we pursue the path-integral approach developed in [71] following earlier works [55, 56]. This approach uses the linear variance of the density field within the cell as an expansion parameter and leads to representation of the PDF in the form similar to the semiclassical expansion of quantum field theory. The PDF factorizes into the leading-order exponential part and a prefactor. The former is given by the spherically symmetric saddle-point configuration that is found exactly using the dynamics of spherical collapse. On the other hand, the next-to-leading prefactor results from integration over fluctuations around the saddle-point solution. A numerical procedure for calculating it was implemented in an open-source Python code AsPy [72].

The prefactor can be thought of as an one-loop contribution in the background of the saddle-point configuration. It receives sizable contribution from short — or ‘ultraviolet’ (UV) — modes and must be renormalized with an appropriate counterterm. Unlike in perturbation theory, this procedure cannot be carried out relying only on the symmetries of the long-distance dynamics. Indeed, these symmetries allow the counterterm to be an arbitrary function of the cell density contrast, thereby destroying the predictive power. Another way to see the problem is to recall that the

PDF aggregates the information about all correlation functions. Within the EFT of LSS, the coefficients of their counterterms are independent, implying that the PDF counterterm contains an infinite number of parameters. In an attempt to overcome this difficulty Ref. [71] proposed two *ad hoc* counterterm models motivated by the structure of the UV contribution into the aspherical prefactor. The models agree with each other at moderate density contrasts, but deviate by 30% at the tails of the distribution which was interpreted as theoretical uncertainty of the method.

The goal of this paper is to refine the counterterm model and put it on firm physical grounds. To this aim, we revisit the calculation of the aspherical prefactor and isolate the contribution of the UV modes. We find that it is described by an effective stress tensor consisting of two physically distinct parts, which we refer to as *kinetic* and *potential*. One corresponds to the pressure of the short modes, and the other to their gravitational pull. We propose that this stress tensor should be renormalized by the counterterm with the same structure, but with additional factors in front of the two contributions controlled by the shell-crossing scale in the background solution. The key physical assumption behind this proposal is that the counterterm is dominated by the modes in a relatively narrow range of wavenumbers which experience the shell crossing, but are not yet virialized.

Approximating the power spectrum at the relevant wavenumbers by a power-law, we can fix the dependence of these factors on time and density. This leaves the model with three free parameters — the coefficients in front of the kinetic and the potential parts of the counterterm and the exponent of the power law describing their time and density dependence. These parameters must be fitted from the data. We show that certain combinations of these parameters can be matched to the EFT counterterms in the one-loop power spectrum and bispectrum. While the former can be reliably measured from the power spectrum of the real or N-body data, measuring the latter requires measurement of the bispectrum and is challenging. Thus, we suggest to restrict the freedom of the PDF model by imposing priors following from the value and the redshift dependence of the power-spectrum counterterm.

We validate our theoretical framework using N-body data from high-resolution Farpoint simulation which evolves  $12288^3$  particles in a  $1 (\text{Gpc}/h)^3$  volume [73]. We find that the model describes the data within their statistical uncertainty for density contrasts  $0.1 \leq 1 + \delta_* \leq 10$ , cell radii<sup>2</sup>  $r_* = 15 \text{ Mpc}/h$  and  $10 \text{ Mpc}/h$  and up to redshift zero. For smaller cell radii  $r_* = 7.5 \text{ Mpc}/h$  and  $5 \text{ Mpc}/h$  we observe small (a few per cent), but significant, discrepancies between the model and the data. We explain that these discrepancies cannot arise from a deficiency of the counterterm model, but represent the first detection of the two-loop corrections to the PDF.

The paper is organized as follows. In Sec. 2 we review the approach to the

---

<sup>2</sup>The parameter  $h \approx 0.7$  is defined through the present-day value of the Hubble constant,  $H_0 = 100 h \text{ km}/(\text{s} \cdot \text{Mpc})$ .

PDF developed in [71], with the focus on the UV contribution to the prefactor. In Sec. 3 we derive the model-independent relations between the PDF counterterm and the counterterms of the  $n$ -point correlators. In Sec. 4 we propose our model for the counterterm stress tensor and compute the resulting counterterm for the PDF prefactor. Section 5 contains comparison to the N-body data. We conclude in Sec. 6.

A number of appendices complement the main text. Appendix A summarizes our conventions. In appendix B we discuss the PDF restricted to spherical configurations and derive its analytic form. Appendix C presents a simple phenomenological fit to the aspherical prefactor and contrasts it with the full theoretical model. Appendix D summarizes the dynamical equations governing the density and velocity perturbations. In appendix E we discuss the Wentzel–Kramers–Brillouin (WKB) approximation for high multipoles. In appendix F we explore alternative definitions of shell-crossing scale in the non-trivial background of the spherical collapse solution. Appendix G explores the sensitivity of the power-spectrum counterterm to the cosmological parameters. Appendix H contains discussion of transients in the N-body PDF due to inaccuracy of the Zeldovich initial conditions. In appendix I we investigate the possibility of fitting PDF with reduced sets of counterterm parameters.

## 2 One-Point Probability Distribution Function

### 2.1 Saddle-point expansion

We consider the density contrast averaged over a spherical cell of radius  $r_*$ ,<sup>3</sup>

$$\bar{\delta}_W = \int \frac{d^3x}{r_*^3} \tilde{W}(r/r_*) \delta(\mathbf{x}) = \int_{\mathbf{k}} W(kr_*) \delta(\mathbf{k}), \quad (2.1)$$

where  $\delta(\mathbf{x}) \equiv \delta\rho(\mathbf{x})/\rho_{\text{univ}}$ , with  $\rho_{\text{univ}}$  being the average matter density of the Universe.  $\tilde{W}(r/r_*)$  is a window function in position space and  $W(kr_*)$  denotes its Fourier counterpart. Generally,  $\tilde{W}$  can be any spherically symmetric function normalized to unity,  $\int d^3z \tilde{W} = 1$ . It is commonly chosen to be top-hat in the literature,

$$\tilde{W}_{\text{th}}(r/r_*) = \frac{3}{4\pi} \Theta_{\text{H}} \left( 1 - \frac{r}{r_*} \right) \iff W_{\text{th}}(kr_*) = \frac{3j_1(kr_*)}{kr_*}, \quad (2.2)$$

where  $\Theta_{\text{H}}$  stands for the Heaviside theta-function. As explained in [71], this choice greatly simplifies the analysis and we adopt it throughout this work.

The initial conditions for the density perturbations are assumed to be adiabatic and Gaussian, so that their statistical properties are entirely described by the two-point correlator,

$$\langle \delta_{\text{in}}(\mathbf{k}) \delta_{\text{in}}(\mathbf{k}') \rangle = (2\pi)^3 \delta_{\text{D}}(\mathbf{k} + \mathbf{k}') g^2(z_{\text{in}}) P(k), \quad (2.3)$$

---

<sup>3</sup>See appendix A for the notations and conventions.

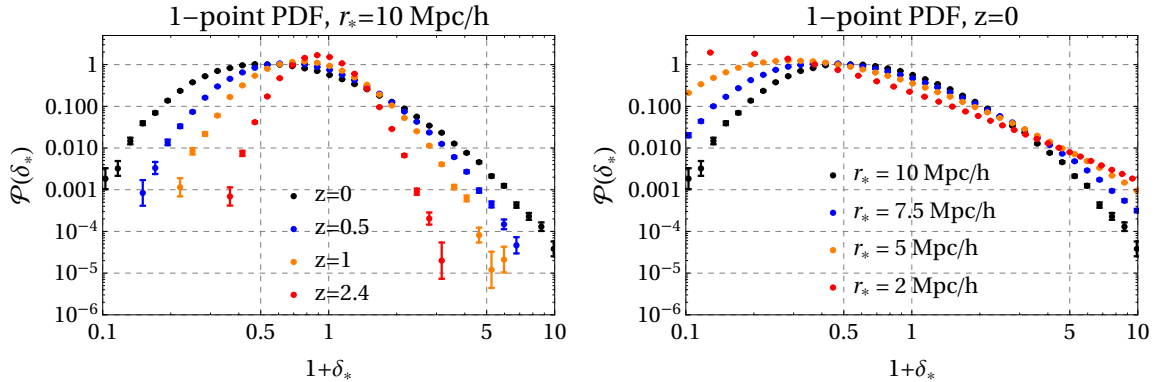


**Figure 1.** The one-point PDF  $\mathcal{P}(\delta_*)$  measured from the N-body data. *Left:*  $\mathcal{P}(\delta_*)$  for several redshifts at fixed comoving cell radius  $r_* = 10 \text{ Mpc}/h$ . *Right:*  $\mathcal{P}(\delta_*)$  for several cell radii at  $z = 0$ . The errorbars show the statistical uncertainties.

where  $\delta_D$  is the Dirac delta-function. Here  $P(k)$  is the linear power spectrum at  $z = 0$ . We also used the linear growth factor  $g(z)$  to translate the  $P(k)$  to the initial redshift  $z_{\text{in}}$ . It is convenient to rescale the initial density field  $\delta_{\text{in}}$  to redshift  $z$  using the linear growth factor,

$$\delta_L(\mathbf{k}, z) = \frac{g(z)}{g(z_{\text{in}})} \delta_{\text{in}}(\mathbf{k}). \quad (2.4)$$

We will refer to  $\delta_L$  as the linear density perturbation in what follows and will omit the redshift-dependence.

The one-point PDF  $\mathcal{P}(\delta_*; z, r_*)$  is defined as the probability to observe  $\bar{\delta}_W$  within a given infinitesimal interval,

$$\mathcal{P}(\delta_*; z, r_*) d\delta_* = \text{Probability}\{\delta_* < \bar{\delta}_W < \delta_* + d\delta_*\}. \quad (2.5)$$

It depends on the redshift  $z$  and the cell radius  $r_*$  as parameters; in what follows we will often suppress these arguments to keep notations concise. Fig. 1 shows PDF measured from data of high-resolution N-body simulation [73].<sup>4</sup> The PDF varies by several orders of magnitude in the density range  $1 + \delta_* \in [0.1, 10]$  and exhibits strong dependence on the redshift and cell radii. This exponential sensitivity is a hallmark of non-perturbative behavior similar to tunneling in quantum theory or large fluctuations in statistical physics and suggests using the saddle-point method which successfully describes the latter phenomena.

The PDF can be evaluated as the functional integral with Gaussian weight over all linear density configurations that produce desired non-linear density contrast at the final time. The latter condition is conveniently imposed by the delta-function inserted into the integration measure,

$$\delta_D(\delta_* - \bar{\delta}_W[\delta_L]) = \int_{-i\infty}^{i\infty} \frac{d\lambda}{2\pi i g^2} \exp\left\{\frac{\lambda}{g^2}(\delta_* - \bar{\delta}_W[\delta_L])\right\}, \quad (2.6)$$

<sup>4</sup>See Sec. 5 for the details of this measurement.

where  $\bar{\delta}_W[\delta_L]$  describes the functional dependence of  $\bar{\delta}_W$  on the linear field. This leads to the following expression [55, 71],

$$\mathcal{P}(\delta_*) = \int_{-i\infty}^{i\infty} \frac{d\lambda}{2\pi i g^2} \exp \left\{ \frac{\lambda \delta_*}{g^2} + w(\lambda) \right\}. \quad (2.7)$$

where the function  $w(\lambda)$  reads

$$w(\lambda) = \ln \left[ \mathcal{N}^{-1} \int \mathcal{D}\delta_L \exp \left\{ -\frac{1}{g^2} \int_{\mathbf{k}} \frac{|\delta_L(\mathbf{k})|^2}{2P(k)} - \frac{\lambda \bar{\delta}_W[\delta_L]}{g^2} \right\} \right], \quad (2.8)$$

and  $\mathcal{N}$  is a normalization factor. Let us first consider high redshifts when the growth factor  $g(z)$  is small. Then the integrals (2.7), (2.8) can be evaluated in the saddle-point approximation. The results reads schematically:

$$\mathcal{P}(\delta_*) = \exp \left\{ -\frac{1}{g^2} (\alpha_0 + \alpha_1 g^2 + \alpha_2 g^4 + \dots) \right\}. \quad (2.9)$$

The leading term in this expansion  $\alpha_0$  corresponds to the exponential part given by the leading saddle-point configuration. The first correction  $\alpha_1 g^2$  comes from the Gaussian integration over small fluctuations around the saddle-point solution which is equivalent to an one-loop calculation.<sup>5</sup> This part produces the prefactor in front of the leading exponent. The term  $\alpha_2 g^4$  represents the two-loop correction to the prefactor, and so on. In this paper we focus on evaluation of the first two terms.

Of course, the growth factor  $g(z)$  is not small at low redshift — in fact, we normalize it to 1 at  $z = 0$ . Still, it is convenient to keep it as a formal expansion parameter. As we are going to see shortly, the true expansion goes in the smoothed linear density variance  $\sigma_{r_*}^2(z)$  at the scale of the cell. This is proportional to  $g^2(z)$  which thus provides a useful book-keeping tool to track the powers of  $\sigma_{r_*}^2$  arising in the expansion.<sup>6</sup> Note that the higher-loop contributions corresponding to higher powers of  $g^2$  in (2.9) are more important at lower redshifts.

The functional  $\bar{\delta}_W[\delta_L]$  entering in Eq. (2.8) encodes the relation between the initial linear perturbation and the final non-linear density contrast into which it evolves. It therefore depends on the non-linear dynamics of matter inhomogeneities and can be complicated for a general window function  $\tilde{W}$ . However, the situation is dramatically simplified for the top-hat  $\tilde{W}$ . In this case the symmetry of the problem implies that the saddle-point configuration  $\hat{\delta}_L(\mathbf{k})$  saturating the integral (2.8) is spherically symmetric. Then its evolution is described by equations of spherical collapse which, as long as matter obeys the equivalence principle and before shell-crossing, establish one-to-one mapping between the linear and non-linear density contrasts,

$$\bar{\delta}_W = f(\bar{\delta}_{L,R(\bar{\delta}_W)}) \iff \bar{\delta}_{L,R(\bar{\delta}_W)} = F(\bar{\delta}_W). \quad (2.10)$$

<sup>5</sup>For the sake of the argument, we suppress the logarithmic dependence of  $\alpha_1$  on  $g$  which will be restored later, cf. Eq. (2.12).

<sup>6</sup>Cf. Refs. [11, 74] where a similar trick was used to keep track of the powers of the linear power spectrum in perturbation theory.

Here  $\bar{\delta}_{L,R(\bar{\delta}_W)}$  is the linear density perturbation averaged with a top-hat filter at the Lagrangian radius corresponding to the Eulerian radius  $r_*$  and density contrast  $\bar{\delta}_W$ ,

$$R(\bar{\delta}_W) = r_*(1 + \bar{\delta}_W)^{1/3} . \quad (2.11)$$

In  $\Lambda$ CDM cosmology the mapping (2.10) depends, in principle, on the redshift  $z$ . However, this dependence happens to be very weak, and the functions  $f$  and  $F$  are essentially the same as in the Einstein–de Sitter (EdS) approximation [71].<sup>7</sup> We will adopt the latter approximation in what follows since it somewhat simplifies the analysis. The value of the cosmological constant then affects the PDF only through the redshift dependence of the growth factor  $g(z)$ . The analytic expressions for the functions  $f$ ,  $F$  are given in appendix B.

The mapping (2.10) allows one to find the saddle-point solution and perform the integration over spherically symmetric fluctuations around it analytically (see appendix B). This gives a part of the PDF, to which we refer as ‘‘spherical PDF’’:

$$\mathcal{P}_{\text{sp}}(\delta_*; z, r_*) \equiv \frac{1}{\sqrt{2\pi g^2(z)}} \frac{\partial \nu(\delta_*; r_*)}{\partial \delta_*} e^{-\frac{\nu^2(\delta_*; r_*)}{2g^2(z)}} , \quad (2.12)$$

where

$$\nu(\delta_*; r_*) \equiv \frac{F(\delta_*)}{\sigma_{R_*}} , \quad (2.13)$$

and

$$\sigma_{R_*}^2 = \int_{\mathbf{k}} P(k) |W_{\text{th}}(kR_*)|^2 \quad (2.14)$$

is the linear density variance at the Lagrangian radius

$$R_* = r_*(1 + \delta_*)^{1/3} . \quad (2.15)$$

Note that  $\sigma_{R_*}$  depends on  $\delta_*$  through the filtering radius (2.15). Note also that the exponent is inversely proportional to the density variance, which justifies our claim that the latter plays the role of the saddle-point expansion parameter. The spherical PDF is nothing but a map of the Gaussian PDF for the linear density threshold  $\nu_L = \delta_L/\sigma_L$  to non-linear densities using spherical collapse and mass conservation. It naturally appears in the excursion-set approach to the PDF [67–69] but by itself does not reproduce the correct mean  $\langle \delta_* \rangle = 0$ . This problem can be remedied by correcting  $\mathcal{P}_{\text{sp}}(\delta_*)$  with an additional factor  $1/(1 + \delta_*)$  which then, however, spoils the PDF normalization.

As shown in [71], inclusion of the Gaussian integral over aspherical fluctuations in Eq. (2.8) automatically produces the correct mean and normalization. It leads to an ‘‘aspherical prefactor’’  $\mathcal{A}_{\text{asp}}$ , so that the full PDF takes a factorized form

$$\mathcal{P}(\delta_*; z, r_*) = \mathcal{A}_{\text{asp}}(\delta_*; z, r_*) \cdot \mathcal{P}_{\text{sp}}(\delta_*; z, r_*) . \quad (2.16)$$

---

<sup>7</sup>In particular, the relative difference of the function  $F(\delta_*)$  in the  $\Lambda$ CDM and EdS cosmologies is at most  $3 \cdot 10^{-3}$  for extreme density contrasts and redshift zero.

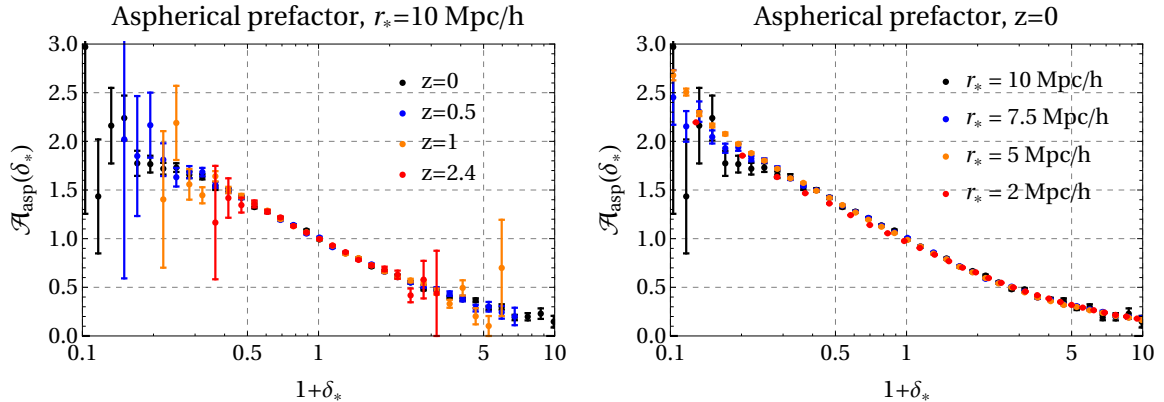


**Figure 2.** Aspherical prefactor measured from the N-body data. *Left:*  $\mathcal{A}_{\text{asp}}(\delta_*)$  for several redshifts at fixed comoving cell radius  $r_* = 10 \text{ Mpc}/h$ . *Right:*  $\mathcal{A}_{\text{asp}}(\delta_*)$  for several cell radii at  $z = 0$ . The errorbars show the statistical uncertainties of the measured PDF.

To get a sense of the properties of  $\mathcal{A}_{\text{asp}}$ , we can compare the formula (2.16) to the PDF measured from data of high-resolution N-body simulation [73]. We take the measured PDF and divide out the spherical part. This gives us an estimate of  $\mathcal{A}_{\text{asp}}(\delta_*)$  shown in Fig. 2. We observe a remarkable universality: The aspherical prefactor has almost no dependence on redshift  $z$  or the cell radius  $r_*$ . The universality persists down to very short scales  $r_* \simeq 2 \text{ Mpc}/h$  which are strongly non-linear at zero redshift. As we explain below, both properties are consistent with the saddle-point expansion suggesting that it can work even at the non-linear scales.

Given rather featureless shape of  $\mathcal{A}_{\text{asp}}(\delta_*)$  one can try to fit it by some simple function with a few free parameters. A possibility of this kind is discussed in appendix C where we consider a fitting function with just two free parameters (for each cell radius) which is shown to capture  $\mathcal{A}_{\text{asp}}$  with reasonable accuracy. Such fitting, however, does not tell us anything about the physical origin of  $\mathcal{A}_{\text{asp}}$  and our ability to describe it in more general cosmologies than minimal  $\Lambda\text{CDM}$ . In what follows we develop an accurate theoretical model for  $\mathcal{A}_{\text{asp}}$  from first principles.

## 2.2 Aspherical prefactor

The aspherical prefactor accounts for the Gaussian integral over small direction-dependent fluctuations of the linear density  $\delta_L$  around the saddle-point solution in Eq. (2.8). These aspherical fluctuations perturb the non-linear density  $\bar{\delta}_W$  in the cell at the second order of perturbation theory. One can think of them as the perturbations of the comoving cell boundary — the trajectories of particles ending up at the radius  $r_*$  by the final time when the PDF is measured, see Fig. 3. Clearly, the perturbations with different multipole numbers  $\ell$  decouple and can be evaluated separately. We now briefly review the algorithm for calculation of the aspherical prefactor developed in [71]. We describe matter as the pressureless fluid and work in

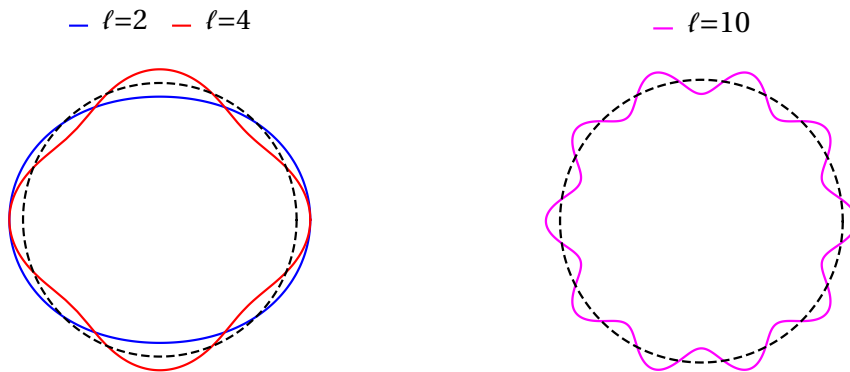


**Figure 3.** Pictorial representation of aspherical fluctuations in different multipole sectors. Dashed line shows the unperturbed cell boundary. *Left:*  $\ell = 2$  and  $\ell = 4$ . *Right:*  $\ell = 10$ .

the EdS approximation.<sup>8</sup> The details are given in appendix D.

As a first step we consider the evolution of linearized aspherical fluctuations in the background of saddle point solution. Expanding all quantities into background and first order perturbations,  $\delta = \hat{\delta} + \delta^{(1)}$ , etc., we write the Euler–Poisson equations to leading order in perturbations. The linearized equations (D.10) contain, besides the density perturbation  $\delta^{(1)}$ , the potentials  $\Psi^{(1)}$  and  $\Theta^{(1)}$  related to the perturbations of velocity  $u_i^{(1)}$  as follows,<sup>9</sup>

$$u_i^{(1)} = -\mathcal{H}\partial_i\Psi^{(1)}, \quad \partial_i u_i^{(1)} = -\mathcal{H}\Theta^{(1)}. \quad (2.17)$$

where  $\mathcal{H} = \partial_t a/a = H_0 e^{-\eta/2}$  is the conformal Hubble parameter,  $t$  is conformal time, and  $a(t)$  is the scale factor normalized to 1 at the present time. In the last expression we introduced a new time variable related to the linear growth rate

$$\eta \equiv \ln g(t) = \ln a(t). \quad (2.18)$$

Working in a particular multipole sector with  $\ell \geq 1$ , we find the first order perturbations  $(\delta_\ell^{(1)}, \Theta_\ell^{(1)}, \Psi_\ell^{(1)})$  for a set of initial wavenumbers  $\{k_I\}$ ,  $I = 1, \dots, N$  representing discretized radial momentum space. We take the momentum lattice to be equidistant with the spacing  $\Delta k = (k_N - k_1)/N$ .

As a next step, we consider the evolution of the second-order monopole perturbation  $\delta_0^{(2)}$  sourced by two aspherical fluctuations with a given  $\ell$  and momenta  $k_I, k_J$ . The problem reduces to two ordinary differential equations (D.24) on the time-dependent cell radius  $r_{IJ}(\eta)$  and the mass perturbation inside it  $\mu_{IJ}^{(2)}(\eta)$  with the sources (D.16) quadratic in first-order aspherical perturbations with  $k_I$  and  $k_J$ . The sources are evaluated at the unperturbed comoving cell boundary  $\hat{r}(\eta)$  corresponding to the trajectories of particles in the saddle-point spherical collapse solution which

<sup>8</sup>We have checked that in  $\Lambda$ CDM the result is the same.

<sup>9</sup>We neglect vorticity which is not generated until shell crossing.

end up at  $r_*$  at the final time  $\eta = 0$ . The second-order perturbation of the mass gives us an element of the response matrix,

$$Q_\ell(k_I, k_J) = \frac{3}{r_*^3} \mu_{IJ}^{(2)}(\eta = 0), \quad (2.19)$$

which describes the second-order response of the non-linear density contrast to the changes in the initial linear field.

We repeat the above procedure for all pairs  $I, J$  and construct the full response matrix for a fixed multipole  $\ell$ . Then, we evaluate the fluctuation determinant in the  $\ell$ th sector [71],

$$\mathcal{D}_\ell = \det \left( \delta_{IJ} + 2\hat{\lambda}(2\pi)^{-3} \Delta k k_I k_J \sqrt{P(k_I)} Q_\ell(k_I, k_J) \sqrt{P(k_J)} \right), \quad (2.20)$$

where  $\hat{\lambda}$  is the saddle-point value of the Lagrange multiplier given in Eq. (B.13). The final answer for the aspherical prefactor is given by the product of contributions from different multipole sectors,

$$\mathcal{A}_{\text{asp}} = \prod_{\ell \geq 1} \mathcal{D}_\ell^{-(\ell+1/2)}. \quad (2.21)$$

Note that the power  $(\ell+1/2)$  comes from the number  $(2\ell+1)$  of independent spherical harmonics in the  $\ell$ th sector.

Let us discuss several general properties of the aspherical prefactor that follow from Eqs. (2.20), (2.21). We observe that these expressions do not explicitly depend on the growth factor  $g$ . Since the latter controls the redshift dependence of the PDF, this implies that  $\mathcal{A}_{\text{asp}}$  formally does not depend on  $z$ . Further, for a power-law power spectrum,  $P(k) \propto k^n$ , the LSS properties are invariant under the simultaneous rescaling of momenta and the power spectrum amplitude,  $P(k) \mapsto \alpha^{-n-3} P(\alpha k)$  [4]. Applied to the PDF, this symmetry maps cells of different radii onto each other,  $r_* \mapsto \alpha^{-1} r_*$ , simultaneously changing the value of  $g^2 \mapsto \alpha^{-n-3} g^2$ . The independence of  $\mathcal{A}_{\text{asp}}$  of  $g$  then implies its independence of the cell radius.

We have already noticed in Fig. 2 that  $\mathcal{A}_{\text{asp}}$  extracted from N-body data is essentially independent of  $z$  and  $r_*$ . This supports the semiclassical expressions (2.20), (2.21) and also suggests that  $\mathcal{A}_{\text{asp}}$  is saturated by modes in a relatively narrow range of momenta where the power spectrum can be approximated as a power-law. We are going to see below that the  $z$  and  $r_*$  independence of  $\mathcal{A}_{\text{asp}}$  is weakly broken by the multiplicative counterterm which renormalizes the UV contribution of modes with high  $\ell$  and  $k$ . Another source of breaking is the two-loop correction, see Sec. 5.

### 2.3 Contribution of UV modes

As discussed above, the computation of the fluctuation determinant for a general  $\ell$  requires solving the system of partial differential equations for the set of functions  $(\delta_\ell^{(1)}, \Theta_\ell^{(1)}, \Psi_\ell^{(1)})$ . But in the limit of large orbital numbers  $\ell \gg 1$  one can use the

Wentzel–Kramers–Brillouin (WKB) approximation to reduce the equations on aspherical perturbations to the ordinary differential equations in time which can be easily solved. The value of this analysis is twofold. First, it allows us to efficiently evaluate the contributions of high multipoles to the aspherical prefactor within the fluid picture. Second, it elucidates the structure of this contribution and provides an insight for its renormalization.

The details of this approach are worked out in appendix E leading to the following key results. First, the WKB equations for linear perturbations have ultralocal form, i.e. they do not contain  $r$ -derivatives and become ordinary differential equations for time evolution along the flow lines of the background solution. Second, the elements of the response matrix (2.19) happen to be small,  $Q_\ell(k, k') \propto (\ell + 1/2)^{-2}$ . This allows us to approximate the fluctuation determinant (2.20) by the exponent of trace,

$$\mathcal{D}_\ell \approx \exp \left( 2\hat{\lambda} \text{Tr} P Q_\ell \right) = \exp \left( 2\hat{\lambda} \int [dk] P(k) Q_\ell(k, k) \right), \quad (2.22)$$

where the integration measure  $[dk]$  is defined in (A.3). We see that only the diagonal elements of the response matrix contribute implying that it is sufficient to solve the second-order equations Eqs. (D.24) only for diagonal sources with  $k_I = k_J = k$ .

Third, the diagonal elements of the response matrix are sums of two parts. One of them quickly oscillates with  $k$ . It gives rise to a quickly oscillating contribution in  $Q_\ell(k, k)$  which averages to zero in the integral (2.22). The second part is slowly varying and has the form,

$$Q_\ell(k, k) \simeq \frac{q(\varkappa)}{k^2(\ell + 1/2)^2}, \quad (2.23)$$

where the symbol  $\simeq$  reminds that we have discarded the oscillating part. The function  $q$  depends only on the ratio,

$$\varkappa \equiv \frac{k}{\ell + 1/2}, \quad (2.24)$$

Using above scaling one can efficiently evaluate the contribution of high- $\ell$  multipoles to the aspherical prefactor, for detail see Ref. [71].

Let us now isolate the contribution of the UV modes into the aspherical prefactor. We sum over all multipoles with  $\ell \gg 1$  and all modes with  $k \gg R_*^{-1}$ , where  $R_*$  is the Lagrangian radius of the cell defined in Eq. (2.15). The corresponding part of the aspherical prefactor can be written as

$$\begin{aligned} \mathcal{A}_{\text{asp}}^{\text{UV}} &\simeq \exp \left\{ \int_{k \gg R_*^{-1}} \frac{dk P(k)}{(2\pi)^3} \sum_\ell \frac{1}{\ell + 1/2} q \left( \frac{k}{\ell + 1/2} \right) \right\} \\ &\approx \exp \left\{ \int_{k \gg R_*^{-1}} \frac{dk P(k)}{(2\pi)^3} \cdot \int_{R_*^{-1}}^\infty \frac{d\varkappa}{\varkappa} q(\varkappa) \right\}, \end{aligned} \quad (2.25)$$

where in the second line we have approximated the sum over  $\ell$  by an integral and used  $d\ell/(\ell + 1/2) = d\mathcal{x}/\mathcal{x}$ . We observe that the expression inside the exponent factorizes into an integral over  $k$  of the power spectrum and a  $\mathcal{x}$ -integral of the function  $q(\mathcal{x})$  encoding the background dependence. The latter integral quickly converges at the upper limit. It has a spurious singularity at the lower end stemming from the breakdown of the WKB approximation at  $\mathcal{x} \rightarrow R_*^{-1}$  but is rendered finite by a proper subtraction of the boundary term (see appendix E.2). We use the dash-integral sign to remind of this subtraction when it is needed.

In deriving (2.25) we used the Euler–Poisson equations for ideal pressureless fluid (see appendix D). This is a good description for modes with moderate  $\ell$  and  $k$ , like those shown on the left of Fig. 3. However, it breaks down for modes with high  $\ell$  and  $k$ . These vary on such short scales that the perturbed trajectories of particles cross violating the single-stream approximation — the modes experience shell-crossing. It is worth stressing that this shell-crossing should not be confused with that happening in the center of the cell on the leading spherical collapse solution for very large overdensities  $\delta_* \gtrsim 7$  (see appendix B). The latter redistributes matter in the central part of the cell but does not affect its total mass.<sup>10</sup> On the other hand, the shell-crossing of short modes occur for all  $\delta_*$  and perturbs the cell boundary (see Fig. 3, right), thereby affecting the mass inside the cell. This effect cannot be discarded in the calculation of the PDF.

Ref. [71] suggested to take this effect into account by renormalizing the  $k$ -integral in Eq. (2.25). The key observation is that the same integral arises in the one-loop calculation of the power spectrum where it is corrected by a *counterterm*  $\gamma$  also sometime referred to as the “sound speed”. Physically,  $\gamma$  is inversely proportional to the square of the cutoff momentum  $k_{\text{sc}}$  corresponding to the modes experiencing shell-crossing,  $\gamma \propto k_{\text{sc}}^{-2}$ . Model 1 proposed in [71] simply applies the renormalization with fixed  $\gamma$  taken from the perturbation theory to the integral in (2.25). This provides a good description of the aspherical prefactor for moderate  $\delta_* \in [-0.5, 1]$  but deviated from the N-body data by  $\sim 30\%$  at the tails, see Fig. 4. The second model of [71] improves the description by estimating the  $\delta_*$ -dependence of the counterterm within the separate universe approximation. In this simplified approach the spherical collapse solution is approximated by a uniform density contrast reaching  $\delta_*$  at the final time. The model happens to provide an accurate description of the data within the statistical errorbars, as shown in Fig. 4 (more detailed comparison of Model 2 with the N-body data can be found in appendix I).

Despite the phenomenological success of Model 2, it is admittedly *ad hoc*. The true saddle-point profile is not uniform (see Fig. 16 from appendix B) and changes significantly at the cell boundary where aspherical perturbations are most important.

---

<sup>10</sup>At least as long as it does not lead to an outflow through the cell boundary which does not happen for  $\delta_* < 9$  and  $r \gtrsim 5 \text{ Mpc}/h$ .

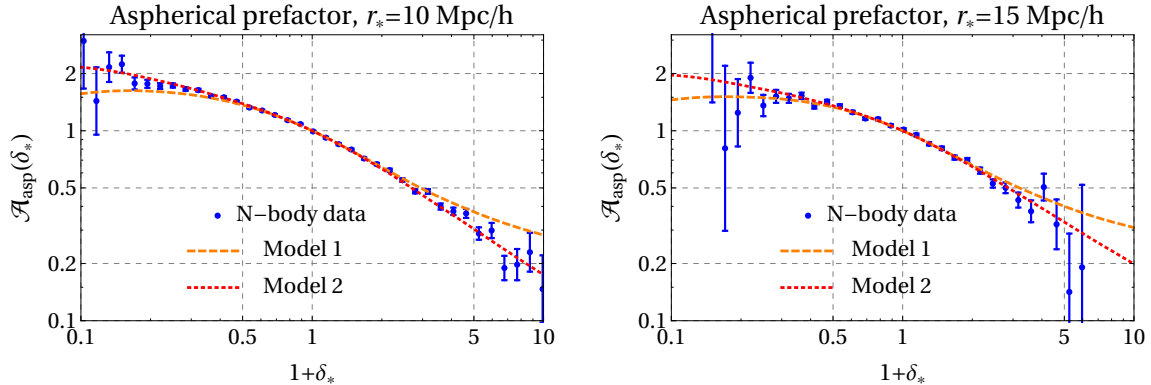


**Figure 4.** Comparison of Models 1 and 2 from Ref. [71] for renormalized aspherical prefactor with the N-body data at  $z = 0$ . The cell radii are  $r_* = 10 \text{ Mpc}/h$  (left) and  $r_* = 15 \text{ Mpc}/h$  (right). The theoretical models use  $\gamma_0 = 1.95 (\text{Mpc}/h)^2$  for the effective speed of sound at  $z = 0$  taken from the fit of the power spectrum (see Sec. 5). The dependence of the sound speed on the growth factor is approximated by a power-law with the index  $m = 8/3$ .

For this reason it was pointed out in [71] that Model 2 should be taken with a grain of salt and, in the absence of a better understanding of the prefactor renormalization, its difference from Model 1 should be considered as the theoretical uncertainty. The goal of this work is to reduce the uncertainty by constructing a well-grounded counterterm model based on renormalization of the stress tensor due to short perturbations in the effective equations of motion.

### 3 Counterterm prefactor and its relation to correlators

Before proceeding to the effective stress tensor, it is instructive to discuss the connection between the renormalization of PDF and the correlation functions. There is a well-known relation between tree-level spherically-averaged cumulants and the physics of spherical collapse providing the leading PDF exponent [53, 75, 76]. In this section we scrutinize the relation at the one-loop level, focusing, in particular, on the counterterms on both sides of the relation.

The EFT approach to LSS suggests to focus on the evolution and statistics of long-wavelength perturbations in the quasi-linear regime, while “integrating out” short non-linear modes. The effect of the latter is then encapsulated into an effective stress tensor that must be added to the r.h.s. of the Euler equation (D.1b) for long modes. Application of this strategy to the PDF means restricting the integral in Eq. (2.8) to modes with  $k < k_{\text{cut}}$ , where  $k_{\text{cut}}$  is some cutoff scale, simultaneously modifying the map  $\bar{\delta}_W[\delta_L]$ . In practice, it is conventional to remove the cutoff by sending  $k_{\text{cut}} \rightarrow \infty$ . Still, the effective stress tensor and hence the modification of the map with respect to the pure fluid picture persists even in this limit and results in a

*counterterm* contribution. By assumption, the latter is an one-loop effect and in the perturbative power counting is proportional to the coupling  $g^2$ . Thus, we write,<sup>11</sup>

$$\bar{\delta}_W[\delta_L] = \bar{\delta}_W^{\text{fluid}}[\delta_L] + g^2 \bar{\delta}_W^{\text{ctr}}[\delta_L], \quad (3.1)$$

where the first term is the pure fluid contribution given by solving the sourceless Euler–Poisson system (D.1), and the second term is the counterterm due to the stress tensor of short modes.

Since the counterterm is  $\mathcal{O}(g^2)$ , it does not affect the saddle-point solution. At one-loop level its contribution is simply given by evaluating  $\bar{\delta}_W^{\text{ctr}}$  on the saddle point and leads to a multiplicative renormalization of the aspherical prefactor,

$$\mathcal{A}_{\text{asp}} = \mathcal{A}^{\text{ctr}} \cdot \mathcal{A}_{\text{asp}}^{\text{fluid}}, \quad (3.2)$$

where  $\mathcal{A}_{\text{asp}}^{\text{fluid}}$  is given by the product of determinants (2.21) computed within the fluid approximation, and

$$\mathcal{A}^{\text{ctr}} = \exp[-\hat{\lambda} \bar{\delta}_W^{\text{ctr}}[\hat{\delta}_L]] \quad (3.3)$$

is the *counterterm prefactor*. To get an idea of its magnitude, we divide the aspherical prefactor extracted from N-body simulations by the computed value of  $\mathcal{A}_{\text{asp}}^{\text{fluid}}$ . The result is shown in Fig. 5. We observe that  $\mathcal{A}^{\text{ctr}}$  varies from 1 at  $\delta_* = 0$  to  $\sim 0.8$  ( $\sim 0.5$ ) at extreme under- (over-) densities. In other words, it represents a moderate, but significant correction to the ideal fluid approximation. We want to develop an algorithm for computing  $\mathcal{A}^{\text{ctr}}$  as function of the density contrast  $\delta_*$ , the cell radius  $r_*$  and redshift  $z$ . This task for arbitrary  $\delta_*$  will be addressed in the next section. Presently, we focus on the vicinity of the point  $\delta_* = 0$  and establish the relation between the Taylor expansion of  $\ln[\mathcal{A}^{\text{ctr}}(\delta_*)]$  and the counterterms in the correlation functions.

We notice that Eq. (2.8) can be viewed as the generating function for connected correlators with the source  $-\lambda W/g^2$ ,

$$w(\lambda) = \ln \left\langle \exp \left( -\frac{\lambda}{g^2} \int_{\mathbf{k}} W(kr_*) \delta(\mathbf{k}) \right) \right\rangle = \sum_{n=2}^{\infty} \frac{1}{n!} \left( -\frac{\lambda}{g^2} \right)^n c_{W,n} \quad (3.4a)$$

where

$$c_{W,n} = \int_{\mathbf{k}_1} \dots \int_{\mathbf{k}_n} W(k_1 r_*) \dots W(k_n r_*) \langle \delta(\mathbf{k}_1) \delta(\mathbf{k}_2) \dots \delta(\mathbf{k}_n) \rangle_{\text{connected}} \quad (3.4b)$$

is the connected  $n$ -point correlator filtered with the window function in each argument. Within the perturbation theory every such correlator can be split into a tree-level and loop parts that scale differently with  $g$ ,

$$c_{W,n} = g^{2(n-1)} c_{W,n}^{\text{tree}} + g^{2n} c_{W,n}^{\text{1-loop}} + \mathcal{O}(g^{2(n+1)}). \quad (3.5)$$

---

<sup>11</sup>We are going to see that  $\bar{\delta}_W^{\text{ctr}}$  can have an additional weak dependence on  $g$ .

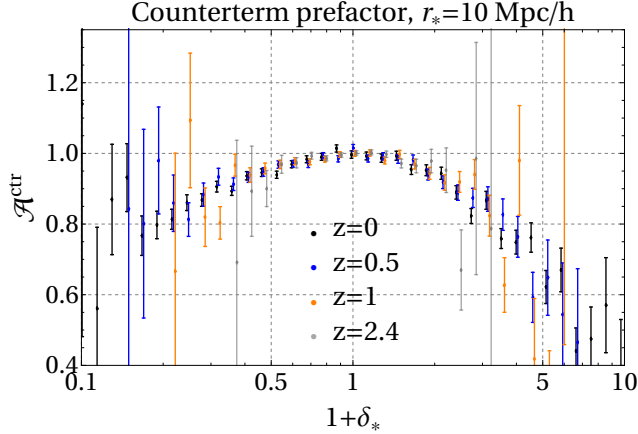


**Figure 5.** Counterterm prefactor extracted from N-body simulations for cell radius  $r_* = 10$  Mpc/h and several values of the redshift. Error bars represent the statistical uncertainty of the simulations.

Grouping terms of the same order in the generating function, we obtain the decomposition,

$$w(\lambda) = \frac{w^{\text{tree}}(\lambda)}{g^2} + w^{1\text{-loop}}(\lambda) + \mathcal{O}(g^2). \quad (3.6)$$

Substituting this onto Eq. (2.7) and evaluating the integral by the saddle point yields the PDF in the form,

$$\mathcal{P}(\delta_*) = \frac{1}{\sqrt{2\pi g^2}} \left( \frac{d^2 w^{\text{tree}}}{d\lambda^2} \Big|_{\hat{\lambda}} \right)^{-1/2} e^{w^{1\text{-loop}}(\hat{\lambda})} \cdot e^{\frac{1}{g^2}(\hat{\lambda}\delta_* + w^{\text{tree}}(\hat{\lambda}))}, \quad (3.7)$$

where  $\hat{\lambda}$  and  $\delta_*$  are related by the saddle-point condition,

$$\delta_* + \frac{dw^{\text{tree}}}{d\lambda} \Big|_{\hat{\lambda}} = 0. \quad (3.8)$$

Of course, the PDF (3.7) must be the same as (2.16) which gives us the expression

$$\mathcal{A}_{\text{asp}} = \sqrt{1 + \nu \frac{d^2 \nu}{d\delta_*^2} \left( \frac{d\delta_*}{d\nu} \right)^2} \exp \left[ w^{1\text{-loop}}(\hat{\lambda}) \right], \quad (3.9)$$

where we have used the relations (3.8) and (B.13) to express the first factor (recall also the definition of  $\nu$  (2.13)). This formula establishes a connection between the aspherical prefactor and the one-loop contribution into the cumulant generating function. Note that while its derivation assumes the validity of the saddle-point approximation, it does not rely on any model for dynamics.

We now observe that the first factor in Eq. (3.9) is determined exclusively by the spherical collapse saddle-point solution and therefore is not UV sensitive. All UV counterterms are contained in the second factor, so we have

$$\ln[\mathcal{A}^{\text{ctr}}(\delta_*)] = w^{\text{ctr}}(\hat{\lambda}), \quad (3.10)$$

where  $w^{\text{ctr}}(\lambda)$  is composed of one-loop counterterms for all correlators using Eqs. (3.4). Let us work out this relation up to the cubic terms. From the equations of appendix B one can obtain,<sup>12</sup>

$$\hat{\lambda}(\delta_*) = -\frac{1}{\sigma_{r_*}^2} \left( \delta_* + 3 \left( \frac{4}{21} - \frac{\xi_{r_*}}{\sigma_{r_*}^2} \right) \delta_*^2 + \mathcal{O}(\delta_*^3) \right), \quad (3.11)$$

where the tree-level variance  $\sigma_{r_*}^2$  and smeared correlation function  $\xi_{r_*}$  are defined by Eqs. (2.14), (B.12b) with  $R_*$  replaced by  $r_*$ . This give us,

$$\ln[\mathcal{A}^{\text{ctr}}(\delta_*)] = \frac{\delta_*^2}{2\sigma_{r_*}^4} c_{W,2}^{\text{ctr}} + \frac{\delta_*^3}{6\sigma_{r_*}^6} \left( c_{W,3}^{\text{ctr}} + 18 \left( \frac{4}{21} - \frac{\xi_{r_*}}{\sigma_{r_*}^2} \right) \sigma_{r_*}^2 c_{W,2}^{\text{ctr}} \right) + \mathcal{O}(\delta_*^4), \quad (3.12)$$

where

$$c_{W,n}^{\text{ctr}} = g^{-2n} \int_{\mathbf{k}_1} \dots \int_{\mathbf{k}_n} W(k_1 r_*) \dots W(k_n r_*) \langle \delta(\mathbf{k}_1) \dots \delta(\mathbf{k}_n) \rangle^{\text{ctr}}. \quad (3.13)$$

Let us discuss this result. First, we note the absence of a linear term. This is consistent with the fact that the first derivative of the aspherical prefactor at  $\delta_* = 0$  is entirely determined by the spherical collapse dynamics and is insensitive to UV [71]. Second, the coefficients of the quadratic and cubic terms are directly related to the counterterms in the power spectrum and bispectrum that have been widely studied in the literature [3–5, 15, 77–81].

The power-spectrum counterterm has the form,

$$\langle \delta(\mathbf{k}) \delta(\mathbf{k}') \rangle^{\text{ctr}} = -2\gamma g^2 k^2 P(k) (2\pi)^3 \delta_{\text{D}}(\mathbf{k} + \mathbf{k}'), \quad (3.14)$$

where  $\gamma$  is a redshift-dependent parameter of dimension  $(\text{length})^2$ , referred to as the “effective sound speed”. By comparing the EFT predictions with the results of N-body simulations it has been shown to approximately follow a power-law dependence on the growth factor,

$$\gamma(z) \simeq \gamma_0 [g(z)]^m, \quad (3.15a)$$

$$\gamma_0 \sim 1.5 (\text{Mpc}/h)^2, \quad m \sim 8/3. \quad (3.15b)$$

Both  $\gamma_0$  and  $m$  depend on cosmology and the details of the analysis (inclusion or not of two-loop corrections, the precise  $k$ -range used for measurements, etc.). The scaling (3.15a) is compatible with the approximation of a power-law power spectrum;

---

<sup>12</sup>Alternatively, one can use Eq. (3.8) and obtain

$$\hat{\lambda} = -\frac{1}{c_{W,2}^{\text{tree}}} \left( \delta_* - \frac{c_{W,3}^{\text{tree}}}{2(c_{W,2}^{\text{tree}})^2} \delta_*^2 + \mathcal{O}(\delta_*^3) \right),$$

which implies the identities,  $c_{W,2}^{\text{tree}} = \sigma_{r_*}^2$ ,  $c_{W,3}^{\text{tree}} = -6\sigma_{r_*}^4 \left( \frac{4}{21} - \frac{\xi_{r_*}}{\sigma_{r_*}^2} \right)$ .

we will elaborate more on this in the next section. Substituting (3.14) into Eq. (3.13) we obtain,

$$c_{W,2}^{\text{ctr}}(z) = -\frac{2\gamma(z)}{g^2(z)}\Sigma_{r_*}^2, \quad (3.16)$$

where

$$\Sigma_{r_*}^2 = \int_{\mathbf{k}} k^2 P(k) |W_{\text{th}}(kr_*)|^2. \quad (3.17)$$

The relation between  $\gamma$  and the Taylor expansion of  $\mathcal{A}^{\text{ctr}}$  will be used below as a prior on the counterterm prefactor model.

The bispectrum counterterm is more complicated. It involves three more parameters whose measurement from N-body data is challenging. Such measurement has been performed in [15], but for different cosmological parameters than in the N-body simulations used in this paper. Since the dependence of the bispectrum counterterm on cosmology is yet to be explored, we presently do not include it in the calibration of  $\mathcal{A}^{\text{ctr}}$ , leaving this task for future.

Note that, in contrast to the fluid part of the prefactor, the counterterm depends on redshift. This dependence is, however, rather mild. Using (3.15), (3.16) we obtain,

$$\ln[\mathcal{A}^{\text{ctr}}] \propto [g(z)]^{m-2}. \quad (3.18)$$

Since  $(m-2) > 0$  this implies that the counterterm contribution to the PDF decreases with increasing redshift, which is expected because the LSS is more linear at early epochs.

## 4 Counterterm model

In this section we develop a procedure for calculation of the counterterm prefactor. We first review the EFT approach to LSS following Refs. [2, 3] and discuss the complications that arise in applying it to the PDF. We then derive an estimate for the shell crossing scale in the background of saddle-point solution. Finally, we propose a model for the counterterm stress tensor renormalizing the contribution of short modes and discuss the qualitative features of the resulting  $\mathcal{A}^{\text{ctr}}$ .

### 4.1 Stress tensor in EFT of LSS

At the fundamental level, matter composed of non-relativistic collisionless particles of mass  $M$  is described by the phase-space density  $f(\mathbf{x}, \mathbf{p}, t)$  where  $\mathbf{x}$  is the comoving spatial coordinate of a particle,  $\mathbf{p} = aM \frac{d\mathbf{x}}{dt}$  is its canonical momentum, and  $t$  is the conformal time. The first two moments of the distribution function over momentum give the local matter density and average flow velocity,

$$\rho(\mathbf{x}, t) = \frac{M}{a^3} \int f(\mathbf{x}, \mathbf{p}, t) d^3p, \quad \mathbf{u}(\mathbf{x}, t) = \frac{\int \mathbf{p} f(\mathbf{x}, \mathbf{p}, t) d^3p}{\int f(\mathbf{x}, \mathbf{p}, t) d^3p}. \quad (4.1)$$

Phase-space density conservation leads to the Vlasov equation,

$$\frac{\partial f}{\partial t} + \frac{\mathbf{p}}{aM} \cdot \nabla f - aM \nabla \Phi \cdot \frac{\partial f}{\partial \mathbf{p}} = 0, \quad (4.2)$$

where  $\Phi$  is the Newtonian potential. Taking moments of Eq. (4.2) over  $\mathbf{p}$  one obtains the Boltzmann hierarchy of equations relating various moments of the distribution to each other. The fluid equations (D.1) correspond to truncating this hierarchy down to first two moments — matter density and flow velocity. Such truncation is not justified for short-wavelength perturbations which undergo shell-crossing breaking the single-stream approximation and generating velocity dispersion [82].

The EFT of LSS overcomes this problem by restricting to long modes. Technically, this is implemented by smoothing the distribution function and Newtonian potential on length scales  $\Delta x \sim k_{\text{cut}}^{-1}$ ,

$$f^l(\mathbf{x}, \mathbf{p}, t) = \int d^3x' k_{\text{cut}}^3 \mathcal{S}(k_{\text{cut}}(\mathbf{x} - \mathbf{x}')) f(\mathbf{x}', \mathbf{p}, t), \quad (4.3a)$$

$$\Phi^l(\mathbf{x}, t) = \int d^3x' k_{\text{cut}}^3 \mathcal{S}(k_{\text{cut}}(\mathbf{x} - \mathbf{x}')) \Phi(\mathbf{x}', t), \quad (4.3b)$$

where the smoothing function  $\mathcal{S}(\mathbf{y})$  has unit width and is normalized in such a way that its integral is equal to 1. Its precise form is unimportant; for example, it can be chosen as a Gaussian. The wavenumber cutoff is assumed to lie below the shell-crossing scale  $k_{\text{cut}} \lesssim k_{\text{sc}}$ .

Let us stress that the smoothing function  $\mathcal{S}$  should not be confused with the window function  $\tilde{W}$  used to construct the PDF. The latter is associated with the physical length scale  $r_*$  which can be varied in the measurements and serves as a parameter of the PDF. In our study we assume it to lie in the mildly non-linear range, so that the corresponding momentum scale is well below the shell-crossing,  $r_*^{-1} \ll k_{\text{sc}}$ . Besides, while in this work we focus on the top-hat window in coordinate space, other choices for  $\tilde{W}$  are in general possible and the PDF is expected to depend on them [58, 71]. On the other hand, the smoothing function  $\mathcal{S}$  is just a theoretical tool to isolate the contribution of short non-linear modes with wavelengths hierarchically smaller than the cell size,  $k_{\text{cut}}^{-1} \ll r_*$ . It appears only in the intermediate steps of the derivation and does not enter in the final answer.

Applying smoothing to the Vlasov equation (4.2) and then taking its moments, we find that the continuity equation (D.1a) is not modified with the long-wavelength density  $\delta^l$  and velocity  $\mathbf{u}^l$  defined using the smoothed distribution (4.3a). The Poisson equation (D.1c) is also left intact by the smoothing procedure thanks to its linearity. On the other hand, the Euler equation (D.1b) receives on the r.h.s. a source of the form,

$$-\frac{1}{1 + \delta^l} \partial_j \tau_{ij}, \quad (4.4)$$

with an effective stress tensor

$$\tau_{ij} = (1 + \delta^l)\sigma_{ij}^l + \frac{2}{3\mathcal{H}^2} \left( [\partial_i \Phi^s \partial_j \Phi^s]^l - \frac{1}{2} \delta_{ij} [\partial_k \Phi^s \partial_k \Phi^s]^l \right). \quad (4.5)$$

It consists of two physically distinct parts to which we will refer as *kinetic* and *potential*. The first is related to the velocity dispersion smoothed on long scales,

$$\sigma_{ij}^l = \frac{\int (v_i - u_i^l)(v_j - u_j^l) f^l d^3p}{\int f^l d^3p}, \quad v_i \equiv \frac{p_i}{aM}. \quad (4.6)$$

Note that the adiabatic initial conditions for LSS correspond to vanishing  $\sigma_{ij}$ . Its non-zero value is generated in the course of evolution due to shell crossing which occurs in the short non-linear modes. The potential contribution is associated to the fluctuations of the gravitational potential at short scales defined as the difference between the full potential and its smoothed part,

$$\Phi^s \equiv \Phi - \Phi^l. \quad (4.7)$$

Note that while smoothing of any linear function of  $\Phi^s$  gives zero by definition, this is not true for quadratic expressions present in (4.5). The potential part is crucial for the decoupling of the virialized structures from the large-scale evolution: it ensures that the effective stress-energy tensor vanishes for fully virialized systems [2]. The stress tensor  $\tau_{ij}$  encapsulates the effect of short modes beyond the cutoff on the long-distance dynamics.

In principle,  $\tau_{ij}$  depends both on the states of short and long modes. We get rid of the former dependence by averaging over random initial conditions for short modes. Using angular brackets with subscript  $s$  to denote the result, we conclude that  $\langle \tau_{ij} \rangle_s$  is a functional of the long-wavelength perturbation only.<sup>13</sup> In general, this functional is complicated and depends on the full non-linear configuration of the long mode and its history. The situation is simplified in the case when the long mode can be treated perturbatively. Then  $\langle \tau_{ij} \rangle_s$  can be systematically expanded in powers of the density contrast  $\delta^l$ , the tidal tensor  $\partial_i \partial_j \Phi^l - (1/3)\delta_{ij} \Delta \Phi^l$  and their spatial derivatives. The expansion is still non-local in time, but this issue can be treated consistently at each order of the perturbation theory in  $\delta^l$ .

Presence of  $\langle \tau_{ij} \rangle_s$  leads to additional terms in the cosmological correlation functions. For concreteness, let us focus on the one-loop power spectrum. At this level, the only relevant term in the stress tensor is

$$\langle \tau_{ij}(\mathbf{x}, \eta) \rangle_s = \tilde{d}(\eta) \delta_{ij} \delta^l(\mathbf{x}, \eta), \quad (4.8)$$

---

<sup>13</sup>Apart from this deterministic component,  $\tau_{ij}$  contains also a stochastic contribution. However, its effect on LSS statistics is subdominant [3, 4] and we neglect it in this paper.

where  $\tilde{d}(\eta)$  is a time-dependent coefficient of dimension (length)<sup>2</sup>. On dimensional grounds, it must be proportional to the inverse cutoff squared,  $\tilde{d} \sim k_{\text{cut}}^{-2}$ . Substituting (4.8) into perturbed Euler equation gives correction to the density contrast

$$\delta^l(\mathbf{k}, \eta) \ni -\tilde{\gamma}(\eta)k^2\delta_L(\mathbf{k}, \eta), \quad (4.9)$$

where  $\tilde{\gamma}(\eta)$  is a time integral of  $\tilde{d}$ , convolved with the fluid equations' Green function [8]. This correction is small as long as  $k$  is well below the cutoff,  $k^2\tilde{\gamma} \sim k^2/k_{\text{cut}}^2 \ll 1$ . It leads to the counterterm in the power spectrum,

$$\langle \delta^l(\mathbf{k}, \eta)\delta^l(\mathbf{k}', \eta) \rangle^{\text{ctr}} = -2k^2\tilde{\gamma}(\eta)g^2(\eta)P(k)(2\pi)^3\delta_{\text{D}}(\mathbf{k} + \mathbf{k}'), \quad (4.10)$$

which adds up to the standard one-loop contribution from the modes below the cutoff computed using the ideal fluid approximation. A detailed analysis shows that the counterterm enters into the final result in the combination with the most UV sensitive part of the one-loop contribution controlled by the integral of the power spectrum from  $k$  to  $k_{\text{cut}}$ . This combination reads,

$$\tilde{\gamma}(\eta) + g^2(\eta)\frac{122\pi}{315}\int_k^{k_{\text{cut}}}\frac{dqP(q)}{(2\pi)^3}. \quad (4.11)$$

Up to now, we have been working with finite cutoff  $k_{\text{cut}}$ . However, it is convenient to extend the momentum integrals to infinity, absorbing the change into the redefinition of the counterterm coefficient,

$$\tilde{\gamma} \mapsto \gamma = \tilde{\gamma} - g^2\frac{122\pi}{315}\int_{k_{\text{cut}}}^{\infty}\frac{dqP(q)}{(2\pi)^3}. \quad (4.12)$$

This corresponds to formally extending the fluid approximation to arbitrarily short modes which, however, does not lead to inconsistencies since spurious contribution coming from the incorrect treatment of the short modes gets renormalized by the proper adjustment of the counterterm. Recalling the relation between  $\gamma$  and the effective stress tensor, we see that we can perform the renormalization already at the level of the equations of motion where we can treat all modes on equal footing with an appropriate choice of the counterterm stress  $\tau_{ij}^{\text{ctr}}$ . In what follows we will not distinguish long and short modes and will omit the corresponding superscripts.

Let us discuss the time dependence of  $\gamma$ . On dimensional grounds one expects  $\gamma$  to be inversely proportional to the square of the physical cutoff of the ideal fluid theory which is set by the shell-crossing scale,

$$\gamma(\eta) \propto (k_{\text{sc}}(\eta))^{-2}. \quad (4.13)$$

In the perturbation theory around homogeneous background the shell-crossing scale coincides with the non-linear scale  $k_{\text{NL}}$  at which the density variance reaches order-one,

$$\langle \delta^2 \rangle_{k_{\text{NL}}} = g^2(\eta) \cdot 4\pi \int_0^{k_{\text{NL}}(\eta)} [dk]P(k) \sim 1. \quad (4.14)$$

We can move one step further by approximating the power spectrum in the relevant range of wavenumbers by a power-law,

$$P(k) \propto k^n . \quad (4.15)$$

Then Eq. (4.14) implies

$$k_{\text{sc}} \simeq k_{\text{NL}} \propto (g(\eta))^{-\frac{2}{n+3}} , \quad \gamma(\eta) \propto (g(\eta))^{\frac{4}{n+3}} . \quad (4.16)$$

The latter scaling has been already mentioned in Eq. (3.15) where we can now identify  $m = 4/(n + 3)$ .

Which part of the above reasoning applies to the non-perturbative PDF? It is easy to see that the derivation of the effective stress tensor (4.5) does not rely on any properties of the perturbation theory and thus holds for the non-perturbative case as well. The separation into long and short modes still holds as long as the shell crossing scale  $k_{\text{sc}}$  is much higher than the inverse cell radius  $r_*^{-1}$ . The latter sets the scale of long modes in this problem. We can further send the cutoff to infinity at the expense of retaining the counterterm stress  $\tau_{ij}^{\text{ctr}}$ . What is missing, however, is the possibility to restrict only to a finite number of terms in the Taylor expansion of  $\tau_{ij}^{\text{ctr}}$  in the long-mode overdensity. Indeed, the saddle-point solution  $\hat{\delta}$  is in general not small and all terms in the Taylor expansion contribute equally. Allowing for arbitrary coefficients in front of them in the strict application of EFT rules would lead to a complete loss of predictive power. Thus, we are compelled to *model* the  $\hat{\delta}$  dependence of  $\tau_{ij}^{\text{ctr}}$  invoking reasonable physical assumptions. This necessarily introduces some degree of model dependence that must be treated as a theoretical uncertainty. We now proceed to the description of our model.

## 4.2 Shell-crossing in the background of spherical collapse

The key element of the model is the shell-crossing scale  $k_{\text{sc}}$  in the vicinity of the Lagrangian radius  $R = R_*$  which corresponds to the unperturbed boundary of the cell in the Lagrangian space. The spherical collapse dynamics maps the latter to the trajectory  $\hat{r}(\eta)$  in the Eulerian space, such that  $\hat{r}(-\infty) = R_*$ ,  $\hat{r}(0) = r_*$ . To estimate the dependence of  $k_{\text{sc}}$  on  $\eta$  and  $r$  in the vicinity of this trajectory, we use the linear perturbation theory on top of the saddle-point spherical collapse solution. Of course, such estimate is not precise since  $k_{\text{sc}}$  characterizes intrinsically non-linear dynamics of the short modes. Still, we expect it to reproduce the right scalings. The logic here is the same as in the derivation of Eqs. (4.14), (4.16) — we use the linear theory to identify the critical momenta at which it breaks down.

Consider the trajectory of a matter particle belonging to the saddle-point spherical collapse solution perturbed by a linear fluctuation. It has fixed Lagrangian coordinates  $X_i$  and time-dependent Eulerian coordinates  $x_i$ . The latter obey the

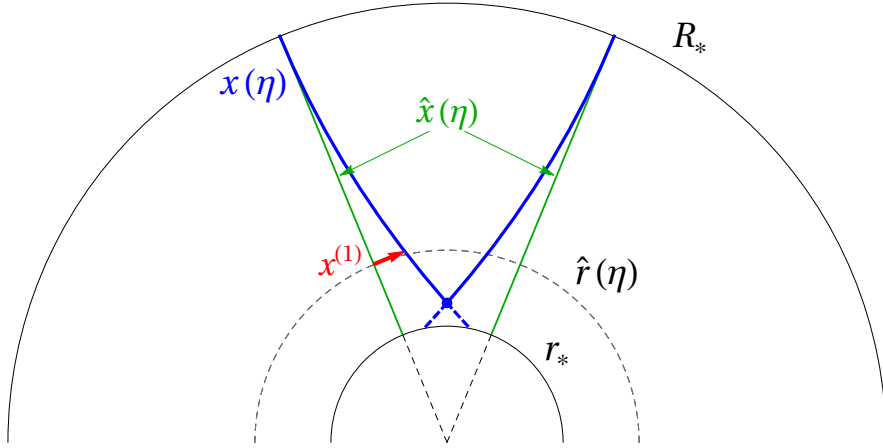


**Figure 6.** Trajectories of two matter particles (blue curves) moving along the flow lines of the background saddle-point solution (straight green lines) perturbed by linear fluctuations  $\mathbf{x}^{(1)}$  (red arrow). The particles evolve from the initial Lagrangian radius  $R_*$  to the final radius of the cell  $r_*$ . The shell-crossing occurs when the variance of the perturbation becomes comparable to the unperturbed distance between the two particles (blue dot).

equations,

$$\frac{dx_i}{d\eta} = -\partial_i \hat{\Psi}(\eta, \mathbf{x}) - \partial_i \Psi^{(1)}(\eta, \mathbf{x}), \quad (4.17)$$

where  $\hat{\Psi}$  is the background part of the velocity potential and  $\Psi^{(1)}$  is the fluctuation. Linearizing this equation, we obtain,

$$\frac{dx_i^{(1)}}{d\eta} = -\partial_i \partial_j \hat{\Psi}(\eta, \hat{\mathbf{x}}) x_j^{(1)} - \partial_i \Psi^{(1)}(\eta, \hat{\mathbf{x}}), \quad (4.18)$$

where both velocity potentials are now evaluated on the unperturbed trajectory  $\hat{x}_i(\eta)$  satisfying

$$\frac{d\hat{x}_i}{d\eta} = -\partial_i \hat{\Psi}(\eta, \hat{\mathbf{x}}). \quad (4.19)$$

In this way the perturbation  $\mathbf{x}^{(1)}$  can be considered as function of time  $\eta$  and unperturbed coordinates  $\hat{\mathbf{x}}$ .

Let us for concreteness consider the case of overdensity  $\delta_* > 0$ , so that  $R_* > r_*$ . The amplitude of the perturbation  $\mathbf{x}^{(1)}$  grows as the particle moves towards smaller radii, see a schematic picture of the particle trajectory in Fig. 6. Two particles starting from different points at  $r = R_*$  may come closer to each other and their trajectories may cross. It is worth stressing that the shell-crossing responsible for the counterterm prefactor happens in the vicinity of the cell boundary, rather than in its center, see Fig. 6. Shell-crossing corresponds to a singularity of the Euler-space

density contrast,

$$\begin{aligned}
1 + \delta(\eta, \mathbf{x}) &= \left( \det \frac{\partial x_i}{\partial X_j} \right)^{-1} = \left[ \det \left( \frac{\partial \hat{x}_i}{\partial X_j} + \frac{\partial x_i^{(1)}}{\partial X_j} \right) \right]^{-1} \\
&= \left( \det \frac{\partial \hat{x}_k}{\partial X_l} \right)^{-1} \left[ \det \left( \delta_i^j + \frac{\partial x_i^{(1)}}{\partial \hat{x}_j} \right) \right]^{-1}. \tag{4.20}
\end{aligned}$$

The first factor here is finite since the spherical collapse background solution is regular. Thus, the singularity must arise from the second factor controlled by the perturbations. For the determinant to vanish, the elements of the matrix

$$\varpi_i^j \equiv -\frac{\partial x_i^{(1)}}{\partial \hat{x}_j} \tag{4.21}$$

must be of order one.

To estimate them, consider the trace  $\varpi \equiv \varpi_i^i$  which characterizes the focusing of near-by particle trajectories. Combining Eqs. (4.18) and (4.19) yields for its evolution along the unperturbed trajectory (see derivation in appendix F):

$$\frac{d\varpi}{d\eta} = \Delta\Psi^{(1)} = \Theta^{(1)}. \tag{4.22}$$

This result is easy to understand intuitively: the increased focusing of particles is given by the convergence of the velocity perturbation. Thus, to find  $\varpi$  at a given moment of time  $\eta$  and position  $\hat{\mathbf{x}}$ , we trace back the trajectory of particle from this point along the unperturbed spherical collapse solution to its original Lagrangian position  $\mathbf{X}$ . Let us denote this trajectory as  $\hat{\mathbf{x}}(\eta', \mathbf{X})$ . In this way  $\varpi$  becomes a function of time and the Lagrangian coordinate:

$$\varpi(\eta, \mathbf{X}) = \int_{-\infty}^{\eta} d\eta' \Theta^{(1)}(\eta', \hat{\mathbf{x}}(\eta', \mathbf{X})). \tag{4.23}$$

We can now calculate the variance of  $\varpi$ . It is the same for all points with the same Eulerian radius  $\hat{r}$  corresponding to Lagrangian radius  $R$ . Expanding  $\Theta^{(1)}$  in spherical harmonics and using the basis  $\Theta_\ell^{(1)}(\eta, r; k_I)$  introduced in Sec. 2.2, we obtain the contribution of modes with  $k < k_{\max}$ ,

$$\begin{aligned}
\langle \varpi^2 \rangle_{k_{\max}} &= \sum_{\ell} \frac{2\ell + 1}{4\pi} \int^{k_{\max}} [dk] P(k) \left| \int_{-\infty}^{\eta} d\eta' \Theta_\ell^{(1)}(\eta', \hat{r}(\eta', R); k) \right|^2 \\
&\approx 4\pi \int^{k_{\max}} [dk] P(k) \cdot \int_{1/R}^{\infty} \frac{d\mathcal{K}}{(2\pi)^2 \mathcal{K}} \left| \int_{-\infty}^{\eta} d\eta' \vartheta_\ell(\eta', R; \mathcal{K}) \right|^2. \tag{4.24}
\end{aligned}$$

In the last equality we used the WKB approximation for short modes (see appendix E.1) and replaced the sum over  $\ell$  with the integral over  $\mathcal{K}$ . Note that the

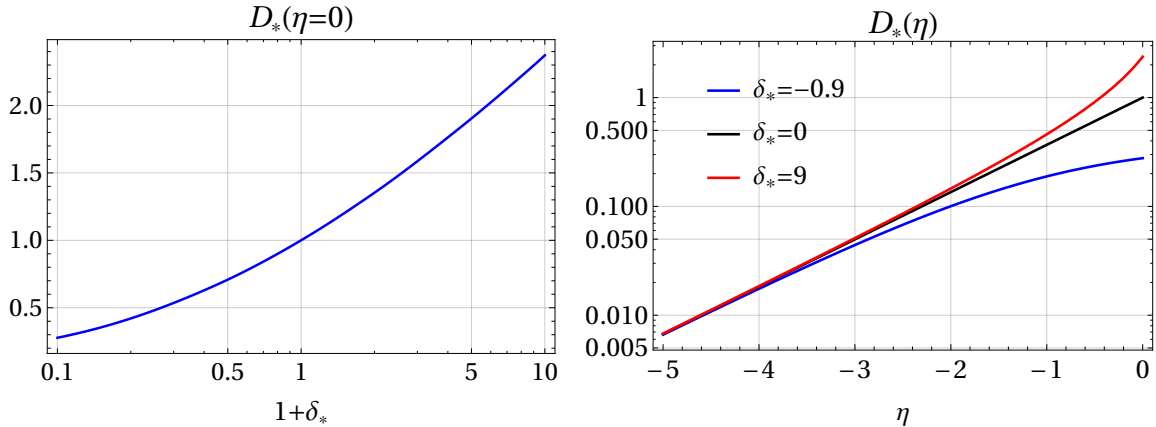


**Figure 7.** Cumulative growth factor of short modes in the background of the saddle-point solution evaluated at the cell boundary. *Left:* Dependence on the density contrast for  $\eta = 0$ . *Right:* Time dependence for three different density contrasts.

expression has factorized due to the universal behavior of the WKB functions. The first factor — the integral of  $k$  — describes the statistical properties of the initial conditions. Whereas the second factor

$$D(\eta; R) = \left( \int_{1/R}^{\infty} \frac{d\boldsymbol{\varkappa}}{(2\pi)^2 \boldsymbol{\varkappa}} \left| \int_{-\infty}^{\eta} d\eta' \vartheta_{\ell}(\eta', R; \boldsymbol{\varkappa}) \right|^2 \right)^{1/2} \quad (4.25)$$

describes the growth of the short-mode velocity divergence in the background of the saddle-point solution. Note that it depends on time and the Lagrangian radius of the matter shell comoving with the background flow. Through the latter it implicitly depends on the eventual density contrast  $\delta_*$  which determines the background solution.

Using the formulas from appendix E.1 one can show that for  $\delta_* = 0$  the growth factor (4.25) becomes independent of  $R$  and reduces to  $e^{\eta} \equiv g(\eta)$  — the usual linear growth rate. However, for  $\delta_* \neq 0$  it sizeably deviates from  $g(\eta)$ . As we will see in the next subsection, we will only need its value and the value of its first radial derivative at the cell boundary  $\hat{r}(\eta)$  (which corresponds to the fixed Lagrangian radius  $R = R_*$ ). In more detail, we introduce

$$D_*(\eta) \equiv D(\eta, R_*) , \quad [\ln D_*(\eta)]' \equiv \left( \frac{\partial \hat{r}(\eta, R)}{\partial R} \right)^{-1} \partial_R \ln D(\eta, R) \Big|_{R=R_*} . \quad (4.26)$$

In the left panel of Fig. 7 we show the dependence of  $D_*$  on  $\delta_*$  for  $\eta = 0$ . The right panel of Fig. 7 shows the time dependence of  $D_*$  for three representative density contrasts.

We are now ready to estimate the shell crossing scale by equating

$$\langle \varpi^2 \rangle_{k_{\text{sc}}} \sim 1 . \quad (4.27)$$

Using the power-law power spectrum approximation, we get (cf. (4.16)),

$$k_{\text{sc}}(\eta, R) \propto (D(\eta, R))^{-m/2}. \quad (4.28)$$

We will use this scaling in our counterterm model below.

Of course, the definition of  $k_{\text{sc}}$  in non-linear background is not unique. Instead of focusing on the trace of the matrix (4.21), one can consider the variance of its individual elements, or some combination thereof. A few options are discussed in appendix F and shown to give qualitatively similar results. We use them to estimate the theoretical uncertainty of the model.

### 4.3 Counterterm stress for spherical collapse

The symmetry of the background implies that the only non-vanishing components of the counterterm stress tensor are  $\tau_{rr}^{\text{ctr}} \equiv \tau_{\parallel}^{\text{ctr}}$  and  $\tau_{\mu\nu}^{\text{ctr}} = r^2 g_{\mu\nu} \tau_{\perp}^{\text{ctr}}$  where  $\mu, \nu = \theta, \phi$  are the angular directions, and  $g_{\mu\nu}$  is the metric on the unit two-sphere. Both  $\tau_{\parallel}^{\text{ctr}}$  and  $\tau_{\perp}^{\text{ctr}}$  are independent of the angles. The force appearing in Eq. (4.4) and entering the Euler equation is purely radial. It perturbs the trajectory of the cell boundary and thereby modifies the mass inside it. Repeating the derivation in appendices D.3 and D.4 we obtain that the perturbations of the cell radius and mass satisfy the system of equations,

$$\dot{\mu}^{\text{ctr}} + A(\eta) \dot{r}^{\text{ctr}} + \frac{dA}{d\eta} r^{\text{ctr}} = 0, \quad (4.29a)$$

$$\ddot{r}^{\text{ctr}} + \frac{1}{2} \dot{r}^{\text{ctr}} + B(\eta) r^{\text{ctr}} + \frac{3}{2\hat{r}^2} \mu^{\text{ctr}} = -\Upsilon_{\Theta}^{\text{ctr}}, \quad (4.29b)$$

where the functions  $A(\eta)$ ,  $B(\eta)$  are defined in (D.22), (D.25), and the *counterterm source* reads

$$\Upsilon_{\Theta}^{\text{ctr}}(\eta) = \frac{1}{\mathcal{H}^2(1+\hat{\delta})} \partial_j \tau_{ij}^{\text{ctr}} \Big|_{i \rightarrow r} = \frac{1}{\mathcal{H}^2(1+\hat{\delta})} \left( \partial_r \tau_{\parallel}^{\text{ctr}} + \frac{2}{r} \tau_{\parallel}^{\text{ctr}} - \frac{2}{r} \tau_{\perp}^{\text{ctr}} \right) \Big|_{\eta, \hat{r}(\eta)}. \quad (4.30)$$

Here  $\hat{\delta}(\eta, r)$  is the density contrast of the unperturbed spherical collapse solution, and all quantities are evaluated at the unperturbed moving cell boundary  $\hat{r}(\eta)$ . We observe that these equations and the source term have the same structure as the equations (D.24) and the source (D.34) governing the second-order perturbations of the density contrast in the cell. As in that case, Eqs. (4.29) are to be solved with the boundary conditions:

$$r^{\text{ctr}} \Big|_{\eta=0} = 0; \quad e^{-\eta} \mu^{\text{ctr}}, e^{-\eta} \left( \dot{r}^{\text{ctr}} + \frac{d \ln A}{d\eta} r^{\text{ctr}} \right) \rightarrow 0 \text{ at } \eta \rightarrow -\infty, \quad (4.31)$$

which uniquely fix the solution. The first condition enforces that the radius of the cell at the final time remains unperturbed and still equals  $r_*$ , whereas the second

condition implies that the perturbation is truly second-order and does not contain any admixture of the first-order perturbations which behave as  $\propto e^\eta$  at early epoch. Once Eqs. (4.29) are solved, the counterterm prefactor (3.3) at  $\eta = 0$  is determined through

$$\bar{\delta}_W^{\text{ctr}} = \frac{3}{r_*^3} \mu^{\text{ctr}}(\eta = 0) . \quad (4.32)$$

The counterterm source must renormalize the UV-sensitive contributions coming from the perturbative calculation. In Sec. 2.3 we have discussed the contributions of the short modes with  $k \gg R_*^{-1}$  to the prefactor. However, the same result will be obtained if we first integrate these modes out and construct their effective stress tensor. Indeed, consider a slab of modes with momenta  $k$ , such that

$$1/R_* \ll k_1 < k < k_2 \ll k_{\text{sc}*} , \quad (4.33)$$

so that these modes, while being short, are still within the validity of the fluid description. The velocity dispersion of such modes with respect to the background flow is

$$\sigma_{ij}^l = \langle u_i^{(1)} u_j^{(1)} \rangle_s = \mathcal{H}^2 \langle \partial_i \Psi^{(1)} \partial_j \Psi^{(1)} \rangle_s , \quad (4.34)$$

where averaging is over the ensemble of random mode realizations. We substitute this into the kinetic part of the stress tensor (4.5) and expand  $\Psi^{(1)}$  into spherical harmonics. The radial (parallel) and transverse (perpendicular) parts of the stress tensor have precisely the form of the first terms in (D.35) obtained in the perturbative analysis. Performing the same manipulations with the potential part of the effective stress (4.5), we reproduce the remaining terms in (D.35). The agreement of the short-wavelength contribution obtained through the effective stress tensor with the perturbative calculation constitutes a consistency check of our approach. Integrating over short modes and using the WKB approximation, we obtain the kinetic and potential contributions to the stress tensor as a function of the Lagrangian radius,

$$\tau_\alpha^a = 2\mathcal{H}^2 \int_{k_1}^{k_2} \frac{dk P(k)}{(2\pi)^3} \cdot \int_{R^{-1}}^\infty \frac{d\mathcal{K}}{\mathcal{K}} \chi_\alpha^a(\eta, R; \mathcal{K}) , \quad a = \text{kin, pot}; \quad \alpha = \parallel, \perp , \quad (4.35)$$

The expressions for the WKB fields  $\chi_\alpha^a$  are given in appendix E.1.

The extension of  $k$ -integration in (4.35) up to infinity would be illegitimate because of the breakdown of the fluid approximation, so these effective stress tensors must be renormalized. Given the distinct physical origin of the kinetic and potential stresses, it is natural to renormalize them separately. We now construct the counterterm stresses  $\tau_\alpha^{\text{kin,ctr}}$  and  $\tau_\alpha^{\text{pot,ctr}}$  as follows. We assume that the expressions (4.35) capture faithfully the effect of short modes up to  $k \lesssim k_{\text{sc}}$ . The modes with  $k \gtrsim k_{\text{sc}}$ , however, are not described correctly. The counterterms must fix this discrepancy, so they should scale as

$$\tau_\alpha^{a,\text{ctr}} \sim 2\mathcal{H}^2 \int_{k_{\text{sc}}}^\infty \frac{dk P(k)}{(2\pi)^3} \cdot \int \frac{d\mathcal{K}}{\mathcal{K}} \chi_\alpha^a . \quad (4.36)$$

For a power-law power spectrum (4.15) with  $-3 < n < -1$  we have a chain of scaling relations

$$\int_{k_{\text{sc}}}^{\infty} dk P(k) \propto k_{\text{sc}}^{n+1} \propto \frac{1}{k_{\text{sc}}^2} \cdot k_{\text{sc}}^{n+3} \propto \frac{1}{k_{\text{sc}}^2} \int^{k_{\text{sc}}} [dk] P(k) \propto \frac{1}{k_{\text{sc}}^2 D^2} \propto D^{m-2}, \quad (4.37)$$

where in the last two equalities we used Eqs. (4.24), (4.27) and (4.28). This motivates us to make the following Ansatz,

$$\tau_{\alpha}^{a,\text{ctr}}(\eta, R) = \zeta^a \cdot 2\mathcal{H}^2(D(\eta, R))^{m-2} \int_{R^{-1}}^{\infty} \frac{d\boldsymbol{\varkappa}}{\boldsymbol{\varkappa}} \chi_{\alpha}^a(\eta, R; \boldsymbol{\varkappa}), \quad a = \text{kin, pot}; \quad \alpha = \parallel, \perp, \quad (4.38)$$

where  $\zeta^a$  are constant parameters of dimension (length)<sup>2</sup>, independent of time, space or density contrast. We will refer to them as the kinetic and potential counterterm amplitudes. In the spirit of EFT, they must be treated as nuisance parameters in fitting the PDF data with the model.

For the PDF calculation we need to go from the stress tensor to the  $\Upsilon$ -sources. Substituting (4.38) into (4.30) we obtain,<sup>14</sup>

$$\Upsilon^a(\eta) = 2\zeta^a [D_*(\eta)]^{m-2} \left[ \int_{R_*^{-1}}^{\infty} \frac{d\boldsymbol{\varkappa}}{\boldsymbol{\varkappa}} v^a(\eta; \boldsymbol{\varkappa}) + \frac{(m-2)[\ln D_*(\eta)]'}{1 + \hat{\delta}|_{\eta, \hat{r}(\eta)}} \int_{R_*^{-1}}^{\infty} \frac{d\boldsymbol{\varkappa}}{\boldsymbol{\varkappa}} \chi_{\parallel}^a(\eta, R_*; \boldsymbol{\varkappa}) \right]. \quad (4.39)$$

where we introduced the rescaled WKB sources,<sup>15</sup>

$$v^a = \frac{1}{1 + \hat{\delta}} \left[ \partial_r \chi_{\parallel}^a + \frac{2}{r} \chi_{\parallel}^a - \frac{2}{r} \chi_{\perp}^a \right] \Big|_{\eta, \hat{r}(\eta)}. \quad (4.40)$$

Eq. (4.39) is our final expression for the counterterm sources used in the numerical procedures. It contains three free parameters: the counterterm scaling index  $m$  and the kinetic and potential counterterm amplitudes  $\zeta^{\text{kin}}, \zeta^{\text{pot}}$ . The rest of it is determined by the dynamics of the spherical collapse and small perturbations on top of it.

#### 4.4 Synthesis

Let us summarize the procedure for calculating the counterterm prefactor in the PDF:

1. Fix the values of  $m, \zeta^{\text{kin}}, \zeta^{\text{pot}}$ .
2. Find the saddle-point solution for the density contrast  $\delta_*$ .
3. Solve the WKB equations (E.8), (E.4) along the flow line corresponding to the cell boundary  $\hat{r}(\eta)$ .

<sup>14</sup>From now on we omit the “ctr” index on the counterterm sources, to avoid cluttered notations.

<sup>15</sup>Note that radial derivative in the expression for  $v^a$  is taken with respect to the Eulerian radius at fixed time. Since  $\chi_{\parallel}^a$  depends on the Lagrangian radius, we have  $\partial_r \chi_{\parallel}^a = (\partial \hat{r}(\eta, R)/\partial R)^{-1} \partial_R \chi_{\parallel}^a$ .

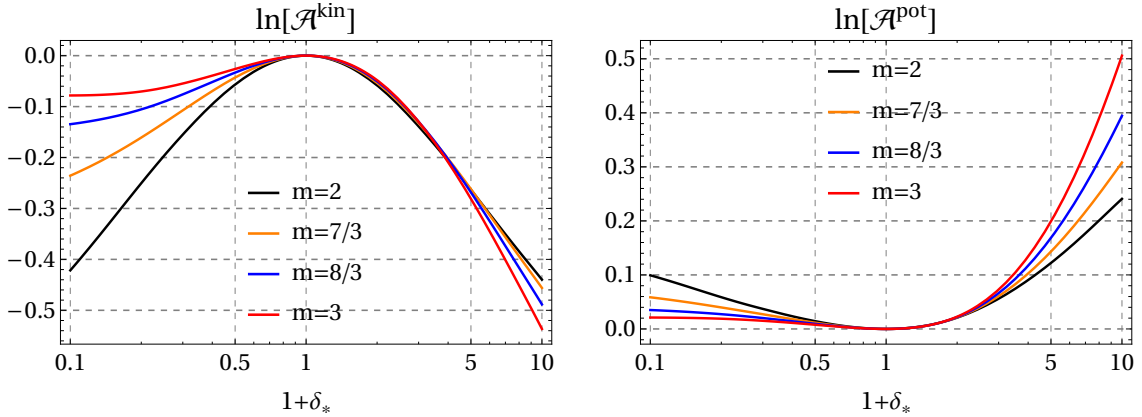


**Figure 8.** Contributions to the counterterm prefactor at zero redshift for  $r_* = 10 \text{ Mpc}/h$ . The parameters  $\zeta^{\text{kin}}, \zeta^{\text{pot}}$  are fixed to  $(1 \text{ Mpc}/h)^2$ . Both contributions are evaluated for the cosmological parameters of the Farpoint simulation [73].

4. Compute the cumulative growth factor  $D_*$ , Eq. (4.25).
5. Evaluate  $v^{\text{kin}}, v^{\text{pot}}$  using Eqs. (E.12) and compute their  $\varkappa$ -integrals.
6. Construct the sources (4.39) and solve Eqs. (4.29) separately for  $\Upsilon^{\text{kin}}$  and  $\Upsilon^{\text{pot}}$ . This gives the counterterm densities  $\bar{\delta}_W^{\text{kin}}$  and  $\bar{\delta}_W^{\text{pot}}$ .
7. Substitute them into Eq. (3.3) to obtain

$$\mathcal{A}^a = \exp[-\hat{\lambda} \bar{\delta}_W^a], \quad a = \text{kin}, \text{pot}. \quad (4.41)$$

The full counterterm prefactor is the product  $\mathcal{A}^{\text{ctr}} = \mathcal{A}^{\text{kin}} \cdot \mathcal{A}^{\text{pot}}$ .

8. Repeat the steps 2 to 7 for different  $\delta_*$ .

We have focused so far on the counterterm prefactor at the present epoch. One might think that for computing the PDF at non-zero redshift,  $z_1 > 0$ , one has to repeat the whole procedure from the start. Fortunately, this is not the case thanks to the invariance of EdS with respect to time-translations in  $\eta$ . Consider the PDF at  $\eta_1 < 0$ . The saddle-point solution corresponding to  $\delta_*$  in this case is obtained simply by translating the solution corresponding to  $\delta_*$  at the present epoch back in time by  $\eta_1$ ,

$$\hat{\delta}_1(\eta, r) = \hat{\delta}_0(\eta - \eta_1, r). \quad (4.42)$$

The linear perturbations translated backward by the same amount are also solutions of the relevant equations. However, they do not obey the asymptotic initial conditions (D.12), differing in normalization. To make them properly normalized, we have to multiply them by a constant factor  $e^{\eta_1}$ . This implies that the new growth factor and

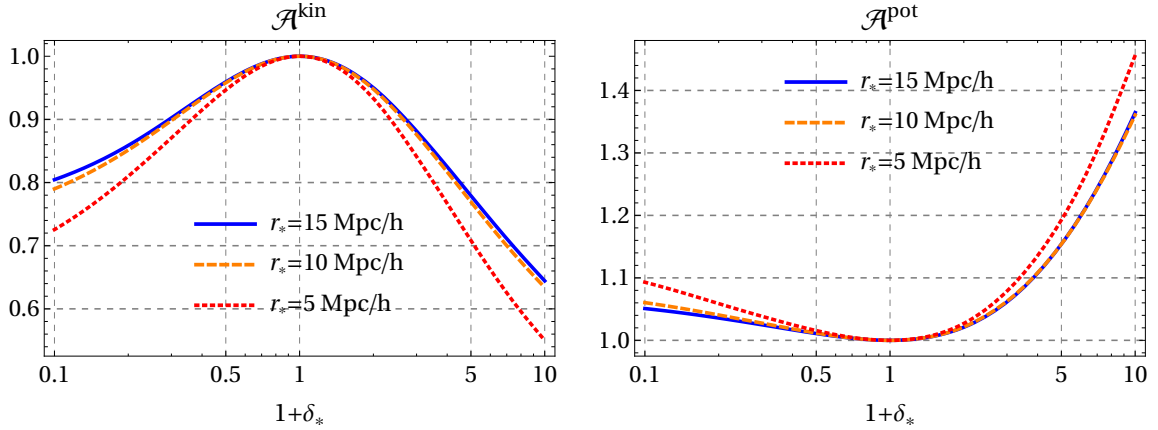


**Figure 9.** Contributions to the counterterm prefactor at redshift zero for several cell radii. Cosmological parameters are the same as in the Farpoint simulation [73]. The model parameters are  $\zeta^{\text{kin}} = \zeta^{\text{pot}} = (1 \text{ Mpc}/h)^2$ ,  $m = 2.33$ .

fields  $\chi_\alpha^a$  are related to the old ones by

$$D_1(\eta, R) = e^{\eta_1} D_0(\eta - \eta_1, R) = g(\eta_1) D_0(\eta - \eta_1, R), \quad (4.43a)$$

$$\chi_{1\alpha}^a(\eta, R; \boldsymbol{\varkappa}) = e^{2\eta_1} \chi_{0\alpha}^a(\eta - \eta_1, R; \boldsymbol{\varkappa}) = g^2(\eta_1) \chi_{0\alpha}^a(\eta - \eta_1, R; \boldsymbol{\varkappa}). \quad (4.43b)$$

Hence, the new sources are

$$\Upsilon_1^a(\eta) = [g(\eta_1)]^m \Upsilon_0^a(\eta - \eta_1). \quad (4.44)$$

By linearity of Eqs. (4.29), we have for the resulting counterterm prefactors,

$$\ln \mathcal{A}_1^a = [g(\eta_1)]^{m-2} \ln \mathcal{A}_0^a. \quad (4.45)$$

Note that two powers of  $g(\eta_1)$  have canceled since the definition (3.1) of the counterterm overdensity contains an explicit factor  $g^2$ . Thus, once we know the counterterm prefactor at the present epoch, we can easily find it at any other redshift by multiplying  $\ln \mathcal{A}^{\text{ctr}}$  with  $[g(z)]^{m-2}$ . This reproduces the scaling (3.18) already encountered in Sec. 3.

In Fig. 8 we illustrate the typical behavior of  $\mathcal{A}^{\text{kin}}$ ,  $\mathcal{A}^{\text{pot}}$  by plotting their logarithms at the present epoch for  $\zeta^{\text{kin}} = \zeta^{\text{pot}} = (1 \text{ Mpc}/h)^2$  and several values of the scaling index  $m$ . The cell radius is  $r_* = 10 \text{ Mpc}/h$  and the cosmological parameters are the same as in the Farpoint N-body simulation [73] (see Sec. 5). One makes several observations. First,  $\ln \mathcal{A}^{\text{kin}}$  and  $\ln \mathcal{A}^{\text{pot}}$  have opposite signs. Second, they both have zero first derivatives at  $\delta_* = 0$ , in agreement with the model-independent considerations in Sec. 3. Third, the counterterms are more important for overdensities  $\delta_* > 0$ . This appears natural since the overdense regions are expected to be more non-linear than the underdense ones, so the effects of the UV renormalization are larger there. We also plot the counterterms for several cell radii in Fig. 9. As

expected, the counterterms become stronger for smaller cells, though the dependence on the radius is quite weak.

The eventual values of the three model parameters  $m$ ,  $\zeta^{\text{kin}}$ ,  $\zeta^{\text{pot}}$  are to be determined from the best fit of the data. In principle, they must be the same for all cell radii  $r_*$ . In practice, however, it is more convenient to determine them independently for different cells, and check a posteriori the consistency of the measured values. On the other hand, they are taken to be common for all redshift bins. Note that in the actual fits to the PDF, one can impose priors following from the connection between  $\mathcal{A}^{\text{ctr}}$  and the counterterms of the  $n$ -point correlators discussed in Sec. 3. This strategy is illustrated in the next section.

## 5 Comparison with N-body data

In this section we compare our theoretical PDF model with the N-body data. For this purpose we use the results of cosmological Farpoint simulation [73]. The latter achieves a very high mass resolution,  $M_{\text{particle}} = 4.6 \cdot 10^7 h^{-1} M_{\odot}$ , by evolving  $12288^3$  particles in a  $1 (\text{Gpc}/h)^3$  volume. The force softening was chosen  $\sim 0.8 \text{ kpc}/h$  and the initial conditions were set at  $z_i = 200$  using the Zeldovich approximation. The simulation was run for  $\Lambda\text{CDM}$  cosmology with the Planck-2018 cosmological parameters:

$$\Omega_m = 0.310 , \quad \Omega_b = 0.049 , \quad h = 0.677 , \quad n_s = 0.967 , \quad \sigma_8 = 0.810 . \quad (5.1)$$

To accelerate the numerical computations, we use randomly downsampled simulation snapshots containing 1% of the total number of particles.

We first analyze the power spectrum in order to determine the “effective sound speed”  $\gamma$  and its dependence on redshift. We generate the linear power spectrum  $P(k)$  with the cosmological parameters of the simulation using the Boltzmann code CLASS [83] and compute one-loop correction to it with CLASS-PT [18]. We then extract the nonlinear power spectrum  $P^{\text{sim}}(k)$  from the simulation snapshots at redshifts  $z = \{0, 0.2, 0.5, 0.8, 1.0, 1.5, 2.4\}$  using the Yamamoto estimator [84] implemented in `nbodykit` [85], and fit it with the theoretical template. We restrict the fitting range of momenta by  $k_{\text{max}} = 0.3 h/\text{Mpc}$  and include the theoretical error following Ref. [36] with the correlation length  $\Delta k_{\text{corr}} = 0.1 h/\text{Mpc}$ . Inclusion of the theoretical error makes our results insensitive to the precise choice of  $k_{\text{max}}$ .

Figure 10 shows the measured values of  $\gamma$  at different redshifts together with the best power-law fit of the form (3.15a). The parameters of the fit and their correlation are

$$\gamma_0 = (1.95 \pm 0.26) (\text{Mpc}/h)^2 , \quad m = 2.26 \pm 0.21 , \quad \text{corr}(\gamma_0, m) = 0.85 . \quad (5.2)$$

We observe that these values somewhat differ from the values (3.15b) previously reported in the literature [15, 71, 77–81]. In this regard, it is worth pointing out

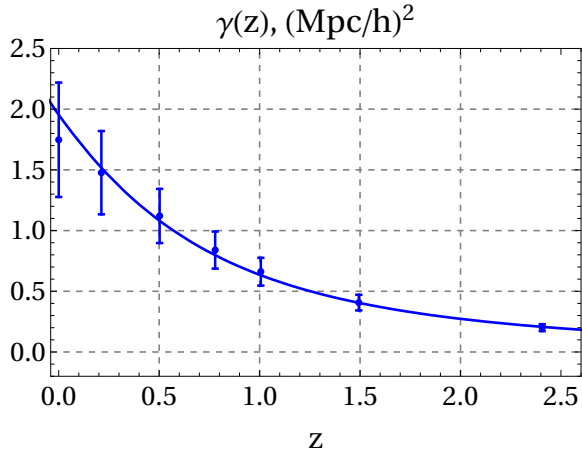


**Figure 10.** Effective sound speed measured from simulations at different redshifts. The power law fit (3.15a) with parameters (5.2) is also shown.

that the previous works used WMAP-based cosmology with higher  $h$  and lower  $\Omega_m$ . As we discuss in appendix G, this difference in the cosmological parameters is likely responsible for the shift in  $\gamma_0$  and  $m$ .

We now turn to the PDF. We cover the simulation volume with spherical cells of radius  $r_*$  placing their centers at the vertices of regular cubic grid with side  $2r_*$ . In other words, we allow the neighboring cells to touch each other, but not overlap. This is done to suppress correlations between the cells. The counts of particles in the cells are binned logarithmically in  $1 + \delta_*$  with the bin width  $\Delta \ln(1 + \delta_*) = 0.127$ . The PDF  $\mathcal{P}^{\text{sim}}(\delta_{*,n})$  in the  $n$ th bin is then estimated as the ratio of the number of cells  $\mathcal{N}_n$  falling into this bin over the total number of cells. We assume the errors to follow the Poisson statistics,  $\Delta \mathcal{P}^{\text{sim}}(\delta_{*,n}) / \mathcal{P}^{\text{sim}}(\delta_{*,n}) \simeq \mathcal{N}_n^{-1/2}$ , and be uncorrelated between the bins. These simplifying assumptions appear reasonable for cells of sizes considered in this work. A more careful treatment would include covariance which can be either extracted from large suits of N-body simulations, such as Quijote [86], or estimated theoretically [87–89]. We leave inclusion of covariance for future.

The Zeldovich initial conditions are known to affect the PDF measured in N-body simulations through long-lived transients [46, 90, 91]. In appendix H we estimate the systematic error in  $\mathcal{P}^{\text{sim}}$  induced by this effect and impose a quality cut: we use only the PDF data for which the systematic error does not exceed the statistical uncertainty. We have found this cut to be relevant for PDF of underdensities,  $\delta_* < 0$ , for the smallest cell radius analyzed in this work  $r_* = 5 \text{ Mpc}/h$ . In all other cases the systematic error happens to be negligible.

The measured PDF is used to estimate the aspherical prefactor. We divide  $\mathcal{P}^{\text{sim}}$  by the spherical PDF, Eq. (2.12), which we calculate using the linear power spectrum. To account for the particle shot noise and the finite width of the bin, we multiply  $\mathcal{P}_{\text{sp}}(\delta_*)$  with the Poisson probability  $\mathcal{P}(\mathcal{N}|\delta_*)$  of having  $\mathcal{N}$  particles inside the cell

with a given density contrast and average over the bin. In this way we obtain  $\langle \mathcal{P}_{\text{sp}} \rangle_n$  — the spherical PDF in the  $n$ th bin. The measured aspherical prefactor is then defined as

$$\mathcal{A}_{\text{asp}}^{\text{sim}}(\delta_{*,n}) = \frac{\mathcal{P}^{\text{sim}}(\delta_{*,n})}{\langle \mathcal{P}_{\text{sp}} \rangle_n}. \quad (5.3)$$

The data on the aspherical prefactor are fitted using the theoretical model developed in the previous sections. The “fluid” part  $\mathcal{A}_{\text{asp}}^{\text{fluid}}$  is evaluated using the method described in Sec. 2. We use the open-source code `AsPy` [72] to compute the contributions of multipoles with  $1 \leq \ell \leq 9$ , whereas the cumulative contribution of high multipoles with  $\ell \geq 10$  is computed with the WKB approximation. This is then multiplied by the counterterm prefactor  $\mathcal{A}^{\text{ctr}}$  evaluated following the algorithm of Sec. 4, and the parameters  $\zeta^{\text{kin}}$ ,  $\zeta^{\text{pot}}$ ,  $m$  are fitted to reproduce  $\mathcal{A}_{\text{asp}}^{\text{sim}}$ . In the fitting procedure we impose two Gaussian correlated priors following from the fit of the power spectrum (5.2). The prior on the scaling index  $m$  is applied directly, whereas the second prior constrains the linear combination of the counterterm amplitudes  $\zeta^{\text{kin}}$  and  $\zeta^{\text{pot}}$  which appears in the second derivative of  $\mathcal{A}^{\text{ctr}}(\delta_*)$  at  $\delta_* = 0$  and is proportional to  $\gamma_0$  (see Eqs. (3.12), (3.16)). The product of the aspherical prefactor and the spherical PDF gives the model PDF  $\mathcal{P}^{\text{mod}}$ .

	$r_* = 15 \text{ Mpc}/h$	$r_* = 10 \text{ Mpc}/h$	$r_* = 7.5 \text{ Mpc}/h$	$r_* = 5 \text{ Mpc}/h$
$z = 0$	0.255	0.478	0.717	1.205
$z = 0.5$	0.151	0.283	0.425	0.714
$z = 1$	0.094	0.176	0.264	0.444
$z = 2.4$	0.035	0.066	0.098	0.165

**Table 1.** Filtered density variance  $g^2\sigma_{r_*}^2$  for the cell radii and redshifts used in the analysis.

This analysis is performed for four cell radii  $r_* = \{15, 10, 7.5, 5\} \text{ Mpc}/h$  and four redshift slices  $z = \{0, 0.5, 1.0, 2.4\}$ . The linear density variance  $g^2\sigma_{r_*}^2$  for various cell radii and redshifts is shown in Tab. 1. We consider cells of different radii separately. This is done for two reasons. First, we want to avoid cross-correlation between the corresponding PDFs. This aspect can, in principle, be addressed in future studies by taking into account the PDF covariance which is, however, outside the scope of this work. Second, our theoretical model uses the saddle-point expansion which is expected to hold in the mildly non-linear regime. Thus, we do not expect the model to work equally well for larger and smaller radii. Our goal is to assess these differences. We now describe the results.

## 5.1 Large cells

Figure 11 shows the comparison between the theoretical model and the PDF obtained from the  $N$ -body simulation for cell radii  $r_* = 15 \text{ Mpc}/h$  and  $10 \text{ Mpc}/h$ . The

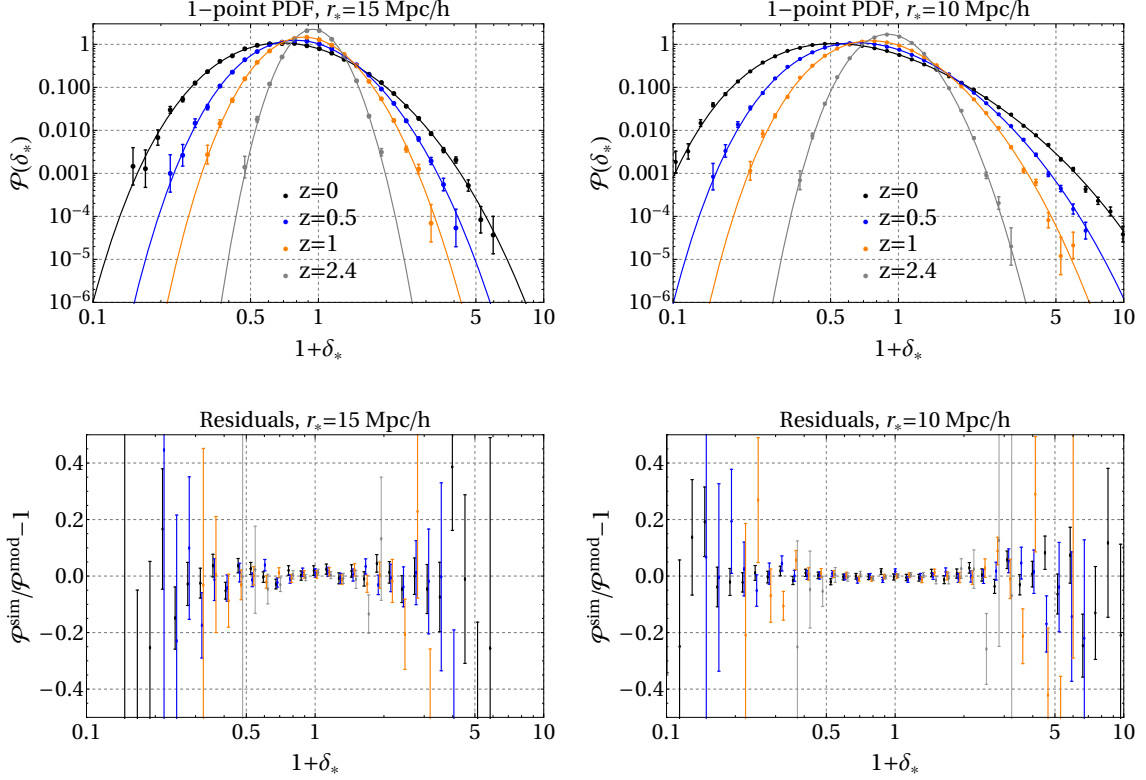


**Figure 11.** Comparison between the PDF measured in the simulation (points) and the best-fit theoretical model (lines) for cell radii  $r_* = 15 \text{ Mpc/h}$  (left) and  $r_* = 10 \text{ Mpc/h}$  (right) and for four redshift values  $z = \{0, 0.5, 1.0, 2.4\}$ . Lower panels show residuals. For presentation purposes the residuals corresponding to different redshifts are slightly shifted in the horizontal direction.

agreement is very good with the residuals inside the statistical uncertainty of the simulations for the range of densities  $0.1 \leq 1 + \delta_* \leq 10$  and all redshifts. At moderate density contrasts  $0.5 \lesssim 1 + \delta_* \lesssim 2$  the model reproduces the PDF with per cent precision.

$r_*$ , Mpc/h	$m$	$\zeta^{\text{kin}}$	$\zeta^{\text{pot}}$	$\chi^2/N_{\text{dof}}$	$\gamma_0$
15	$2.23 \pm 0.15$	$0.53 \pm 0.54$	$-2.6 \pm 1.4$	72/82	$2.04 \pm 0.16$
10	$2.14 \pm 0.10$	$0.48 \pm 0.29$	$-2.03 \pm 0.69$	108/110	$1.73 \pm 0.08$

**Table 2.** Best fit parameters of the counterterm model,  $\chi^2$  per number of degrees of freedom, and the derived effective speed of sound  $\gamma_0$  for large cell radii.

The good quality of the fit is confirmed by the values of  $\chi^2$  listed in Table 2. This table also summarizes the fitted parameters  $m$ ,  $\zeta^{\text{kin}}$ ,  $\zeta^{\text{pot}}$ . We observe that they coincide for the two radii within the error bars. This provides a consistency check of our model since, as mentioned in Sec. 4.3, they are expected to be  $r_*$ -independent.

Last column contains the derived parameter  $\gamma_0$  calculated from the second derivative of the counterterm prefactor at  $\delta_* = 0$ . We see that for  $r_* = 10 \text{ Mpc}/h$  the PDF prefers slightly lower best-fit values of  $\gamma_0$  and  $m$  than those derived from the power spectrum (see Eq. (5.2)), though still within one standard deviation of the latter. It is also worth noting that the error bars listed in Table 2 suggest that PDF may provide a better precision in determination of these parameters. However, a proper treatment of uncertainties should include the theoretical error of the model associated with two-loop contributions into the prefactor (see below) whose estimation is outside the scope of this paper.

As another consistency check, we compute the norm, mean and variance from the theoretically constructed PDF. These are listed in Table 3. We see that the deviations of the norm from unity and the mean from zero never exceed a few  $\times 10^{-3}$ . The non-linear density variance extracted from the PDF matches with per cent accuracy the result of the 1-loop EFT calculation (last column in the table). This is consistent with the discussion in Sec. 3 and provides a non-trivial confirmation of validity of the saddle-point expansion. Note that in our method the non-linear variance is not used as an input, but instead comes as the result of the theoretical modeling. Only its counterterm part is fitted from the data.

		norm - 1	$\langle \delta_* \rangle$	$\langle \delta_*^2 \rangle$	$\sigma_{\text{EFT}}^2$	$\langle \delta_*^3 \rangle / \langle \delta_*^2 \rangle^2$
$r_* = 15 \text{ Mpc}/h$	$z = 0$	$-6.2 \cdot 10^{-3}$	$-7.1 \cdot 10^{-3}$	0.260	0.262	3.35
	$z = 0.5$	$-2.9 \cdot 10^{-3}$	$-3.1 \cdot 10^{-3}$	0.153	0.154	3.30
	$z = 1$	$-1.3 \cdot 10^{-3}$	$-1.3 \cdot 10^{-3}$	0.095	0.095	3.27
	$z = 2.4$	$-3.3 \cdot 10^{-5}$	$-5.6 \cdot 10^{-5}$	0.035	0.035	3.23
$r_* = 10 \text{ Mpc}/h$	$z = 0$	$-3.7 \cdot 10^{-4}$	$-2.1 \cdot 10^{-3}$	0.533	0.532	3.63
	$z = 0.5$	$1.2 \cdot 10^{-4}$	$-6.7 \cdot 10^{-4}$	0.306	0.304	3.65
	$z = 1$	$2.8 \cdot 10^{-4}$	$-2.9 \cdot 10^{-4}$	0.185	0.185	3.56
	$z = 2.4$	$3.3 \cdot 10^{-4}$	$6.4 \cdot 10^{-5}$	0.067	0.067	3.45

**Table 3.** The norm, mean, variance and skewness from the best-fit theoretical PDF as well as the filtered variance computed using the 1-loop in the EFT power-spectrum.

In the last column of Table 3 we also present the skewness  $S_3 \equiv \langle \delta_*^3 \rangle / \langle \delta_*^2 \rangle^2$  computed from the PDF. This can be contrasted with the tree-level result:  $S_3^{\text{tree}} = 3.21$  for  $r_* = 15 \text{ Mpc}/h$  and  $3.39$  for  $r_* = 10 \text{ Mpc}/h$ . We see that the full skewness is larger than the tree-level contribution and has mild but significant dependence on the redshift. It would be interesting to compare these results with the perturbative EFT calculation.

Our counterterm model involves several choices which are not unique. One of them is the choice of the shell-crossing momentum  $k_{\text{sc}}$ . We have re-fitted the PDF using alternative definitions of  $k_{\text{sc}}$  which we implemented by replacing the growth

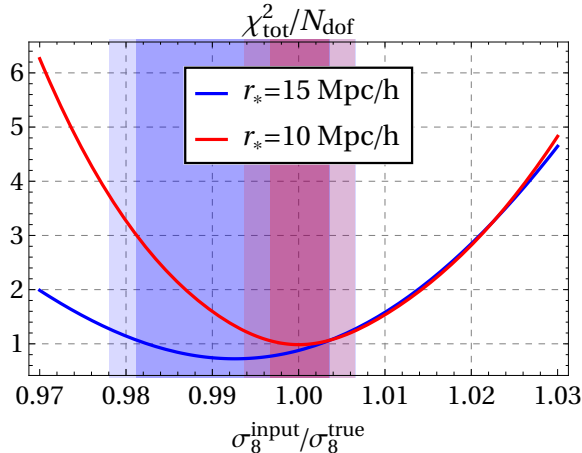


**Figure 12.** Quality of the fit of the measured PDF with the theoretical model computed using the rescaled value of  $\sigma_8$ . Shaded bands show the  $1\sigma$  (dark) and  $2\sigma$  (light) intervals around the best-fit values. Note that the upper boundaries of the blue and magenta bands almost coincide.

factor  $D_*$  in the counterterm sources (4.39) with  $D_{\parallel}$  or  $D_{\perp}$  defined in appendix F. We found almost identical results: the best-fit PDFs differ from our baseline model by less than 1% even at the tails. This robustness with respect to the choice of  $k_{\text{sc}}$  is partially due to the small best-fit value of  $(m - 2)$  in the Planck cosmology which suppresses the sensitivity of the PDF to the position-dependent growth factor.

One more choice is the split of the counterterm stress into kinetic and potential parts with independent amplitudes  $\zeta^{\text{kin}}$  and  $\zeta^{\text{pot}}$ . One may wonder if this freedom can be reduced. We study this possibility in appendix I where we find that setting one of  $\zeta^{\text{kin}}$  or  $\zeta^{\text{pot}}$  to zero can actually provide a good quality of the fit. Moreover, the counterterm prefactor for  $\zeta^{\text{pot}} = 0$  happens to be very close to the Model 2 of [71] which explains the phenomenological success of this model. On the other hand, a reduce model with  $\zeta^{\text{kin}} = \zeta^{\text{pot}}$  cannot reproduce the data with required precision. All in all, we believe that keeping  $\zeta^{\text{kin}}$  and  $\zeta^{\text{pot}}$  as independent free parameters is physically motivated and more precise data may require non-zero values for both of them. On the other hand, introducing more free parameters<sup>16</sup> is unlikely to add anything to the quality of the fit.

One might be worried that having three free parameters precludes the model from being predictive. This is not the case as demonstrated by the following exercise. We artificially change the amplitude of the linear power spectrum, traditionally parameterized by  $\sigma_8$ , and use the rescaled power spectrum to compute the theoretical PDF. As before, we adjust  $m$ ,  $\zeta^{\text{kin}}$ ,  $\zeta^{\text{pot}}$  to best fit the data. Despite this freedom, we find that the quality of the fit quickly degrades when  $\sigma_8$  deviates from its true

<sup>16</sup>Recall that the most general expression for the counterterm stress allowed by EFT can contain arbitrary functions of the density and the tidal tensor.

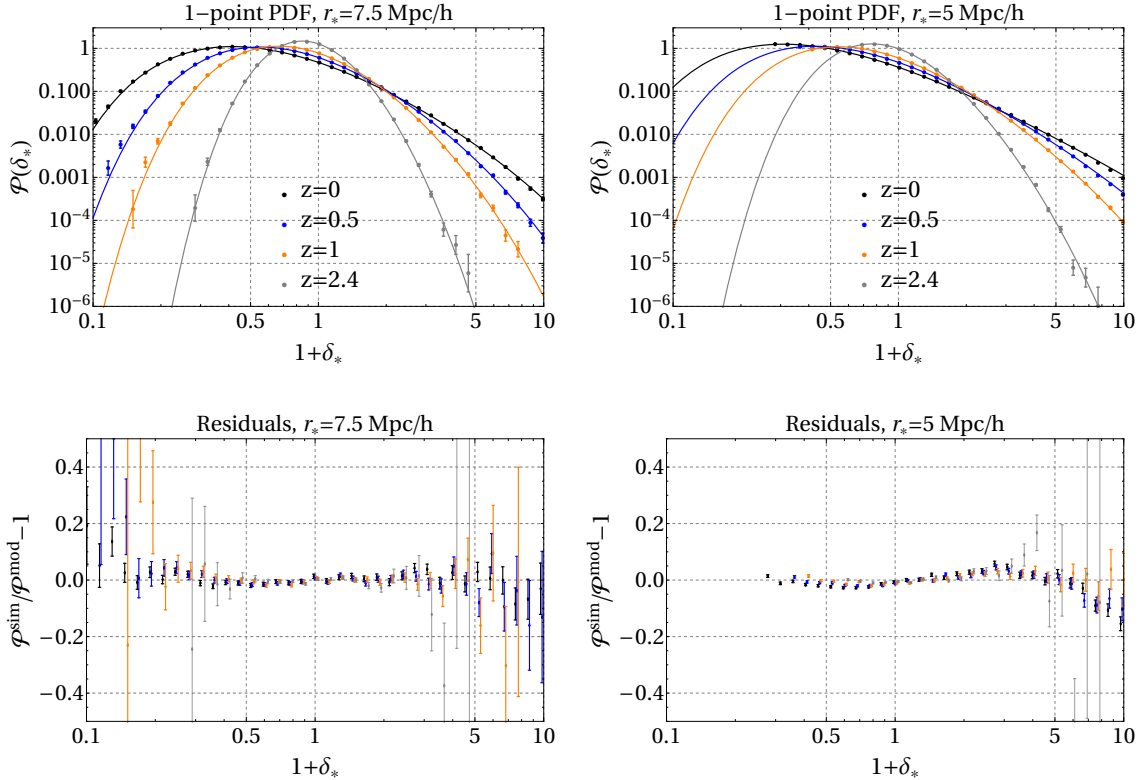


**Figure 13.** Comparison between the PDF measured in the simulation (points) and the best-fit theoretical model (lines) for cell radii  $r_* = 7.5 \text{ Mpc}/h$  (left) and  $r_* = 5 \text{ Mpc}/h$  (right) and for four redshift values  $z = \{0, 0.5, 1.0, 2.4\}$ . Lower panels show residuals. For presentation purposes the residuals corresponding to different redshifts are slightly shifted in the horizontal direction.

value, see Fig. 12. The figure suggests that our PDF model is highly sensitive to the value of  $\sigma_8$ , perhaps at sub-per cent level. This statement, however, should be taken with a grain of salt since the proper assessment of the sensitivity must include an estimate of the theoretical error which we leave for future.

## 5.2 Small cells

We now repeat the fitting procedure for cells of smaller radii  $r_* = 7.5 \text{ Mpc}/h$  and  $5 \text{ Mpc}/h$ . In the latter case we impose a lower cut on the density contrast,  $(1 + \delta_*)_{\text{min}} = \{0.28, 0.36, 0.44, 0.6\}$  at  $z = \{0, 0.5, 1.0, 2.4\}$  to suppress the systematics in the N-body data due to the use of Zeldovich initial conditions (see appendix H).

Upper panels in Fig. 13 suggest that the model still captures the behavior of the PDF quite well. However, when looking at the residuals, we start seeing tensions. The difference between the best-fit model and the measured PDF reaches  $\sim 5\%$  which is well beyond the statistical uncertainties. This discrepancy is reflected in the large  $\chi^2$  listed in Table 4. There are also clear tensions between the values of  $m$  and

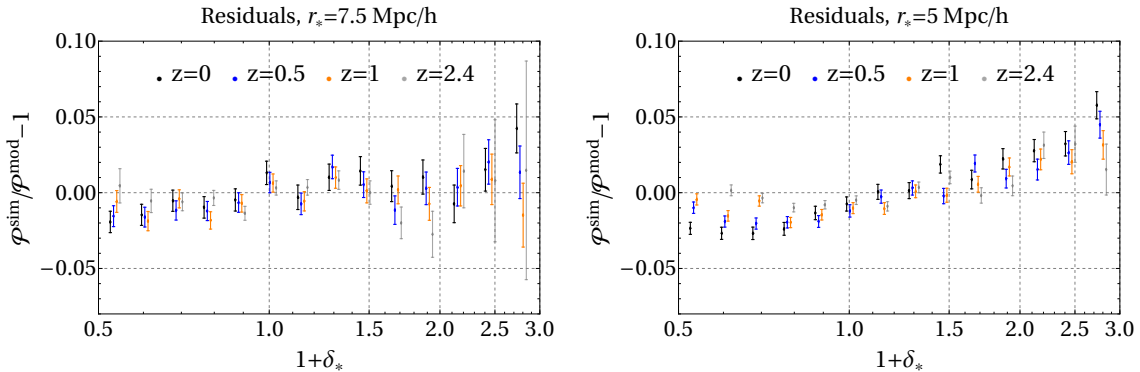


**Figure 14.** Residuals in the central region of densities between the PDF extracted from the N-body simulation and the theoretical model proposed in this paper. The cell radii are  $r_* = 7.5 \text{ Mpc}/h$  (left) and  $r_* = 5 \text{ Mpc}/h$  (right). The redshift values are given in the legend.

$\gamma_0$  for different cell radii implying that the model fails to reproduce the data with required precision.

$r_*$ , Mpc/h	$m$	$\zeta^{\text{kin}}$	$\zeta^{\text{pot}}$	$\chi^2/N_{\text{dof}}$	$\gamma_0$
7.5	$2.37 \pm 0.06$	$1.06 \pm 0.18$	$-0.49 \pm 0.36$	225/125	$1.71 \pm 0.05$
5	$2.12 \pm 0.02$	$0.95 \pm 0.06$	$-0.13 \pm 0.12$	965/100	$1.57 \pm 0.02$

**Table 4.** Best fit parameters of the counterterm model,  $\chi^2$  per number of degrees of freedom, and the derived effective speed of sound  $\gamma_0$  for small cell radii.

To understand the cause of this failure, we zoom on the central part of the density range in Fig. 14. We observe that the residuals exhibit a linear trend at  $\delta_* = 0$ . For  $r_* = 5 \text{ Mpc}/h$  we also see that  $\mathcal{P}^{\text{sim}}/\mathcal{P}^{\text{mod}}|_{\delta_*=0}$  significantly deviates from 1. Both these discrepancies somewhat weaken at larger redshifts. Such behavior cannot be attributed to a deficiency in the counterterm model. Indeed, in Sec. 3 we derived that, independently of its modeling, the one-loop counterterm can affect only the second and higher derivatives of the PDF at  $\delta_* = 0$ .

Thus, we interpret the discrepancy as the first detection of the two-loop corrections to the PDF. It is encouraging to find that they are relatively suppressed even down to cell radii as small as  $5 \text{ Mpc}/h$ . However, they clearly must be taken into account in future analysis of the PDF at these scales. A precise calculation of the two-loop corrections appears challenging. A more feasible approach will be to estimate them approximately and include in the PDF model as the theoretical uncertainty in the spirit of [36]. We leave this interesting task for future.

## 6 Conclusions

In this work we developed an analytic description of the non-perturbative one-point matter PDF, supplementing the approach of [71] with a physically motivated model for the one-loop counterterm prefactor. It is based on modeling the counterterm stress tensor which renormalizes the effect of short-wavelength modes on the saddle-point spherical collapse solution. We have validated the model using the data from high-resolution Farpoint simulation [73] and found a per cent level agreement down to cell radii  $r_* = 10 \text{ Mpc}/h$  and redshift  $z = 0$ .

The model contains three redshift-independent free parameters that in the spirit of EFT of LSS must be fitted from the data. Two combinations of these parameters already appear in the EFT template for the matter power spectrum. Thus, if the power spectrum is measured with high precision, our PDF model adds only a single parameter on top, which can be further connected to the bispectrum counterterms. In practice, however, as our comparison with N-body data indicates, the PDF can provide comparable or better constraints on the counterterm coefficients than the correlation functions. This suggests doing a joint analysis or using information from the power spectrum and bispectrum as priors when fitting the PDF.

For cells of radius  $5 \text{ Mpc}/h < r_* < 10 \text{ Mpc}/h$  we detected a few per cent deviations between the model and the N-body data which we identified as the two-loop correction. The smallness of this corrections is encouraging. Still, it is significant and may become visible even at larger radii with real or N-body data with larger statistics. Rather than trying to calculate it precisely, a more promising path would be to include it as the theoretical uncertainty in the one-loop PDF template. We plan to explore this interesting direction in future.

The matter PDF by itself is not directly observable. More work is needed to connect it to the CiC statistics of galaxies. This will require inclusion of redshift-space distortions and galaxy bias. Our analysis of renormalization naturally reveals a picture of nonlinear short-scale modes evolving along the flow lines of the background saddle-point solution. This picture appears similar to that used in the Lagrangian approach to the PDF biasing proposed in [62]. It will be very interesting to explore this connection in detail.

Another important task is inclusion of the PDF covariance which is crucial for its application to constraining the cosmological parameters or theories beyond  $\Lambda$ CDM. In our work we restricted to non-intersecting cells which are essentially uncorrelated. With the proper treatment of covariance the statistical power of PDF can be increased by allowing for overlapping cells. Interesting progress in theoretical modeling of PDF has been made recently in [87–89]. Alternatively, the covariance can be extracted from large suits of N-body simulations, such as Quijote [86].

Our approach can be applied to other non-perturbative statistics, such as generalizations of the PDF using a non-top-hat window function [58] and multiple

cells [92], or correlations between the non-linear matter density and long-wavelength modes [49]. Yet one more promising route is modeling of the lensing shear and convergence PDF [61, 93]. Finally, counts-in-cells are closely related to the  $k$ -nearest-neighbor [94, 95] and the void size [96] distribution functions. We believe our work sets firm grounds for analytical understanding of these interesting observables.

**Acknowledgments** We are indebted to Nicholas Frontiere and Thomas Uram for assistance in the use of the Farpoint simulation data. We thank Niayesh Afshordi, Neal Dalal, Alexander Kaurov, Nickolas Kokron and Mehrdad Mirbabayi for fruitful discussions. The work of A.C. is supported by the RFBR grant 20-02-00982. The work of S.S. is supported by the Natural Sciences and Engineering Research Council (NSERC) of Canada. Research at Perimeter Institute is supported in part by the Government of Canada through the Department of Innovation, Science and Economic Development Canada and by the Province of Ontario through the Ministry of Colleges and Universities. This research was enabled in part by support provided by Compute Ontario ([www.computeontario.ca](http://www.computeontario.ca)) and Digital Research Alliance of Canada ([alliancecan.ca](http://alliancecan.ca)). The numerical analysis of this work was partially performed on the Helios cluster at the Institute for Advanced Study.

## A Conventions

We use the same conventions as in [71]. For completeness, we summarize them here.

We define the Fourier transform as,

$$\delta(\mathbf{x}) = \int_{\mathbf{k}} \delta(\mathbf{k}) e^{i\mathbf{k}\cdot\mathbf{x}}, \quad (\text{A.1})$$

where the integration measure in momentum space is

$$\int_{\mathbf{k}} = \int \frac{d^3k}{(2\pi)^3}. \quad (\text{A.2})$$

We also use the concise notation for the radial integral in momentum space,

$$\int [dk] = \int_0^\infty \frac{k^2 dk}{(2\pi)^3}, \quad (\text{A.3})$$

The power spectrum is defined as,

$$\langle \delta(\mathbf{k}) \delta(\mathbf{k}') \rangle = (2\pi)^3 \delta_{\mathbf{D}}(\mathbf{k} + \mathbf{k}') P(k), \quad (\text{A.4})$$

where  $\delta_{\mathbf{D}}(\mathbf{k})$  is the Dirac delta-function.

We use the following definition for the spherical harmonics:

$$Y_0(\theta, \phi) = 1, \quad (\text{A.5a})$$

$$Y_{\ell m}(\theta, \phi) = \frac{(-1)^{\ell+m}}{2^\ell \ell!} \left[ \frac{2\ell+1}{4\pi} \frac{(\ell-|m|)!}{(\ell+|m|)!} \right]^{1/2} e^{im\phi} (\sin \theta)^{|m|} \left( \frac{d}{d \cos \theta} \right)^{\ell+|m|} (\sin \theta)^{2\ell},$$

$$\ell > 0, \quad -\ell < m < \ell. \quad (\text{A.5b})$$

They obey the relations,

$$\Delta_{\Omega} Y_{\ell m} = -\ell(\ell + 1) Y_{\ell m} , \quad Y_{\ell m}(-\mathbf{n}) = (-1)^{\ell} Y_{\ell m}(\mathbf{n}) , \quad Y_{\ell m}^*(\mathbf{n}) = Y_{\ell, -m}(\mathbf{n}) , \quad (\text{A.6})$$

where  $\Delta_{\Omega}$  is the the Laplace–Beltrami operator on the 2-dimensional sphere. All harmonics are orthogonal and normalized to 1 when integrated over a 2d sphere, except the monopole that has the norm  $4\pi$ ,

$$\int d\Omega Y_{\ell m} Y_{\ell' m'}^* = (4\pi)^{\delta_{0\ell}} \delta_{\ell\ell'} \delta_{mm'} , \quad (\text{A.7})$$

where  $\delta_{ij}$  is the Kronecker delta symbol.

We expand the fields over spherical harmonics in position and Fourier space as,

$$\delta(\mathbf{x}) = \delta_0(r) + \sum_{\ell>0} \sum_{m=-\ell}^{\ell} \delta_{\ell m}(r) Y_{\ell m}(\mathbf{x}/r) , \quad (\text{A.8a})$$

$$\delta(\mathbf{k}) = \delta_0(k) + \sum_{\ell>0} \sum_{m=-\ell}^{\ell} (-i)^{\ell} \delta_{\ell m}(k) Y_{\ell m}(\mathbf{k}/k) . \quad (\text{A.8b})$$

Due to the relations (A.6) we have,

$$(\delta_{\ell m}(r))^* = (\delta_{\ell, -m}(r)) , \quad (\delta_{\ell m}(k))^* = (\delta_{\ell, -m}(k)) . \quad (\text{A.9})$$

The coefficient functions in the above expansions are related by,

$$\delta_{\ell m}(r) = 4\pi \int [dk] j_{\ell}(kr) \delta_{\ell m}(k) , \quad (\text{A.10})$$

where  $j_{\ell}(x)$  is the spherical Bessel function of order  $\ell$ . It is related to the Bessel function of the first kind via

$$j_{\ell}(x) = \sqrt{\frac{\pi}{2x}} J_{\ell+1/2}(x) . \quad (\text{A.11})$$

The first few functions are,

$$j_0(x) = \frac{\sin x}{x} , \quad j_1(x) = \frac{\sin x}{x^2} - \frac{\cos x}{x} , \quad j_2(x) = \left( -\frac{1}{x} + \frac{3}{x^3} \right) \sin x - \frac{3}{x^2} \cos x . \quad (\text{A.12})$$

Spherical Bessel functions  $j_{\ell}(kr)$  with different arguments  $k$  form an orthogonal basis on the half-line with the normalization

$$\int_0^{\infty} dr r^2 j_{\ell}(k'r) j_{\ell}(kr) = \frac{\pi}{2k^2} \delta_{\text{D}}(k - k') . \quad (\text{A.13})$$

They are eigenmodes of the radial part of the Laplace operator,

$$\partial_r^2 j_{\ell}(kr) + \frac{2}{r} \partial_r j_{\ell}(kr) - \frac{\ell(\ell + 1)}{r^2} j_{\ell}(kr) = -k^2 j_{\ell}(kr) . \quad (\text{A.14})$$

## B Spherical PDF

In this appendix we derive the ‘‘spherical’’ part of the PDF (2.16) accounting for the contribution of the saddle configuration and the monopole fluctuations around it. We start from the saddle-point equations for the integrals (2.7), (2.8) in the limit  $g \rightarrow 0$ . Taking derivatives of the expressions in the exponent with respect to  $\delta_L$  and  $\lambda$  we obtain,

$$\frac{\delta_L(\mathbf{k})}{P(k)} + \lambda \frac{\partial \bar{\delta}_W}{\partial \delta_L(\mathbf{k})} = 0, \quad (\text{B.1a})$$

$$\bar{\delta}_W[\delta_L] = \delta_*. \quad (\text{B.1b})$$

Since the window function and the power spectrum are invariant under rotations and assuming that the solution to (B.1) is unique, we conclude that the saddle-point configuration  $\hat{\delta}_L(k)$  is spherically symmetric. This implies that  $\hat{\delta}_L(k)$  and  $\bar{\delta}_W$  are related by the equations of spherical collapse which are exactly solvable.<sup>17</sup> The solution is conveniently written in terms of relations between the linear and nonlinear density contrasts taken at the same time slice and averaged over the Lagrangian and the Eulerian radii, respectively,

$$\bar{\delta}(r) = f(\bar{\delta}_L(R)), \quad \bar{\delta}_L(R) = F(\bar{\delta}(r)), \quad R = r(1 + \bar{\delta}(r))^{1/3}, \quad (\text{B.2})$$

where

$$\bar{\delta}(r) = \frac{3}{r^3} \int_0^r r'^2 dr' \delta(r'), \quad \bar{\delta}_L(R) = \frac{3}{R^3} \int_0^R R'^2 dR' \delta_L(R'). \quad (\text{B.3})$$

For the EdS cosmology the mapping (B.2) does not depend on time and the functions  $f, F$  are defined as follows. Introduce four functions,

$$\mathcal{F}_+(\theta) = \frac{9(\theta - \sin \theta)^2}{2(1 - \cos \theta)^3} - 1, \quad \mathcal{G}_+(\theta) = \frac{3}{20}[6(\theta - \sin \theta)]^{2/3}, \quad (\text{B.4a})$$

$$\mathcal{F}_-(\theta) = \frac{9(\text{sh } \theta - \theta)^2}{2(\text{ch } \theta - 1)^3} - 1, \quad \mathcal{G}_-(\theta) = -\frac{3}{20}[6(\text{sh } \theta - \theta)]^{2/3}. \quad (\text{B.4b})$$

Then

$$f(x) = \begin{cases} \mathcal{F}_+(\mathcal{G}_+^{-1}(x)), & x > 0 \\ \mathcal{F}_-(\mathcal{G}_-^{-1}(x)), & x < 0 \end{cases}, \quad F(x) = \begin{cases} \mathcal{G}_+(\mathcal{F}_+^{-1}(x)), & x > 0 \\ \mathcal{G}_-(\mathcal{F}_-^{-1}(x)), & x < 0 \end{cases}, \quad (\text{B.5})$$

where  $\mathcal{G}_+^{-1}$  stands for the inverse function to  $\mathcal{G}_+$ , etc. The derivation of these expressions can be found, e.g., in [71] (see also appendix H). We show the plot of the function  $F$  in the left panel of Fig. 15. For small density contrasts we have,

$$F(\delta_*) = \delta_* - \frac{17}{21}\delta_*^2 + \frac{2815}{3969}\delta_*^3 + O(\delta_*^4). \quad (\text{B.6})$$

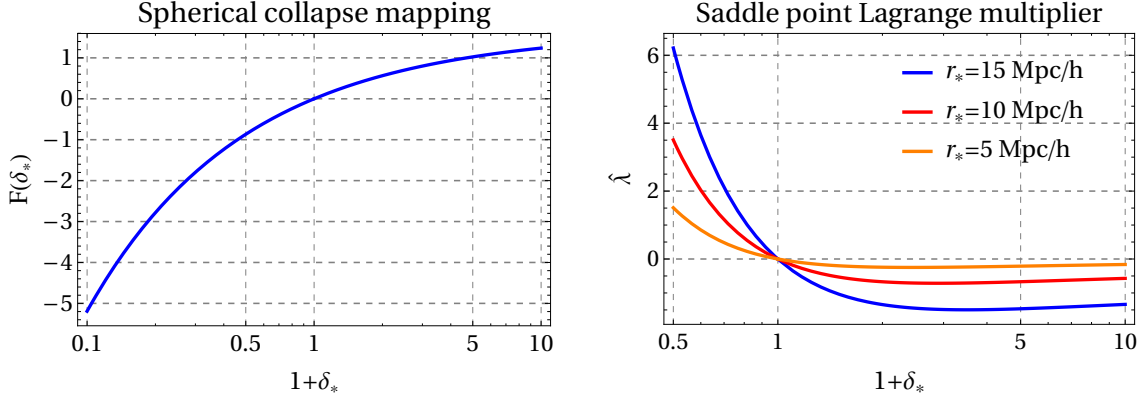


**Figure 15.** *Left:* The spherical collapse map  $F(\delta_*)$  for EdS cosmology. *Right:* The saddle-point value of the Lagrange multiplier  $\hat{\lambda}$  as function of density contrast for several cell radii.

The mapping (B.2) allows us to find the saddle point and perform the integral over spherical fluctuations exactly. The shortest way to do it is to notice that for spherically symmetric configurations we can replace the  $\delta$ -function (2.6) with a constraint on the linear density contrast,

$$\delta_D(\delta_* - \bar{\delta}_W[\delta_L]) = C[\delta_*, \delta_L] \cdot \delta_D(F(\delta_*) - \bar{\delta}_L(R_*)) , \quad (\text{B.7})$$

where  $R_*$  is defined in (2.15) and the coefficient

$$C[\delta_*, \delta_L] = F'(\delta_*) - \frac{R_* \partial_R \bar{\delta}_L(R_*)}{3(1 + \delta_*)} \quad (\text{B.8})$$

has been inserted to ensure that the integral of the r.h.s. over  $\delta_*$  gives unity. This yields for the spherical part of the PDF,

$$\begin{aligned} \mathcal{P}_{\text{sp}}(\delta_*) &= \mathcal{N}_0^{-1} \int_{\text{spherical}} \mathcal{D}\delta_L \exp \left\{ -\frac{4\pi}{g^2} \int [dk] \frac{|\delta_L(k)|^2}{2P(k)} \right\} \delta_D(\delta_* - \bar{\delta}_W[\delta_L]) \\ &= \mathcal{N}_0^{-1} \int_{-i\infty}^{i\infty} \frac{d\tilde{\lambda}}{2\pi i g^2} \exp \left\{ \frac{\tilde{\lambda} F(\delta_*)}{g^2} \right\} \\ &\quad \times \int_{\text{spherical}} \mathcal{D}\delta_L C[\delta_*, \delta_L] \exp \left\{ -\frac{4\pi}{g^2} \int [dk] \left[ \frac{|\delta_L(k)|^2}{2P(k)} + \tilde{\lambda} W_{\text{th}}(kR_*) \delta_L(k) \right] \right\}, \end{aligned} \quad (\text{B.9})$$

where in the second line we used Eq. (B.7) and Fourier-transformed the  $\delta$ -function. This is a Gaussian integral with a prefactor  $C[\delta_*, \delta_L]$  which is a linear function of  $\delta_L$ .

<sup>17</sup>We assume that the saddle-point solution does not experience shell crossing. Strictly speaking, this assumption is violated at  $z = 0$  for extreme overdensities  $\delta_* \gtrsim 7$  considered in this paper. Still, the shell crossing occurs in the center of the cell and does not invalidate the spherical collapse mapping between average densities discussed below.

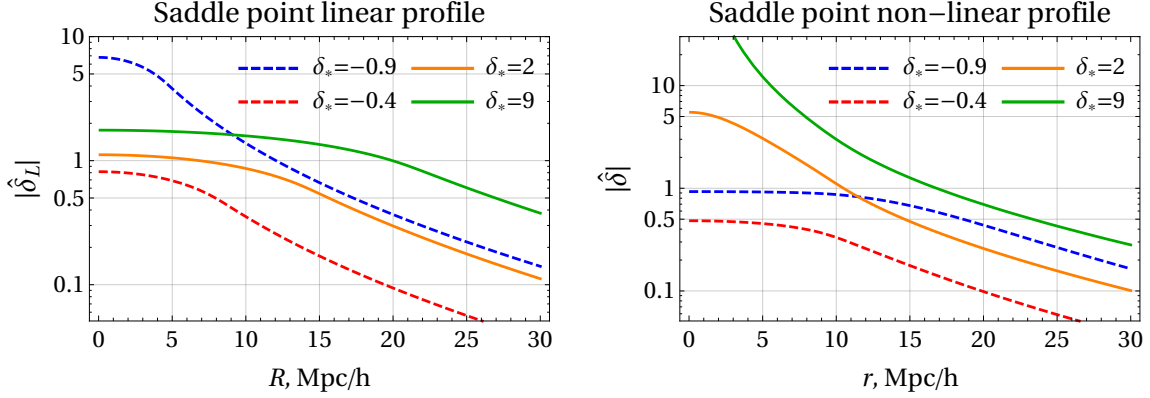


**Figure 16.** Saddle-point linear profile in Lagrangian position space (left) and non-linear profile at  $z = 0$  as a function of an Eulerian radius (right) for several values of  $\delta_*$ . For  $\delta_* < 0$ , the absolute value of the negative density contrast is shown (dashed lines). The cell radius is  $r_* = 10 \text{ Mpc}/h$ .

Such integrals are exactly evaluated by the saddle point method. It is straightforward to find the saddle configuration,

$$\hat{\delta}_L(k) = \frac{F(\delta_*)}{\sigma_{R_*}^2} P(k) W_{\text{th}}(kR_*), \quad (\text{B.10a})$$

$$\hat{\lambda} = -\frac{F(\delta_*)}{\sigma_{R_*}^2}, \quad (\text{B.10b})$$

where the density variance  $\sigma_{R_*}^2$  is given by Eq. (2.14). The resulting linear density profiles in the Lagrangian space  $\hat{\delta}_L(R)$  for  $\Lambda\text{CDM}$  power spectrum and  $r_* = 10 \text{ Mpc}/h$  are shown on the left of Fig. 16 for several values of  $\delta_*$ . On the right we also show the corresponding non-linear profiles  $\hat{\delta}(r)$  in Eulerian space at  $z = 0$  obtained by applying the map (B.2), (B.3). For  $\delta_* \gtrsim 7$  the linear density profile in the center exceeds the EdS collapse threshold 1.686 and thus the innermost part of  $\hat{\delta}(r)$  diverges. This, however, does not invalidate the map between the averaged densities, as noted in footnote 17.

Putting the expressions (B.10) back into (B.9) we obtain,

$$\mathcal{P}_{\text{sp}}(\delta_*) = \frac{\hat{C}(\delta_*)}{\sqrt{2\pi g^2 \sigma_{R_*}^2}} e^{-\frac{F^2(\delta_*)}{2g^2 \sigma_{R_*}^2}}. \quad (\text{B.11})$$

Here  $\hat{C}(\delta_*)$  is the coefficient  $C[\delta_*, \delta_L]$  evaluated at the saddle point,

$$\hat{C}(\delta_*) = F'(\delta_*) + \frac{F(\delta_*)}{1 + \delta_*} \left(1 - \frac{\xi_{R_*}}{\sigma_{R_*}^2}\right) \quad (\text{B.12a})$$

with

$$\xi_{R_*} = 4\pi \int [dk] \frac{\sin kR_*}{kR_*} W_{\text{th}}(kR_*) P(k). \quad (\text{B.12b})$$

Finally, introducing the variable  $\nu$  as in (2.13) and observing that  $d\nu/d\delta_* = \hat{C}(\delta_*)/\sigma_{R_*}$  brings the spherical PDF to the form (2.12). Notice that the spherical PDF is by itself normalized,  $\int \mathcal{P}_{\text{sp}}(\delta_*) d\delta_* = 1$ . On the other hand, it does not obey the zero-average condition  $\langle \delta_* \rangle_{\text{sp}} \equiv \int \delta_* \mathcal{P}_{\text{sp}}(\delta_*) d\delta_* \neq 0$ . This is, of course, due to the fact that  $\mathcal{P}_{\text{sp}}$  is not the full PDF since it does not take into account the contribution of aspherical fluctuations. As discussed in [71], the full PDF (2.16) does lead to zero average density contrast,  $\langle \delta_* \rangle \equiv \int \delta_* \mathcal{P}(\delta_*) d\delta_* = 0$ .

For calculation of the aspherical prefactor, we need the saddle-point value of the Lagrange multiplier  $\lambda$  entering into the integral of the full PDF (2.7). Comparing the Fourier representations of the two  $\delta$ -functions in (B.7), we see that it is related to the ‘‘spherical’’ Lagrange multiplier  $\tilde{\lambda}$  by the factor  $C$ . So, we have,

$$\hat{\lambda}(\delta_*) = -\frac{F(\delta_*)}{\sigma_{R_*}^2} \hat{C}(\delta_*) = -\nu \frac{d\nu}{d\delta_*}, \quad (\text{B.13})$$

Note that  $\hat{\lambda}$  depends on the density contrast and on the cell radius  $r_*$ , but is independent of the redshift. We plot it for several cell radii in the right panel of Fig. 15.

## C A fit for the aspherical prefactor

The featureless behavior of the aspherical prefactor extracted from N-body simulations in Fig. 2 suggests to fit it in the considered range of density contrasts by a polynomial in  $\ln(1 + \delta_*)$ ,

$$\mathcal{A}_{\text{asp}}^{\text{fit}} = a_0 + a_1 \ln(1 + \delta_*) + a_2 \ln^2(1 + \delta_*) + a_3 \ln^3(1 + \delta_*). \quad (\text{C.1})$$

The coefficients  $a_0, a_1$  here are not free and can be found from the following consistency conditions. First, the normalization of the PDF implies

$$\int \mathcal{P}(\delta_*) d\delta_* \approx \mathcal{A}_{\text{asp}}|_{\delta_*=0} = 1, \quad (\text{C.2})$$

where we have used Eq. (2.16) and retained only the term of the zeroth order in  $g^2$ . Second, due to the mass conservation and translation invariance the full 1-point PDF must have zero mean,

$$\langle \delta_* \rangle \equiv \int \delta_* \mathcal{P}(\delta_*) d\delta_* = 0. \quad (\text{C.3})$$

Again using Eq. (2.16) and retaining the leading contributions in  $g^2$  we obtain the identity

$$\left. \frac{d\mathcal{A}_{\text{asp}}}{d\delta_*} \right|_{\delta_*=0} = -\frac{1}{2} \left( \frac{d\delta_*}{d\nu} \right)^{-2} \left. \frac{d^2\delta_*}{d\nu^2} \right|_{\nu=0} = \frac{4}{21} - \frac{\xi_{r_*}}{\sigma_{r_*}^2}. \quad (\text{C.4})$$

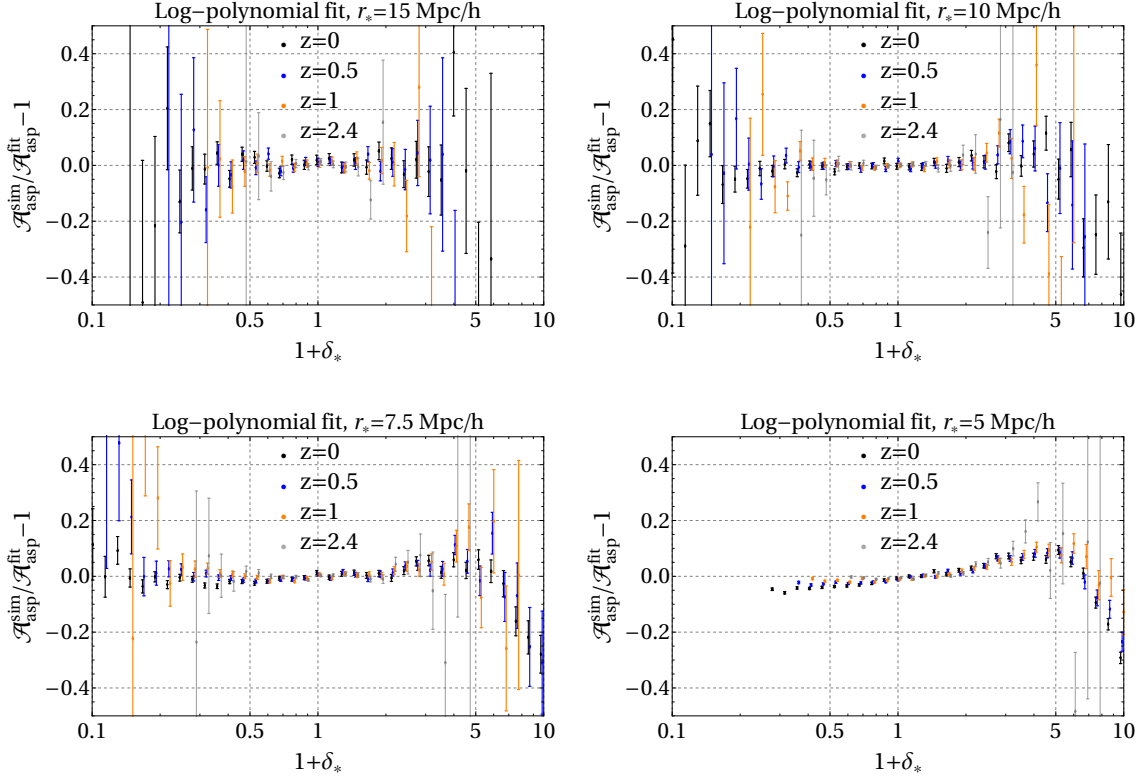


**Figure 17.** Residuals between the aspherical prefactor extracted from N-body data and the log-polynomial fit (C.1) for different redshifts and cell radii. The data for  $r_* = 5$  Mpc/h are cut at small densities as in Sec. 5.2 to suppress the systematic errors due to Zeldovich initial conditions.

Thus, we conclude that the magnitude and the slope of the aspherical prefactor at the origin are fixed, irrespective of the details of its modeling.<sup>18</sup> In particular, for the fitting function (C.1) it implies,

$$a_0 = 1, \quad a_1 = \frac{4}{21} - \frac{\xi_{r_*}}{\sigma_{r_*}^2}. \quad (\text{C.5})$$

The remaining parameters  $a_2$ ,  $a_3$  are free and we fit them to the aspherical prefactor extracted from simulations using the procedure described in Sec. 5. We choose these parameters to be redshift-independent, but allow them to vary with the cell radius  $r_*$ . The residuals of the fit are shown in Fig. 17. The fit is quite good for the two larger radii  $r_* = 15$  Mpc/h, and 10 Mpc/h. It correctly captures the behavior of the prefactor near the origin, whereas there are some slight discrepancies in the tail. In particular, for  $r_* = 10$  Mpc/h the fit is in  $1.9\sigma$  tension with the data as follows from the  $\chi^2$ -value listed in the Table 5.

<sup>18</sup>This is true for the one-loop prefactor. Higher loops introduce corrections of order  $g^2$ , see Sec. 5.2.

$r_*$ , Mpc/h	$a_1$	$a_2$	$a_3$	$\chi^2/N_{\text{dof}}$
15	-0.535	$-0.020 \pm 0.01$	$0.054 \pm 0.01$	68.5/83
10	-0.565	$0.031 \pm 0.003$	$0.034 \pm 0.002$	136/111
7.5	-0.584	$0.044 \pm 0.002$	$0.030 \pm 0.001$	344/126
5	-0.608	$0.057 \pm 0.001$	$0.0269 \pm 0.0006$	2769/101

**Table 5.** Parameters of the log-polynomial fit (C.1) to the one-loop aspherical prefactor for different cell radii.  $a_0 = 1$  for all cases, whereas  $a_1$  is computed using (C.5). Only  $a_2$  and  $a_3$  are fitted from the N-body data. The last column gives the  $\chi^2$  per number of degrees of freedom.

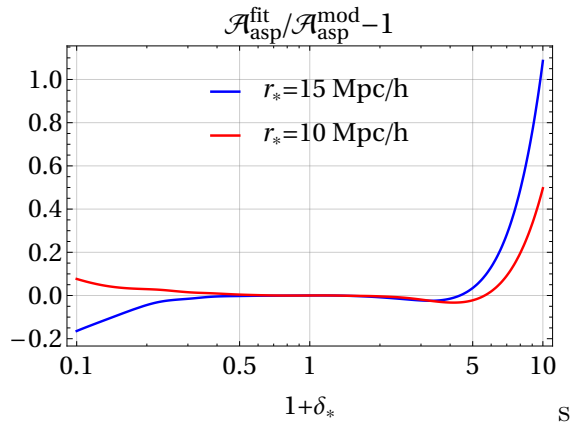


**Figure 18.** The difference between the log-polynomial fit (C.1) and the full theoretical model for the aspherical prefactor for cell radii  $r_* = 15$  Mpc/h and 10 Mpc/h at  $z = 0$ . Note that for  $r_* = 15$  Mpc/h the N-body data have large uncertainties at  $1 + \delta_* \lesssim 0.2$  and  $1 + \delta_* \gtrsim 5$ , which makes the fit at these densities poorly constrained.

We note that the performance of the log-polynomial fit is somewhat worse than of the theoretical PDF model developed in the main part of the paper. In this regard, it is instructive to compare the model and the fit directly. We do it in Fig 18 where we plot the difference between the fit (C.1) to the aspherical prefactor and the theoretically modeled value. To compute the latter we use the counterterm parameters listed in Table 2. We see that the fit is close to the theoretical model in the underdense region and at moderate overdensities. However, at large overdensities  $\delta_* \gtrsim 5$  the deviation becomes significant and reaches 40% for  $r_* = 10$  Mpc/h. It is even larger for  $r_* = 15$  Mpc/h, but here it can be partially attributed to the fact that the N-body data used in the fit are not constraining the tails of the distribution.

For smaller radii  $r_* = 7.5$  Mpc/h and  $r_* = 5$  Mpc/h the log-polynomial fit deteriorates. It is unable to reproduce the slope of the prefactor at the origin and the discrepancies at the overdense tail reach  $\sim 30\%$ . The values of  $\chi^2$  are very poor, see Table 5. In principle, the fit can be improved by letting the parameters  $a_0, a_1$

to be free and by allowing all parameters to vary with the redshift. This, however, obviously reduces its constraining power.

As discussed in Sec. 5.2, for small radii even the theoretical model fails to precisely reproduce the data due to 2-loop corrections. The crucial advantage of the theoretical model, however, is that using it we can understand the cause of the failure and develop well-defined strategies to systematically improve the accuracy.

## D Dynamical equations

We describe dark matter and baryons as a single self-gravitating fluid. In this appendix we summarize the equations for the system assuming the fluid to be pressureless. The effective stress tensor arising from short modes which experience shell crossing and are not captured by the fluid picture is considered in Sec. 4.

The standard Euler–Poisson equations read,

$$\frac{\partial \delta}{\partial t} + \partial_i((1 + \delta)u_i) = 0 , \quad (\text{D.1a})$$

$$\frac{\partial u_i}{\partial t} + \mathcal{H}u_i + (u_j \partial_j)u_i + \partial_i \Phi = 0 , \quad (\text{D.1b})$$

$$\Delta \Phi = \frac{3\mathcal{H}^2}{2} \Omega_m(t) \delta , \quad (\text{D.1c})$$

where  $t$  is the conformal time,  $\mathcal{H}$  is the conformal Hubble parameter, and  $\Omega_m(t)$  is the time-dependent matter fraction in the energy budget of the universe. We neglect vorticity and write the peculiar velocity in terms of scalar potentials,

$$u_i = -\mathcal{H} \partial_i \Psi , \quad \partial_i u_i = -\mathcal{H} \Theta , \quad \Delta \Psi = \Theta . \quad (\text{D.2})$$

Taking divergence of the Euler Eq. (D.1b) and eliminating  $\Delta \Phi$  with (D.1c) we get an evolution equation for  $\Theta$  containing  $\Psi$  and  $\delta$ . Assuming EdS cosmology, we set  $\Omega_m(t) = 1$  and switch to the time variable  $\eta$  introduced in (2.18). We now discuss the reduction of the general system (D.1) for the cases of the background spherical collapse solution, linear perturbations and second-order perturbations.

### D.1 Background evolution

The saddle-point solution is spherically symmetric. We characterize it by its non-linear profile in the Eulerian space  $(\hat{\delta}(\eta, r), \hat{\Theta}(\eta, r), \hat{\Psi}(\eta, r))$ . From (D.1) we obtain that it obeys the equations,

$$\partial_\eta \hat{\delta} - \partial_r \hat{\Psi} \partial_r \hat{\delta} - (1 + \hat{\delta}) \hat{\Theta} = 0 , \quad (\text{D.3a})$$

$$\partial_\eta \hat{\Theta} + \frac{1}{2} \hat{\Theta} - \frac{3}{2} \hat{\delta} - \partial_r \hat{\Psi} \partial_r \hat{\Theta} - \hat{\Theta}^2 + \frac{2}{r^2} (\partial_r \hat{\Psi})^2 + \frac{4}{r} \partial_r^2 \hat{\Psi} \partial_r \hat{\Psi} = 0 , \quad (\text{D.3b})$$

$$\partial_r (r^2 \partial_r \hat{\Psi}) = r^2 \hat{\Theta} . \quad (\text{D.3c})$$

This system can be solved by the standard methods performing the map to the Lagrangian space which leads to the relations (B.2) between nonlinearly and linearly evolved densities. The explicit expressions for various quantities characterizing the saddle-point background profile can be found in [71].

In this paper we often use the trajectory  $\hat{r}(\eta)$  of the shell of particles which arrive at  $r_*$  by  $\eta = 0$ . We can think of this shell as the moving boundary of the cell which, in the absence of shell crossing, contains a constant mass of matter. This implies two relations,

$$\dot{\hat{r}} = -\partial_r \hat{\Psi}(\eta, \hat{r}) , \quad \dot{\hat{\mu}} = 0 , \quad (\text{D.4})$$

where

$$\hat{\mu}(\eta) \equiv \int_0^{\hat{r}(\eta)} r^2 dr (1 + \hat{\delta}(\eta, r)) , \quad (\text{D.5})$$

and dot stands for (total) derivative w.r.t.  $\eta$ . The first relation further gives,

$$\ddot{\hat{r}} = -\partial_\eta \partial_r \hat{\Psi} + \partial_r \hat{\Psi} \partial_r^2 \hat{\Psi} \Big|_{\eta, \hat{r}} . \quad (\text{D.6})$$

It is useful to obtain the equation for  $\hat{r}$  in closed form. To this end, we multiply Eq. (D.3b) by  $r^2$  and integrate it from 0 to  $\hat{r}$ . After several simplifications using Eq. (D.3c) we obtain,

$$\hat{r}^2 \left( \partial_\eta \partial_r \hat{\Psi} - \partial_r \hat{\Psi} \partial_r^2 \hat{\Psi} + \frac{1}{2} \partial_r^3 \hat{\Psi} \right) \Big|_{\eta, \hat{r}} - \frac{3}{2} \left( \hat{\mu} - \frac{\hat{r}^3}{3} \right) = 0 . \quad (\text{D.7})$$

In the brackets we recognize the first and second time-derivatives of  $\hat{r}$ . Thus, we arrive at the equation,

$$\ddot{\hat{r}} + \frac{\dot{\hat{r}}}{2} - \frac{\hat{r}}{2} + \frac{3\hat{\mu}}{2\hat{r}^2} = 0 . \quad (\text{D.8})$$

This is nothing but the Newton's law for a particle moving together with the cell boundary. The trajectory interpolates between  $\hat{r}(-\infty) = R_*$  and  $\hat{r}(0) = r_*$ .

## D.2 Linearized perturbations with $\ell > 0$

Next we consider the evolution of linearized aspherical fluctuations in the background of saddle point solution. We decompose all quantities into background and first-order aspherical perturbations,  $\delta = \hat{\delta} + \delta^{(1)}$ , etc., and expand the latter in spherical harmonics,

$$\delta^{(1)}(\mathbf{x}) = \sum_{\ell \geq 1} \sum_{m=-\ell}^{\ell} (-i)^\ell Y_{\ell m}(\mathbf{x}/r) \delta_{\ell m}^{(1)}(r) , \quad (\text{D.9})$$

In what follows we will omit the azimuthal ‘‘quantum number’’  $m$  since it does not appear explicitly in the equations. To linear order in perturbations, the Euler–Poisson system written in terms of the velocity potential takes the following form

$$\partial_\eta \delta_\ell^{(1)} - \Theta_\ell^{(1)} - \partial_r \hat{\Psi} \partial_r \delta_\ell^{(1)} - \hat{\Theta} \delta_\ell^{(1)} - \partial_r \hat{\delta} \partial_r \Psi_\ell^{(1)} - \hat{\delta} \Theta_\ell^{(1)} = 0, \quad (\text{D.10a})$$

$$\begin{aligned} \partial_\eta \Theta_\ell^{(1)} + \frac{1}{2} \Theta_\ell^{(1)} - \frac{3}{2} \delta_\ell^{(1)} - \partial_r \hat{\Psi} \partial_r \Theta_\ell^{(1)} - \partial_r \hat{\Theta} \partial_r \Psi_\ell^{(1)} - 2 \partial_r^2 \hat{\Psi} \Theta_\ell^{(1)} \\ + 2 \left( \partial_r^2 \hat{\Psi} - \frac{\partial_r \hat{\Psi}}{r} \right) \left( \frac{2}{r} \partial_r \Psi_\ell^{(1)} - \frac{\ell(\ell+1)}{r^2} \Psi_\ell^{(1)} \right) = 0, \end{aligned} \quad (\text{D.10b})$$

$$\partial_r^2 \Psi_\ell^{(1)} + \frac{2}{r} \partial_r \Psi_\ell^{(1)} - \frac{\ell(\ell+1)}{r^2} \Psi_\ell^{(1)} = \Theta_\ell^{(1)}. \quad (\text{D.10c})$$

This is a system of (1+1)-dimensional partial differential equations with respect to  $(\delta_\ell^{(1)}, \Theta_\ell^{(1)}, \Psi_\ell^{(1)})$ .

In setting up the initial conditions we proceed as follows. At early times the saddle-point background vanishes and the solution of the above equations reduces to

$$\delta_\ell^{(1)}(\eta, r) \rightarrow e^\eta \delta_{L,\ell}^{(1)}(r),$$

where  $\delta_{L,\ell}^{(1)}$  is a fluctuation of the linear density field. We need an orthogonal basis for such functions on the half-line which are properly normalized with respect to the radial integration measure,

$$\int_0^\infty dr r^2 \delta_{L,\ell}^{(1)}(r; k) \delta_{L,\ell}^{(1)}(r; k') = (2\pi)^3 k^{-2} \delta_D(k - k'). \quad (\text{D.11})$$

The expression on the r.h.s. is the radial delta-function compatible with the momentum-space measure  $\int [dk]$ , Eq. (A.3). A convenient basis with this property is provided by the spherical Bessel functions,

$$\delta_{L,\ell}^{(1)}(r; k) = 4\pi j_\ell(kr). \quad (\text{D.12})$$

The velocity potentials are expanded in spherical harmonics in the same way as the density, and their initial conditions follow from the adiabaticity of the linear mode,

$$\Theta_{L,\ell}^{(1)}(r; k) = \delta_{L,\ell}^{(1)}(r; k), \quad \Psi_{L,\ell}^{(1)}(r; k) = -\delta_{L,\ell}^{(1)}(r; k)/k^2. \quad (\text{D.13})$$

In setting up the initial condition for  $\Psi_{L,\ell}^{(1)}$  we have used that Bessel functions are eigenstates of the radial part of the Laplace operator, see Eq. (A.14).

### D.3 Quadratic perturbations in the monopole sector

Here we analyze the evolution of second-order monopole perturbation  $\delta_0^{(2)}(\eta, r; k_I, k_J)$  induced by two aspherical fluctuations of a given multipole  $\ell$  and momenta  $k_I, k_J$ . Expanding the Euler–Poisson equations to the quadratic order and averaging over

the angles one obtains

$$\dot{\delta}_0^{(2)} - \Theta_0^{(2)} - \partial_r \hat{\Psi} \partial_r \delta_0^{(2)} - \hat{\Theta} \delta_0^{(2)} - \partial_r \hat{\delta} \partial_r \Psi_0^{(2)} - \hat{\delta} \Theta_0^{(2)} = \Xi_\delta, \quad (\text{D.14a})$$

$$\dot{\Theta}_0^{(2)} + \frac{1}{2} \Theta_0^{(2)} - \frac{3}{2} \delta_0^{(2)} - \partial_r \hat{\Psi} \partial_r \Theta_0^{(2)} - \partial_r \hat{\Theta} \partial_r \Psi_0^{(2)} \quad (\text{D.14b})$$

$$- 2 \partial_r^2 \hat{\Psi} \Theta_0^{(2)} + \frac{4}{r} \left( \partial_r^2 \hat{\Psi} - \frac{\partial_r \hat{\Psi}}{r} \right) \partial_r \Psi_0^{(2)} = \Xi_\Theta,$$

$$\partial_r^2 \Psi_0^{(2)} + \frac{2}{r} \partial_r \Psi_0^{(2)} = \Theta_0^{(2)}, \quad (\text{D.14c})$$

where

$$\Xi_\delta = \frac{1}{r^2} \partial_r (r^2 \Upsilon_{\delta, IJ}), \quad \Xi_\Theta = \frac{1}{r^2} \partial_r (r^2 \Upsilon_{\Theta, IJ}), \quad (\text{D.15})$$

and  $\Upsilon_\delta$  and  $\Upsilon_\Theta$  are defined as

$$\Upsilon_{\delta, IJ}(\eta, r) = \frac{1}{8\pi} \delta_{\ell, I}^{(1)} \partial_r \Psi_{\ell, J}^{(1)} + (I \leftrightarrow J), \quad (\text{D.16a})$$

$$\begin{aligned} \Upsilon_{\Theta, IJ}(\eta, r) = \frac{1}{8\pi} \left[ \Theta_{\ell, I}^{(1)} \partial_r \Psi_{\ell, J}^{(1)} - \frac{2}{r} \partial_r \Psi_{\ell, I}^{(1)} \partial_r \Psi_{\ell, J}^{(1)} + \frac{2\ell(\ell+1)}{r^2} \Psi_{\ell, I}^{(1)} \partial_r \Psi_{\ell, J}^{(1)} \right. \\ \left. - \frac{\ell(\ell+1)}{r^3} \Psi_{\ell, I}^{(1)} \Psi_{\ell, J}^{(1)} \right] + (I \leftrightarrow J). \end{aligned} \quad (\text{D.16b})$$

To analyze this system, it is convenient to switch to the total monopole density combining the background and perturbations,  $\delta_0 = \hat{\delta} + \delta_0^{(2)}$ , and similarly for  $\Theta_0$  and  $\Psi_0$ . Summing (D.14) with the background Eqs. (D.3) we find the system for  $(\delta_0, \Theta_0, \Psi_0)$  which has the same form as (D.3), but with the sources  $\Xi_\delta, \Xi_\Theta$  in the continuity and Euler equations, respectively.

The rest of the analysis proceeds similarly to appendix D.1. We introduce the moving radius of the cell  $r_{\text{cell}}(\eta; k_I, k_J)$  which obeys

$$\dot{r}_{\text{cell}} = -\partial_r \Psi_0(\eta, r_{\text{cell}}) \quad (\text{D.17})$$

and arrives at  $r_{\text{cell}} = r_*$  at  $\eta = 0$ . Then we multiply the continuity equation by  $r^2$  and integrate from 0 to  $r_{\text{cell}}(\eta)$ . This gives

$$\dot{\mu}_{\text{cell}} = r_{\text{cell}}^2 \Upsilon_{\delta, IJ}(\eta, r_{\text{cell}}), \quad (\text{D.18})$$

where

$$\mu_{\text{cell}}(\eta) \equiv \int_0^{r_{\text{cell}}(\eta)} r^2 dr (1 + \delta_0(\eta, r)) \quad (\text{D.19})$$

is the mass inside the cell. We see that it is no longer constant due to perturbations. Finally, from the Euler equation we obtain the equation of motion for the cell boundary, similar to (D.8), but now with a non-zero r.h.s.,

$$\ddot{r}_{\text{cell}} + \frac{\dot{r}_{\text{cell}}}{2} - \frac{r_{\text{cell}}}{2} + \frac{3\mu_{\text{cell}}}{2r_{\text{cell}}^2} = -\Upsilon_{\Theta, IJ}(\eta, r_{\text{cell}}). \quad (\text{D.20})$$

The last step is to decompose the cell radius and the mass back into the background values and perturbations,

$$r_{\text{cell}} = \hat{r} + r_{IJ}^{(2)} , \quad (\text{D.21a})$$

$$\mu_{\text{cell}} = \hat{\mu} + A(\eta)r_{IJ}^{(2)} + \mu_{IJ}^{(2)} , \quad (\text{D.21b})$$

where  $A(\eta)$  is defined as

$$A(\eta) = \hat{r}^2(\eta) [1 + \hat{\delta}(\eta, \hat{r}(\eta))] , \quad (\text{D.22})$$

and

$$\mu_{IJ}^{(2)}(\eta) \equiv \int_0^{\hat{r}(\eta)} r^2 dr \delta_0^{(2)}(\eta, r; k_I, k_J) . \quad (\text{D.23})$$

Linearizing Eqs. (D.18), (D.20) with respect to  $\mu_{IJ}^{(2)}$ ,  $r_{IJ}^{(2)}$  and using that  $\hat{\mu}$ ,  $\hat{r}$  obey the background equations, we arrive at two linear equations,

$$\dot{\mu}^{(2)} + A(\eta) \dot{r}^{(2)} + \frac{dA}{d\eta} r^{(2)} = \hat{r}^2 \Upsilon_\delta(\eta, \hat{r}) \quad (\text{D.24a})$$

$$\ddot{r}^{(2)} + \frac{1}{2} \dot{r}^{(2)} + B(\eta) r^{(2)} + \frac{3}{2\hat{r}^2} \mu^{(2)} = -\Upsilon_\Theta(\eta, \hat{r}) , \quad (\text{D.24b})$$

where we have omitted the indices  $I, J$  to simplify notations and  $B(\eta)$  is defined as

$$B(\eta) = 1 + \frac{3}{2} \hat{\delta}(\eta, \hat{r}(\eta)) - \frac{R_*^3}{\hat{r}^3(\eta)} . \quad (\text{D.25})$$

Note that the the sources on the r.h.s. of Eqs. (D.24) are evaluated at the unperturbed cell boundary  $(\eta, \hat{r}(\eta))$ . The coefficient functions  $A(\eta)$  and  $B(\eta)$  depend only on the local value of the background density contrast on the same boundary.

The equations (D.24) must be solved with the final condition  $r_{IJ}^{(2)}(0) = 0$  and the initial conditions

$$\mu_{IJ}^{(2)} \propto e^{2\eta} , \quad \dot{r}_{IJ}^{(2)} + \frac{d \ln A}{d\eta} r_{IJ}^{(2)} \propto e^{2\eta} , \quad \text{at } \eta \rightarrow -\infty . \quad (\text{D.26})$$

The first condition expresses the fact that the  $\mu_{IJ}^{(2)}$  is proportional to the second-order density contrast  $\delta_0^{(2)}$  by definition (D.23). The latter is required for the consistency of Eq. (D.24a).

#### D.4 Redefining sources for second-order perturbations

Here we show that the source  $\Upsilon_\delta$  in the perturbed continuity equation (D.24a) can be set to zero by a proper redefinition of the moving cell radius. This is consistent with the EFT of LSS where only the Euler equation is modified by the introduction of the effective stress tensor, whereas the continuity equations remains unchanged.

Let us redefine the cell radius by replacing

$$r_{IJ}^{(2)}(\eta) \mapsto r_{IJ}^{(2)}(\eta) + \epsilon_{IJ}(\eta) , \quad (\text{D.27})$$

where  $\epsilon_{IJ}(\eta)$  is chosen to obey the equation

$$A(\eta) \dot{\epsilon}_{IJ} + \frac{dA}{d\eta} \epsilon_{IJ} = \hat{r}^2 \Upsilon_{\delta, IJ}(\eta, \hat{r}) . \quad (\text{D.28})$$

Physically, this corresponds to choosing the moving cell boundary in such a way that the mass inside the cell — including background and perturbations — stays constant. As a result, the r.h.s. of Eq. (D.24a) vanishes,  $\tilde{\Upsilon}_\delta = 0$ .

Substituting (D.27), (D.28) into the Euler equation (D.24b) we obtain,

$$\ddot{r}_{IJ}^{(2)} + \frac{1}{2} \dot{r}_{IJ}^{(2)} + B(\eta) r_{IJ}^{(2)} + \frac{3}{2\hat{r}^2} \mu_{IJ}^{(2)} + B_1(\eta) \epsilon_{IJ} = -\tilde{\Upsilon}_{\Theta, IJ}(\eta, \hat{r}) , \quad (\text{D.29})$$

where

$$B_1 = \left( \frac{d \ln A}{d\eta} \right)^2 - \frac{d^2 \ln A}{d\eta^2} - \frac{1}{2} \frac{d \ln A}{d\eta} + B , \quad (\text{D.30a})$$

$$\tilde{\Upsilon}_\Theta = \Upsilon_\Theta + \left( \frac{1}{2} - \frac{d \ln A}{d\eta} \right) \frac{\Upsilon_\delta}{1 + \hat{\delta}} + \frac{d}{d\eta} \left( \frac{\Upsilon_\delta}{1 + \hat{\delta}} \right) . \quad (\text{D.30b})$$

Note that in the latter expression the background density  $\hat{\delta}$  is evaluated at the unperturbed cell boundary  $(\eta, \hat{r}(\eta))$ . Let us show the function  $B_1(\eta)$  vanishes on the background equations of motion. Recalling the definition (D.22) we have,

$$\frac{d \ln A}{d\eta} = \frac{2\dot{\hat{r}}}{\hat{r}} + \frac{\partial_\eta \hat{\delta} + \dot{\hat{r}} \partial_r \hat{\delta}}{1 + \hat{\delta}} \Big|_{\eta, \hat{r}} = \partial_r^2 \hat{\Psi}(\eta, \hat{r}) , \quad (\text{D.31})$$

where in the second equality we have used Eqs. (D.4), (D.3a), (D.3c). Similarly, from Eqs. (D.8), (D.3b), (D.3c) we find,

$$\frac{d^2 \ln A}{d\eta^2} = (\partial_r^2 \hat{\Psi})^2 - \frac{1}{2} \partial_r^2 \hat{\Psi} + 1 + \frac{3}{2} \hat{\delta} - \frac{R_*^3}{\hat{r}^3} \Big|_{\eta, \hat{r}} . \quad (\text{D.32})$$

Collecting these expressions along with the definition (D.25) indeed yields  $B_1(\eta) = 0$ . Thus, the Euler equation takes the form (D.24b) with the new source  $\tilde{\Upsilon}_\Theta$  given by Eq. (D.30b).

Let us now simplify  $\tilde{\Upsilon}_\Theta$ . Using the equations obeyed by the first order perturbations and the background, we can get rid of explicit time derivatives in  $\tilde{\Upsilon}_\Theta$ . Starting from  $\Upsilon_\delta$  defined in Eq. (D.16a) and using Eqs. (D.10), we have

$$\begin{aligned} \frac{d}{d\eta} \left( \frac{\Upsilon_\delta}{1 + \hat{\delta}} \right) = \frac{1}{4\pi(1 + \hat{\delta})} & \left[ (\partial_\eta \delta_\ell^{(1)} - \partial_r \hat{\Psi} \partial_r \delta_\ell^{(1)}) \partial_r \Psi_\ell^{(1)} + \delta_\ell^{(1)} (\partial_\eta \partial_r \Psi_\ell^{(1)} - \partial_r \hat{\Psi} \partial_r^2 \Psi_\ell^{(1)}) \right. \\ & \left. - \frac{\partial_\eta \hat{\delta} - \partial_r \hat{\Psi} \partial_r \hat{\delta}}{1 + \hat{\delta}} \delta_\ell^{(1)} \partial_r \Psi_\ell^{(1)} \right] , \end{aligned}$$

where we have suppressed the indices  $I, J$  to avoid clutter of notations. We now use Eqs. (D.10a), (D.3a) to simplify,

$$\frac{d}{d\eta} \left( \frac{\Upsilon_\delta}{1 + \hat{\delta}} \right) = \frac{1}{4\pi} \left[ \Theta_\ell^{(1)} \partial_r \Psi_\ell^{(1)} + \frac{\partial_r \hat{\delta}}{1 + \hat{\delta}} (\partial_r \Psi_\ell^{(1)})^2 + \delta_\ell^{(1)} (\partial_\eta \partial_r \Psi_\ell^{(1)} - \partial_r \hat{\Psi} \partial_r^2 \Psi_\ell^{(1)}) \right].$$

Finally, the radial part of the linearized Eq. (D.1b) before elimination of the Newton potential reads,

$$-\partial_\eta \partial_r \Psi_\ell^{(1)} - \frac{\partial_r \Psi_\ell^{(1)}}{2} + \partial_r \hat{\Psi} \partial_r^2 \Psi_\ell^{(1)} + \partial_r^2 \hat{\Psi} \partial_r \Psi_\ell^{(1)} + \frac{\partial_r \Phi_\ell^{(1)}}{\mathcal{H}^2} = 0. \quad (\text{D.33})$$

We collect these expressions into Eq. (D.30b) and eliminate  $\Theta_\ell^{(1)}, \delta_\ell^{(1)}$  using (D.10c) and the Poisson Eq. (D.1c). It is convenient to cast the result into the following suggestive form,

$$\tilde{\Upsilon}_{\Theta, IJ}(\eta) = \frac{1}{\mathcal{H}^2(1 + \hat{\delta})} \left[ \partial_r \tau_{\parallel, IJ} + \frac{2}{r} \tau_{\parallel, IJ} - \frac{2}{r} \tau_{\perp, IJ} \right] \Big|_{\eta, \hat{r}(\eta)}, \quad (\text{D.34})$$

where

$$\tau_{\parallel, IJ} = \frac{\mathcal{H}^2}{4\pi} (1 + \hat{\delta}) \partial_r \Psi_{\ell, I}^{(1)} \partial_r \Psi_{\ell, J}^{(1)} + \frac{1}{12\pi \mathcal{H}^2} \left[ \partial_r \Phi_{\ell, I}^{(1)} \partial_r \Phi_{\ell, J}^{(1)} - \frac{\ell(\ell + 1)}{r^2} \Phi_{\ell, I}^{(1)} \Phi_{\ell, J}^{(1)} \right], \quad (\text{D.35a})$$

$$\tau_{\perp, IJ} = \frac{\mathcal{H}^2 \ell(\ell + 1)}{8\pi r^2} (1 + \hat{\delta}) \Psi_{\ell, I}^{(1)} \Psi_{\ell, J}^{(1)} - \frac{1}{12\pi \mathcal{H}^2} \partial_r \Phi_{\ell, I}^{(1)} \partial_r \Phi_{\ell, J}^{(1)}. \quad (\text{D.35b})$$

In Sec. 4.3 we interpret  $\tau_{\parallel, \perp}$  as the components of the effective stress produced by the short modes.

## E WKB expansion for UV modes

### E.1 Equations and sources

The initial conditions (D.12) for linear aspherical perturbations are provided by the spherical Bessel functions which are exponentially suppressed at  $kr < (\ell + 1/2)$  for high multipoles  $\ell \gg 1$ . This implies that the perturbations with  $kr_* \ll \ell$  do not contribute into the variation of the density inside the cell and the corresponding elements of the response matrix are suppressed,  $Q_\ell(k, k') \approx 0$  for  $k$  or  $k'$  much smaller than  $\ell/r_*$ . The dominant contribution into the response matrix then comes from the modes with

$$k \gtrsim \ell/r_* \gg 1/r_*. \quad (\text{E.1})$$

These modes oscillate much faster than the background solution, so one can apply the WKB approximation to find their evolution.

Using the momentum as a large parameter, we write the leading WKB expressions,

$$\delta_\ell^{(1)} = (\ell + 1/2)^{-1} \delta_\ell e^{ikS_\ell - i\pi/4} + \text{h.c.} , \quad (\text{E.2a})$$

$$\Theta_\ell^{(1)} = (\ell + 1/2)^{-1} \vartheta_\ell e^{ikS_\ell - i\pi/4} + \text{h.c.} , \quad (\text{E.2b})$$

$$\Psi_\ell^{(1)} = (\ell + 1/2)^{-1} k^{-2} \psi_\ell e^{ikS_\ell - i\pi/4} + \text{h.c.} , \quad (\text{E.2c})$$

$$\Phi_\ell^{(1)} = \frac{3}{2} \mathcal{H}^2 (\ell + 1/2)^{-1} k^{-2} \varphi_\ell e^{ikS_\ell - i\pi/4} + \text{h.c.} \quad (\text{E.2d})$$

where  $\delta_\ell, \vartheta_\ell$  etc. are slowly varying functions. Note that  $\Psi_\ell^{(1)}$  and  $\Phi_\ell^{(1)}$  are suppressed by two powers of  $k$  compared to  $\delta_\ell^{(1)}$  and  $\Theta_\ell^{(1)}$ . For convenience, we have also inserted the overall factors  $(\ell+1/2)^{-1}$ , as well as complex phases in front of various functions.<sup>19</sup> Then the initial conditions at  $\eta \rightarrow -\infty$ , set up by the asymptotic expansion of spherical Bessel functions at large order [71], are real and depend only on the ratio  $\varkappa$  defined in Eq. (2.24),

$$S_\ell = \frac{1}{\varkappa} \left[ \sqrt{(\varkappa r)^2 - 1} - \arccos \frac{1}{\varkappa r} \right] , \quad (\text{E.3a})$$

$$\delta_\ell = \vartheta_\ell = -\psi_\ell = -\varphi_\ell = \frac{2\pi}{\sqrt{\varkappa r} [(\varkappa r)^2 - 1]^{1/4}} \cdot e^\eta . \quad (\text{E.3b})$$

These expressions apply at  $r > 1/\varkappa$ . At smaller radii the Bessel functions are exponentially suppressed, so we set all coefficients in the WKB expansion to zero.

From the equation (D.10c) for velocity potential we obtain

$$\psi_\ell = -\frac{\vartheta_\ell}{(S'_\ell)^2 + (\varkappa r)^{-2}} , \quad (\text{E.4a})$$

where we have denoted with prime the radial derivative  $\partial_r$ . Similarly, for the gravitational potential we have,

$$\varphi_\ell = -\frac{\delta_\ell}{(S'_\ell)^2 + (\varkappa r)^{-2}} . \quad (\text{E.4b})$$

Further, we substitute the form (E.2) into Eqs. (D.10a), (D.10b). At the leading order  $O(k)$  both equations reduce to

$$\left. \frac{dS_\ell}{d\eta} \right|_{\text{flow}} = 0 . \quad (\text{E.5})$$

where we have used the derivative along the background flow lines,

$$\left. \frac{d}{d\eta} \right|_{\text{flow}} = \frac{\partial}{\partial \eta} - \hat{\Psi}' \frac{\partial}{\partial r} . \quad (\text{E.6})$$

---

<sup>19</sup>Note that these normalization conventions differ from Ref. [71].

We conclude that  $S_\ell$  is conserved along the flow and we can write at all times,

$$S_\ell = \frac{1}{\varkappa} \left[ \sqrt{(\varkappa R)^2 - 1} - \arccos \frac{1}{\varkappa R} \right] \iff \frac{\partial S_\ell}{\partial R} = \frac{\sqrt{(\varkappa R)^2 - 1}}{\varkappa R}, \quad (\text{E.7})$$

where  $R$  is the Lagrangian radial coordinate labeling the background flow lines.

From the order  $O(1)$  of Eqs. (D.10a), (D.10b) we obtain the equations for the first-order WKB coefficients

$$\left. \frac{d\delta_\ell}{d\eta} \right|_{\text{flow}} - \hat{\Theta}\delta_\ell - (1 + \hat{\delta})\vartheta_\ell = 0, \quad (\text{E.8a})$$

$$\left. \frac{d\vartheta_\ell}{d\eta} \right|_{\text{flow}} - \frac{3}{2}\delta_\ell + \left[ \frac{1}{2} - \frac{2(\varkappa r S'_\ell)^2 \hat{\Psi}''}{1 + (\varkappa r S'_\ell)^2} - \frac{2\hat{\Psi}'}{r(1 + (\varkappa r S'_\ell)^2)} \right] \vartheta_\ell = 0. \quad (\text{E.8b})$$

We notice that Eqs. (E.8) do not contain spatial derivatives of the functions  $\delta_\ell$ ,  $\vartheta_\ell$ , so they form a system of ordinary differential equations for these functions along the background flow lines. We solve these equations numerically in the vicinity of the flow line corresponding to the moving cell boundary  $\hat{r}(\eta)$ , which in the Lagrangian coordinates is fixed at  $R = R_*$ . This is sufficient for evaluating the sources (D.34).

Let us obtain the explicit expressions for the stress tensor components  $\tau_{\parallel, \perp}$  (D.35) in the WKB limit. Considering only the diagonal components with  $k_I = k_J = k$ , the aggregated contribution of the UV modes into the effective stress tensor reads

$$\begin{aligned} & \sum (2\ell + 1) \int [dk] P(k) \tau_\alpha(\eta, R; \ell, k) \\ &= 2\mathcal{H}^2 \int_{k \gg R_*^{-1}} \frac{dk P(k)}{(2\pi)^3} \cdot \int_{R^{-1}}^{\infty} \frac{d\varkappa}{\varkappa} \sum_{a=\text{kin, pot}} \chi_\alpha^a(\eta, R; \varkappa), \quad \alpha = \parallel, \perp, \end{aligned} \quad (\text{E.9})$$

where we have defined new kinetic and potential WKB sources  $\chi_\alpha^a$ ,  $a = \text{kin, pot}$ . Take, for example, the kinetic part of  $\tau_{\parallel}$  given by the first term in Eq. (D.35a). Using Eq. (E.2c), it takes the form

$$\tau_{\parallel}^{\text{kin}} = \frac{\mathcal{H}^2(1 + \hat{\delta})}{2\pi(\ell + 1/2)^2 k^2} (S'_\ell)^2 \psi_\ell^2 (1 - \cos(2ikS_\ell - i\pi/4)). \quad (\text{E.10})$$

The second term in brackets quickly oscillates as function of  $k$  and averages away in the cumulative quantities involving integrals over  $k$ . Neglecting it, we arrive at the expression for the rescaled component of the stress,

$$\chi_{\parallel}^{\text{kin}} = \frac{1 + \hat{\delta}}{2\pi} (S'_\ell)^2 \psi_\ell^2. \quad (\text{E.11a})$$

Similar calculation for other components yields,

$$\chi_{\perp}^{\text{kin}} = \frac{1 + \hat{\delta}}{4\pi} \frac{\psi_{\ell}^2}{(\varkappa r)^2}, \quad (\text{E.11b})$$

$$\chi_{\parallel}^{\text{pot}} = \frac{3}{8\pi} \left( (S'_{\ell})^2 - \frac{1}{(\varkappa r)^2} \right) \varphi_{\ell}^2, \quad (\text{E.11c})$$

$$\chi_{\perp}^{\text{pot}} = -\frac{3}{8\pi} (S'_{\ell})^2 \varphi_{\ell}^2. \quad (\text{E.11d})$$

Note that according to the initial conditions (E.3), the WKB functions entering here vanish at early times if  $\varkappa r < 1$ . Since the WKB evolution is ultralocal along the flow, we conclude that this property is preserved in terms of the Lagrangian radius  $R$ . Namely, the stress tensor components (E.11) are non-vanishing only if  $\varkappa > 1/R$ , which implies the lower limit of the  $\varkappa$ -integration in Eq. (E.9).

Finally, we can collect the stress tensor components into the rescaled sources (4.40) used in the counterterm model,

$$v^{\text{kin}} = \frac{1}{2\pi} \left[ 2(S'_{\ell})^2 \psi_{\ell} \psi'_{\ell} + \left( 2S'_{\ell} S''_{\ell} + \frac{2(S'_{\ell})^2}{r} - \frac{1}{\varkappa^2 r^3} + \frac{\hat{\delta}'}{1 + \hat{\delta}} (S'_{\ell})^2 \right) \psi_{\ell}^2 \right] \Big|_{\eta, \hat{r}}, \quad (\text{E.12a})$$

$$v^{\text{pot}} = \frac{3}{4\pi(1 + \hat{\delta})} \left[ \left( (S'_{\ell})^2 - \frac{1}{(\varkappa r)^2} \right) \varphi_{\ell} \varphi'_{\ell} + \left( S'_{\ell} S''_{\ell} + \frac{2(S'_{\ell})^2}{r} \right) \varphi_{\ell}^2 \right] \Big|_{\eta, \hat{r}}, \quad (\text{E.12b})$$

## E.2 Evaluation of the $\varkappa$ -integrals

The WKB expressions for the effective stress  $\chi_{\alpha}^a$  are singular at  $\varkappa R \rightarrow 1$ . This singularity stems from the initial conditions (E.3b) and, since the dynamical equations (E.8) are ultralocal, propagates to arbitrary time. It is spurious and arises from the breakdown of the WKB approximation at the ‘‘turning point’’  $\varkappa R = 1$ . Indeed, the standard condition for the validity of the WKB expansion is the smallness of the second derivative of the phase,

$$S''_{\ell} / (S'_{\ell})^2 \ll k. \quad (\text{E.13})$$

Substituting here the result (E.7) and using that  $\partial_r R$  is an order-one quantity, we conclude that the WKB approximation requires

$$|\varkappa R - 1| \gg (\ell + 1/2)^{-2/3}. \quad (\text{E.14})$$

Strictly speaking, we can use the WKB expressions only at  $\varkappa > (1 + \epsilon)R^{-1}$ , where  $\epsilon \gg \ell^{-2/3}$ .

However, when computing the contribution of the high- $\ell$  modes into the fluid prefactor and the counterterm we need to integrate over all  $\varkappa$  for which the sources are non-zero. We can try to naively extend the WKB expressions in the integrals down to  $\epsilon = 0$  hoping that the error we make in this way is small. This indeed works

for the integrals of the type appearing in the counterterm stress tensor (4.38) since the singularity in  $\chi_\alpha^a$  has the form  $(\varkappa R - 1)^{-1/2}$  and is integrable. So, in principle, one can first compute  $\tau_\alpha^{a,\text{ctr}}$  along several flow lines and obtain the counterterm stress as function of  $\eta$  and  $r$  in the vicinity of the cell boundary. Then the radial derivative entering the counterterm sources (4.30) can also be evaluated numerically. This method is, however, inefficient since it requires numerical evaluation of the  $\varkappa$ -integral at several points in  $R$  and at every time slice. Instead, we use the expression (4.39) for the counterterm sources and notice that we can split it into contributions of different  $\varkappa$ , solve Eqs. (4.29) for each  $\varkappa$  separately, and take the  $\varkappa$ -integral only once in the end. The same approach is used to calculate the high- $\ell$  fluid prefactor (2.25).

However, here we encounter a problem since the integrand contains a singularity  $(\varkappa R_* - 1)^{-3/2}$  and a naive  $\varkappa$ -integration diverges. This singularity can be traced to the same singularity in  $v^{\text{pot}}(\eta; \varkappa)$  which, in turn, comes from the derivative  $\partial_r \chi_{\parallel}^{\text{pot}}(\eta, R; \varkappa)$ .<sup>20</sup> The divergence is spurious and arises because of interchanging the order of  $r$ -differentiation and  $\varkappa$ -integration. To resolve it, we have to treat this step more carefully.

In order to make the discussion general, we consider an arbitrary function  $\chi(R; \varkappa)$ , such that

$$\chi(R; \varkappa) \simeq \frac{\chi_{\frac{1}{2}}}{(\varkappa R - 1)^{1/2}}, \quad \text{at } \varkappa R \rightarrow 1. \quad (\text{E.15})$$

We have suppressed a possible time dependence of  $\chi$  since it is irrelevant for the argument. Then we have a chain of relations,

$$\partial_r \int_{R^{-1}}^{\infty} \frac{d\varkappa}{\varkappa} \chi = \lim_{\epsilon \rightarrow 0} \partial_r \int_{(1+\epsilon)R^{-1}}^{\infty} \frac{d\varkappa}{\varkappa} \chi = \lim_{\epsilon \rightarrow 0} \left[ \int_{(1+\epsilon)R^{-1}}^{\infty} \frac{d\varkappa}{\varkappa} \partial_r \chi - \frac{2}{\sqrt{\epsilon}} [\partial_r \chi]_{\frac{3}{2}} \right], \quad (\text{E.16})$$

where

$$[\partial_r \chi]_{\frac{3}{2}} = -\frac{\partial_r R}{2R} \chi_{\frac{1}{2}} = \lim_{\epsilon \rightarrow 0} [\epsilon^{3/2} \partial_r \chi(R; (1+\epsilon)R^{-1})] \quad (\text{E.17})$$

is the coefficient of the  $(\varkappa R - 1)^{-3/2}$  singularity in  $\partial_r \chi$ . Thus, we see that a proper treatment of the  $\varkappa$ -integral consists in regulating it at the lower end, substituting a divergent boundary term and restoring the lower limit afterwards. We denote the integrals understood in the sense of this regularization procedure with a dash-integral sign.

In practice, both terms in (E.16) are evaluated numerically at small, but finite  $\epsilon$ . The difference between the straightforward application of this formula and the exact result is then  $O(\sqrt{\epsilon})$  which can be significant. The same is true even for convergent integrals, like those of  $v^{\text{kin}}$  or  $\chi_{\parallel}^a$  appearing in (E.9). To improve precision, we evaluate this  $O(\sqrt{\epsilon})$  correction computing the Taylor expansion of the functions  $v^a$  and  $\chi_\alpha^a$  at  $\varkappa \rightarrow R_*^{-1}$ .

---

<sup>20</sup>It is easy to see that  $v^{\text{kin}}$  does not lead to any troubles since the strongest singularity in it is  $(\varkappa R_* - 1)^{-1/2}$ .

We start by introducing dimensionless variables<sup>21</sup>

$$x = \varkappa R_* - 1, \quad y = R/R_* - 1, \quad (\text{E.18})$$

and write

$$v(x) = v_{\frac{3}{2}} x^{-3/2} + v_{\frac{1}{2}} x^{-1/2} + O(\sqrt{x}), \quad (\text{E.19})$$

where  $v$  stands for any of the functions  $v^a$  or  $\chi_\alpha^a|_{y=0}$ . Note that for all of them, except  $v^{\text{pot}}$ , the first term in this expansion will be zero. The integral takes the form,<sup>22</sup>

$$\int_{R_*^{-1}}^{\infty} \frac{d\varkappa}{\varkappa} v = -\frac{2v_{\frac{3}{2}}}{\sqrt{\epsilon}} + 2(v_{\frac{1}{2}} - v_{\frac{3}{2}})\sqrt{\epsilon} + \int_{\epsilon}^{\infty} \frac{dx}{1+x} v(x) + O(\epsilon^{3/2}). \quad (\text{E.20})$$

To evaluate the counterterm prefactor, we choose a grid  $x_I$ , solve the system (4.29) separately with the sources given by  $v(x_I)$ ,  $v_{\frac{3}{2}}$ ,  $v_{\frac{1}{2}}$ , and combine the results at the final time slice using Eq. (E.20).

We still need to find the coefficients  $v_{\frac{3}{2}}$ ,  $v_{\frac{1}{2}}$ . We make use of the ultralocality of the WKB equations (E.8) which implies that in a small vicinity of the cell boundary defined by  $y \ll x \ll 1$  their solution has the form,

$$\delta_\ell(\eta, y; x) = (\alpha_0(\eta) + \alpha_1(\eta)x + \alpha_2(\eta)y + O(x^2, xy)) \delta_\ell^{\text{sing}}(y; x), \quad (\text{E.21a})$$

$$\vartheta_\ell(\eta, y; x) = (\beta_0(\eta) + \beta_1(\eta)x + \beta_2(\eta)y + O(x^2, xy)) \delta_\ell^{\text{sing}}(y; x). \quad (\text{E.21b})$$

Here

$$\delta_\ell^{\text{sing}}(y; x) \equiv \frac{2\pi}{\sqrt{\varkappa R} [(\varkappa R)^2 - 1]^{1/4}} \approx \frac{2\pi}{(2x)^{1/4}} \left[ 1 - \frac{5}{8}x - y \left( \frac{1}{4x} + \frac{23}{32} \right) \right] \quad (\text{E.22})$$

encapsulates the singular initial data, whereas the regular evolution kernels  $\alpha_0(\eta)$ ,  $\alpha_1(\eta)$ , etc. can be found by integrating (E.8) at  $|x|, |y| \ll 1$  with  $x$ - and  $y$ -independent initial conditions  $\delta_\ell = \vartheta_\ell = e^\eta$  at  $\eta \rightarrow -\infty$ . Further, we have

$$S'_\ell|_{y=0} = \left. \frac{\partial R}{\partial r} \right|_{\hat{r}} \cdot \sqrt{2x} + O(x^{3/2}), \quad S''_\ell|_{y=0} = \frac{1}{R_*} \left( \left. \frac{\partial R}{\partial r} \right|_{\hat{r}} \right)^2 \cdot \frac{1}{\sqrt{2x}} + O(x^{1/2}). \quad (\text{E.23})$$

Using these relations and Eqs. (E.4a), (E.4b) we find

$$\varphi_\ell|_{y=0} = -\frac{2\pi\hat{r}^2}{R_*^2} \cdot \frac{1}{(2x)^{1/4}} \left[ \alpha_0 + x \left( \frac{11\alpha_0}{8} - 2\alpha_0 \left( \left. \frac{\partial \ln R}{\partial \ln r} \right|_{\hat{r}} \right)^2 + \alpha_1 \right) \right], \quad (\text{E.24a})$$

$$\begin{aligned} \varphi'_\ell|_{y=0} = & \frac{2\pi\hat{r}^2}{R_*^3} \left. \frac{\partial R}{\partial r} \right|_{\hat{r}} \cdot \frac{1}{(2x)^{5/4}} \left[ \frac{\alpha_0}{2} \right. \\ & \left. + x \left( \frac{39}{16}\alpha_0 + 3\alpha_0 \left( \left. \frac{\partial \ln R}{\partial \ln r} \right|_{\hat{r}} \right)^2 - 4\alpha_0 \left( \left. \frac{\partial \ln R}{\partial \ln r} \right|_{\hat{r}} \right)^{-1} + \frac{\alpha_1}{2} - 2\alpha_2 \right) \right], \end{aligned} \quad (\text{E.24b})$$

<sup>21</sup>These variable should not be confused with the use of notations  $x, y$  in other sections of the paper.

<sup>22</sup>This formula can be easily generalized to the case when  $v$  is multiplied by an arbitrary function regular at  $x = 0$ , see [71] for explicit expressions.

and similarly for  $\psi_\ell, \psi'_\ell|_{y=0}$  with the replacement  $\alpha_i \mapsto \beta_i$ ,  $i = 0, 1, 2$ . Finally, substitution into Eqs. (E.12) yields,

$$\chi_{\parallel, \frac{3}{2}}^{\text{kin}} = \chi_{\parallel, \frac{1}{2}}^{\text{kin}} = \chi_{\perp, \frac{3}{2}}^{\text{kin}} = \chi_{\parallel, \frac{3}{2}}^{\text{pot}} = \chi_{\perp, \frac{3}{2}}^{\text{pot}} = \chi_{\perp, \frac{1}{2}}^{\text{pot}} = v_{\frac{3}{2}}^{\text{kin}} = 0, \quad (\text{E.25a})$$

$$\chi_{\perp, \frac{1}{2}}^{\text{kin}} = \frac{\pi(1 + \hat{\delta})\hat{r}^2}{\sqrt{2}R_*^2}\beta_0^2, \quad (\text{E.25b})$$

$$\chi_{\parallel, \frac{1}{2}}^{\text{pot}} = -\frac{3\pi\hat{r}^2}{2\sqrt{2}R_*^2}\alpha_0^2, \quad (\text{E.25c})$$

$$v_{\frac{1}{2}}^{\text{kin}} = \frac{\sqrt{2}\pi\hat{r}}{R_*^2} \left[ \left( \frac{\partial \ln R}{\partial \ln r} \Big|_{\hat{r}} \right)^3 - 1 \right] \beta_0^2, \quad (\text{E.25d})$$

$$v_{\frac{3}{2}}^{\text{pot}} = \frac{3\pi\hat{r}^2}{4\sqrt{2}R_*^3(1 + \hat{\delta})} \frac{\partial R}{\partial r} \Big|_{\hat{r}} \alpha_0^2, \quad (\text{E.25e})$$

$$v_{\frac{1}{2}}^{\text{pot}} = \frac{3\pi\hat{r}^2}{\sqrt{2}R_*^3(1 + \hat{\delta})} \frac{\partial R}{\partial r} \Big|_{\hat{r}} \left[ \alpha_0^2 \left( \frac{17}{16} + \frac{3}{2} \left( \frac{\partial \ln R}{\partial \ln r} \Big|_{\hat{r}} \right)^2 - 2 \left( \frac{\partial \ln R}{\partial \ln r} \Big|_{\hat{r}} \right)^{-1} \right) + \frac{\alpha_0\alpha_1}{2} - \alpha_0\alpha_2 \right]. \quad (\text{E.25f})$$

## F Alternative estimates of shell-crossing scale

Here we explore two alternative definitions of the shell-crossing scale, in addition to that presented in Sec. 4.2. We start with the linear perturbation matrix (4.21). Combining Eqs. (4.18) and (4.19) we get an equation for its general element,

$$\frac{d\varpi_i^j}{d\eta} = \partial_i \partial_j \partial_k \hat{\Psi} x_k^{(1)} + \partial_j \partial_k \hat{\Psi} \varpi_i^k - \partial_i \partial_k \hat{\Psi} \varpi_j^k + \partial_i \partial_j \Psi^{(1)}, \quad (\text{F.1})$$

where all quantities are evaluated on the unperturbed trajectory  $(\eta, \hat{\mathbf{x}})$ . The variance of  $\varpi_i^j$  is dominated by short modes implying that the derivatives acting on perturbations are enhanced compared to derivatives acting on the background. This allows us to neglect the first term on the r.h.s. of (F.1). Further, by symmetrizing the equation in the indices  $i$  and  $j$  we get rid of the second and third terms. In particular, the trace over  $i$  and  $j$  gives Eq. (4.22) from the main text.

Since the background solution is spherically symmetric, it is natural to split  $\mathbf{x}^{(1)}$  into the radial (parallel) and transverse (perpendicular) parts. For the radial part we have

$$\frac{d\varpi_{\parallel}}{d\eta} \equiv -\frac{d}{d\eta} \partial_r r^{(1)} = \partial_r^2 \Psi^{(1)}. \quad (\text{F.2})$$

Computing its variance with the help of the WKB expressions from appendix E.1 we obtain,

$$\left\langle (\varpi_{\parallel})^2 \right\rangle_{k_{\max}} \approx \frac{1}{5} \cdot 4\pi \int^{k_{\max}} [dk] P(k) \cdot (D_{\parallel}(\eta, R))^2, \quad (\text{F.3})$$

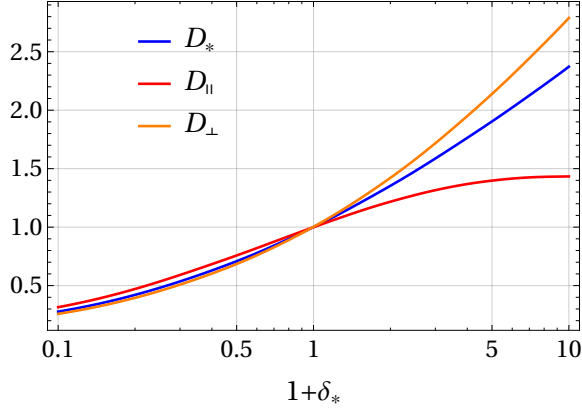


**Figure 19.** The radial and transverse growth factors, evaluated at the cell boundary, as functions of  $\delta_*$  at  $\eta = 0$ , together with the cumulative growth factor (4.26).

where

$$D_{||}(\eta, R) = \left( 5 \int_{1/R}^{\infty} \frac{d\boldsymbol{\varkappa}}{(2\pi)^2 \boldsymbol{\varkappa}} \left| \int_{-\infty}^{\eta} d\eta' (\partial_r S_\ell)^2 \Psi_\ell \Big|_{\eta', R; \boldsymbol{\varkappa}} \right|^2 \right)^{1/2} \quad (\text{F.4})$$

is the radial growth factor, which we normalized to coincide with  $e^\eta$  at  $\delta_* = 0$ . Similarly, for the transverse part:

$$\frac{d\varpi_\perp}{d\eta} \equiv -\frac{d}{d\eta} \partial_\mu x_\mu^{(1)} = \frac{\Delta_\Omega \Psi^{(1)}}{r^2}, \quad (\text{F.5})$$

where  $\mu = \theta, \phi$  are angular directions, and  $\Delta_\Omega$  stands for the angular part of the Laplacian. The variance reads,

$$\left\langle (\varpi_\perp)^2 \right\rangle_{k_{\max}} \approx \frac{8}{15} \cdot 4\pi \int^{k_{\max}} [dk] P(k) \cdot (D_\perp(\eta, R))^2 \quad (\text{F.6})$$

with the transverse growth factor

$$D_\perp(\eta, R) = \left( \frac{15}{8} \int_{1/R}^{\infty} \frac{d\boldsymbol{\varkappa}}{(2\pi)^2 \boldsymbol{\varkappa}^5} \left| \int_{-\infty}^{\eta} d\eta' \frac{\Psi_\ell(\eta', R; \boldsymbol{\varkappa})}{r^2(\eta', R)} \right|^2 \right)^{1/2}. \quad (\text{F.7})$$

The two new growth factors, evaluated at the cell boundary, are compared with  $D_*(\eta)$  in Fig. 19. We see that they follow the same qualitative trend: They are larger than 1 for overdensities and decrease below 1 in the underdense regions. The difference between different growth factors is more significant at  $\delta_* > 0$  with the hierarchy

$$D_{||}(\eta, R_*) < D_*(\eta) < D_\perp(\eta, R_*) \quad \text{for } \delta_* > 0. \quad (\text{F.8})$$

On the other hand, for underdensities all three growth factors almost coincide and the ordering is reversed.

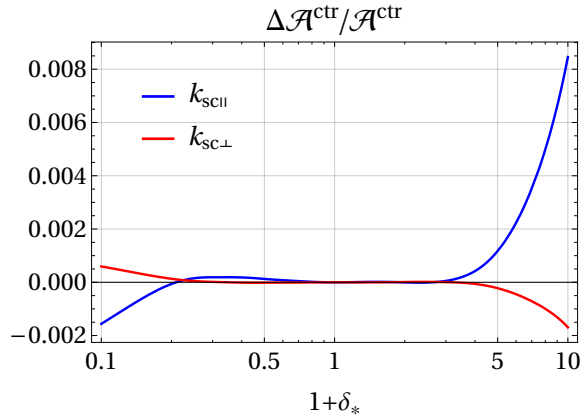


**Figure 20.** Difference between the counterterm prefactor computed with alternative estimates of the shell-crossing scale and the baseline model. The curves are obtained from fitting the same N-body data as in the main text. The cell radius is  $r_* = 10 \text{ Mpc}/h$  and redshift  $z = 0$ .

The new growth factors characterize shell-crossing in the radial and transverse directions, so we introduce

$$k_{\text{sc}\parallel} \propto D_{\parallel}^{-m/2}, \quad k_{\text{sc}\perp} \propto D_{\perp}^{-m/2}. \quad (\text{F.9})$$

We consider these estimates as two extremes bracketing reasonable dependences of  $k_{\text{sc}}$  on the background and reflecting the theoretical uncertainty of the counterterm. To assess this uncertainty, we fit the counterterm models with  $D_*$  replaced by  $D_{\parallel}$  and  $D_{\perp}$  to the N-body data following the procedure described in Sec. 5. The difference between the resulting counterterms prefactors and the prefactor obtained with the baseline model is plotted in Fig. 20 for the cell radius  $r_* = 10 \text{ Mpc}/h$  and redshift  $z = 0$ . We observe that the difference is very small and stays within 1% even at the tails. The picture for other cell radii and redshifts is similar.

## G Sensitivity of the “speed of sound” to cosmology

In Sec. 5 we have measured the values of the EFT parameters in the power spectrum from the Farpoint simulation, Eq. (5.2). They differ by some  $\sim 30\%$  from the values previously reported in the literature. While the error bars of our measurement are quite large and encompass within  $2\sigma$  the previous values, it is worth understanding the origin of this discrepancy. We are going to argue that it can be attributed to the difference between the Planck cosmological parameters used in the Farpoint simulation and the WMAP-based cosmologies used for previous measurements. For comparison we take the cosmological parameters (cf. (5.1)),

$$\Omega_m = 0.26, \quad \Omega_b = 0.044, \quad h = 0.72, \quad n_s = 0.96, \quad \sigma_8 = 0.794. \quad (\text{G.1})$$

These are the input parameters for the Horizon Run 2 (HR2) simulation [97] which was used in [71] to measure the speed of sound

$$\gamma_0^{\text{HR2}} = (1.51 \pm 0.07)(\text{Mpc}/h)^2 . \quad (\text{G.2})$$

Previous estimates [5, 79] for similar cosmology gave the value  $m \approx 8/3$  for the exponent of the power-law scaling of  $\gamma(z)$ .

We start by observing that the speed of sound enters into the template for the nonlinear power spectrum as part of the renormalized one-loop contribution,

$$P_{\text{NL}}(k)|_{z=0} = P(k) + P^{\text{SPT}, 1\text{-loop}}(k) - 2\gamma_0 k^2 P(k) , \quad (\text{G.3})$$

where  $P^{\text{SPT}, 1\text{-loop}}$  is the one-loop correction computed in the Standard Perturbation Theory (SPT) (i.e. without renormalization). Thus, we can get a rough idea of a possible shift of  $\gamma_0$  due to different cosmologies without reference to N-body data by looking at the change in the SPT one-loop contribution. More precisely, we want to compare the ratio

$$\frac{P^{\text{SPT}, 1\text{-loop}}(k)}{2k^2 P(k)} \quad (\text{G.4})$$

at  $k \in [0.1 \div 0.3] h/\text{Mpc}$  — the range of momenta typically used in the  $\gamma_0$  measurements.<sup>23</sup> In the left plot of Fig. 21 we show this ratio in the HR2 and Farpoint cosmologies. We emphasize that to calculate it we use only the linear power spectrum for the two cosmologies which we process with CLASS-PT [18] to evaluate one-loop. We see that, modulo the baryon acoustic oscillations (BAO), the ratio differs on average by  $\sim 0.5(\text{Mpc}/h)^2$ . This is of the same magnitude as the change in  $\gamma_0$  found from simulations.

An alternative estimate can be obtained by considering the UV-sensitive part of  $P^{\text{SPT}, 1\text{-loop}}$ . In this part  $\gamma_0$  is known to renormalize the so-called velocity dispersion,

$$\sigma_v^2 \equiv \frac{1}{6\pi^2} \int_{k_{\text{min}}}^{\infty} dk P(k) , \quad (\text{G.5})$$

entering into the full one-loop expression in the combination

$$\frac{61}{210} \sigma_v^2 + \gamma_0 . \quad (\text{G.6})$$

The integral in (G.5) runs from  $k_{\text{min}} \simeq 0.1 h/\text{Mpc}$  to infinity. One expects the change in the two terms in (G.6) to be comparable when the cosmological parameters are varied, which gives

$$\gamma_0|_{\text{Farpoint}} - \gamma_0|_{\text{HR2}} \sim \frac{61}{210} \left( \sigma_v^2|_{\text{Farpoint}} - \sigma_v^2|_{\text{HR2}} \right) = 0.22 . \quad (\text{G.7})$$

---

<sup>23</sup>Recall that we include theoretical uncertainty which makes the measurement of  $\gamma_0$  weakly sensitive to  $k$  above  $0.1 h/\text{Mpc}$ .

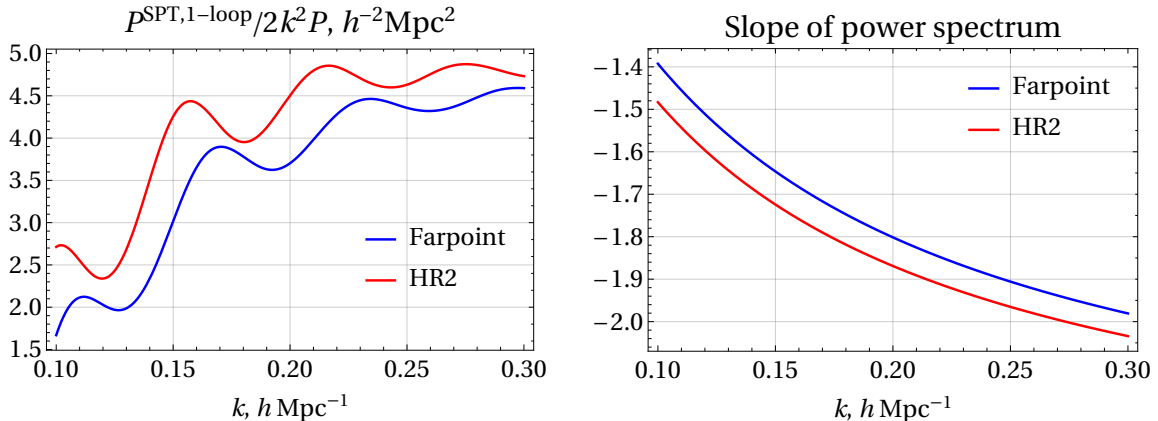


**Figure 21.** Ratio (G.4) (*left*) and the slope of the linear power spectrum (*right*) in cosmologies used in the Farpoint and Horizon Run 2 simulations. We find the slope from the broad-band part of the power spectrum approximated with the Eisenstein–Hu formula.

This is again in the ballpark of the  $\gamma_0$ -shift between cosmologies which we found from simulations.

The expected shift in  $m$  can be estimated similarly. From the scaling universe approximation we have

$$m \sim 4/(n + 3), \quad (\text{G.8})$$

where  $n$  is the slope of the linear power spectrum. In the right panel of Fig. 21 we show the slope  $d \ln[P(k)]/d \ln k$  in the two compared cosmologies. To obtain it, we removed the BAO by approximating the broad-band part of the linear power spectrum with the Eisenstein–Hu template [98]. We see that the slope in Farpoint cosmology is bigger, implying lower  $m$ . Substituting the slope evaluated at  $k = 0.1 h/\text{Mpc}$  one obtains

$$m|_{\text{Farpoint}} - m|_{\text{HR2}} \sim -0.17. \quad (\text{G.9})$$

This has the same sign, but somewhat smaller magnitude than the shift found from the simulations. Still, it again lies in the right ballpark. In this respect, it is worth observing that the slope of the linear power spectrum varies significantly over the relevant range of momenta, suggesting that the relation (G.8) should not be trusted literally. Rather than trying to connect  $m$  to the linear slope, it is more appropriate to think of it as an effective power-law resulting from non-linear dynamics involving different scales. The scaling universe intuition is still useful, but only qualitatively.

## H Transients from Zeldovich initial conditions

Zeldovich initial conditions (ZIC) are known to give rise to long-lived transients in the N-body simulations that bias their results [90, 91]. In this appendix we estimate this effect in the case of the PDF. We focus on the exponential part of the PDF since

it is expected to give the leading contribution. We work in the EdS approximation and follow the method of Ref. [99].

ZIC modify the map (2.10) between the spherically symmetric linear and non-linear density contrasts. To find this modification, let us reconsider the equations for spherical collapse. Motion of a spherical shell of matter is described by the energy conservation,

$$\frac{1}{2} \left( \frac{dy}{d\tau} \right)^2 - \frac{GM}{y} = \mathcal{E}, \quad (\text{H.1})$$

where  $y$  is the physical radius of the shell,  $\tau$  is the physical time,  $\mathcal{M}$  is the total mass inside the shell, and  $\mathcal{E}$  is the total shell's energy. We are going to see that underdense regions are stronger affected by ZIC, so we choose  $\mathcal{E} > 0$ . The solution to this equation is written in the parametric form,

$$y = \frac{GM}{2\mathcal{E}} (\text{ch } \theta - 1), \quad (\text{H.2a})$$

$$\tau = \frac{GM}{(2\mathcal{E})^{3/2}} (\text{sh } \theta - \theta - \text{sh } \theta_i + \theta_i) + \tau_i, \quad (\text{H.2b})$$

where  $\theta_i$  is the value of the parameter  $\theta$  at the initial time  $\tau_i$  corresponding to the start of the simulations. Both  $\theta_i$  and  $\tau_i$  vanish if the initial conditions are set in the exact growing mode. We are going to see that for ZIC they are non-zero.

Next we change the variables from  $(\tau, y)$  to the scale factor  $a$  and the comoving shell radius  $r = y/a$ . We use the relations,

$$a = \left( \frac{8\pi G}{3} \rho_i a_i^3 \right)^{1/3} \left( \frac{3}{2} \tau \right)^{2/3}, \quad (\text{H.3a})$$

$$\mathcal{M} = \frac{4\pi}{3} \rho_i a_i^3 R^3, \quad (\text{H.3b})$$

where in the last formula we expressed the mass inside the shell through its Lagrangian radius  $R$ ;  $\rho_i$  is the initial average density of the universe and  $a_i$  is the initial scale factor. This casts the parametric solution into the form,

$$r = R \left( \frac{2}{9} \right)^{1/3} \frac{\text{ch } \theta - 1}{[\text{sh } \theta - \theta - \text{sh } \theta_i + \theta_i + \mathcal{C}]^{2/3}}, \quad (\text{H.4a})$$

$$a = a_i \mathcal{C}^{-2/3} [\text{sh } \theta - \theta - \text{sh } \theta_i + \theta_i + \mathcal{C}]^{2/3}, \quad (\text{H.4b})$$

where we have introduced the notation

$$\mathcal{C} = \tau_i \frac{(2\mathcal{E})^{3/2}}{GM} = \frac{\sqrt{2}}{3} \left[ \frac{3\mathcal{E}}{2\pi G \rho_i a_i^2 R^2} \right]^{3/2}. \quad (\text{H.5})$$

By mass conservation, the non-linear density contrast inside the shell is

$$1 + \bar{\delta}(r, a) = \left( \frac{R}{r} \right)^3 = \frac{9 (\text{sh } \theta - \theta - \text{sh } \theta_i + \theta_i + \mathcal{C})^2}{2(\text{ch } \theta - 1)^3}. \quad (\text{H.6})$$

Our task now is to connect the integration constants  $\theta_i, \mathcal{C}$  to the linear density field.

We recall that in Zeldovich approximation the Eulerian ( $\mathbf{x}$ ) and Lagrangian ( $\mathbf{X}$ ) coordinates of a particle are related as

$$\mathbf{x} = \mathbf{X} - \nabla \Psi_L(\mathbf{X}), \quad (\text{H.7})$$

where  $\Psi_L$  is the linear velocity potential. From the identity  $\Delta \Psi_L = \Theta_L = \delta_L$  we find for the case of spherical symmetry

$$\partial_R \Psi_L = \frac{R}{3} \bar{\delta}_L(R, a), \quad (\text{H.8})$$

where  $\bar{\delta}_L(R, a)$  is the average *linear* density contrast inside  $R$  at the time set by  $a$ . Imposing the relation (H.7) at the initial moment of the simulation we find,

$$r_i = R \left( 1 - \frac{1}{3} \bar{\delta}_L(R, a_i) \right) \quad (\text{H.9a})$$

Imposing the Zeldovich approximation on the initial velocity yields,

$$\left. \frac{dr}{da} \right|_i = -\frac{R}{3} \frac{\bar{\delta}_L(R, a_i)}{a_i}. \quad (\text{H.9b})$$

Substituting Eqs. (H.4) into (H.9) we obtain,

$$\text{ch } \theta_i + 1 = 2 \left( 1 - \frac{a_i}{3a} \bar{\delta}_L \right) \left( 1 - \frac{2a_i}{3a} \bar{\delta}_L \right)^2, \quad (\text{H.10a})$$

$$\mathcal{C} = \frac{\sqrt{2}}{3} \left( -\frac{10a_i}{3a} \bar{\delta}_L \right)^{3/2} \left( 1 - \frac{8a_i}{15a} \bar{\delta}_L + \frac{4a_i^2}{45a^2} \bar{\delta}_L^2 \right)^{3/2} \left( 1 - \frac{a_i}{3a} \bar{\delta}_L \right)^{-3/2}, \quad (\text{H.10b})$$

where  $\bar{\delta}_L$  is the shortcut for  $\bar{\delta}_L(R, a)$  and we have used that linear density contrast scales linearly with the scale factor,  $\bar{\delta}_L(R, a_i) = a_i \bar{\delta}_L(R, a)/a$ . These equations allow us to determine  $\theta_i$  and  $\mathcal{C}$  once  $\bar{\delta}_L$  is given. Equation (H.4b) then expresses  $\theta$  as function of  $a$ ,

$$\text{sh } \theta - \theta = \text{sh } \theta_i - \theta_i - \mathcal{C} + \left( \frac{a}{a_i} \right)^{3/2} \mathcal{C}. \quad (\text{H.11})$$

Finally, Eq. (H.6) gives the non-linear density. In this way, we obtain the modified map,

$$\bar{\delta}(r, a) = f_{\text{ZIC}}(\bar{\delta}_L(R, a); a_i/a) \quad (\text{H.12a})$$

and its inverse

$$\bar{\delta}_L(R, a) = F_{\text{ZIC}}(\bar{\delta}(r, a); a_i/a). \quad (\text{H.12b})$$

The set of equations for overdensities is derived similarly and reads,

$$\cos \theta_i + 1 = 2 \left(1 - \frac{a_i \bar{\delta}_L}{3a}\right) \left(1 - \frac{2a_i \bar{\delta}_L}{3a}\right)^2, \quad (\text{H.13a})$$

$$\mathcal{C} = \frac{\sqrt{2}}{3} \left(\frac{10a_i \bar{\delta}_L}{3a}\right)^{3/2} \left(1 - \frac{8a_i \bar{\delta}_L}{15a} + \frac{4a_i^2 \bar{\delta}_L^2}{45a^2}\right)^{3/2} \left(1 - \frac{a_i \bar{\delta}_L}{3a}\right)^{-3/2}, \quad (\text{H.13b})$$

$$\theta - \sin \theta = \theta_i - \sin \theta_i - \mathcal{C} + \left(\frac{a}{a_i}\right)^{3/2} \mathcal{C}, \quad (\text{H.13c})$$

$$1 + \bar{\delta}(r, a) = \left(\frac{R}{r}\right)^3 = \frac{9(\theta - \sin \theta - \theta_i + \sin \theta_i + \mathcal{C})^2}{2(1 - \cos \theta)^3}. \quad (\text{H.13d})$$

Note that the maps (H.12) are redshift dependent. Note also that in the limit  $a_i \rightarrow 0$  corresponding to exactly adiabatic initial conditions we have

$$\theta_i = \mathcal{C} = 0, \quad \text{sh } \theta - \theta = \frac{1}{6} \left(-\frac{20}{3} \bar{\delta}_L\right)^{3/2} \quad \text{or} \quad \theta - \sin \theta = \frac{1}{6} \left(\frac{20}{3} \bar{\delta}_L\right)^{3/2} \quad (\text{H.14})$$

and we recover the usual redshift-independent EdS map (B.4), (B.5).

It is instructive to simplify the result assuming  $|a_i \bar{\delta}_L/a| \ll 1$ . This is satisfied for the Farpoint simulation in the considered range of densities. Focusing again on underdensities, one can show that the combination  $(-\text{sh } \theta_i + \theta_i + \mathcal{C})$  is at least of order  $\mathcal{O}(|a_i \bar{\delta}_L/a|^{5/2})$  and is negligible. The leading correction then comes from the shift of  $\mathcal{C}$ ,

$$\mathcal{C} = \frac{\sqrt{2}}{3} \left(-\frac{10a_i \bar{\delta}_L}{3a}\right)^{3/2} \left(1 - \frac{3a_i \bar{\delta}_L}{10a}\right), \quad (\text{H.15})$$

which substituted into (H.11) gives,

$$\bar{\delta}_L \left(1 - \frac{a_i \bar{\delta}_L}{5a}\right) = F(\bar{\delta}). \quad (\text{H.16})$$

Expressing  $\bar{\delta}_L$ , we find

$$F_{\text{ZIC}}(\bar{\delta}; a_i/a) = F(\bar{\delta}) \left(1 + \frac{a_i}{5a} F(\bar{\delta})\right). \quad (\text{H.17})$$

This final expression is also valid for overdensities. Note that the transients decay slowly — only as the first power of the inverse scale factor. Thus, they survive even at large hierarchy between  $a_i$  and  $a$ . Since the mapping function  $F$  enters into the PDF exponentially, even a per cent shift in it leads to large systematic bias of the PDF. All formulas derived above can be applied to  $\Lambda$ CDM cosmology upon replacing the scale factor  $a$  by the growth factor  $g(z)$ .

We evaluate the shift of the spherical collapse map for the Farpoint simulation [73] which starts from ZIC at  $z_i = 200$ . The result is shown in Fig. 22.<sup>24</sup> We see that

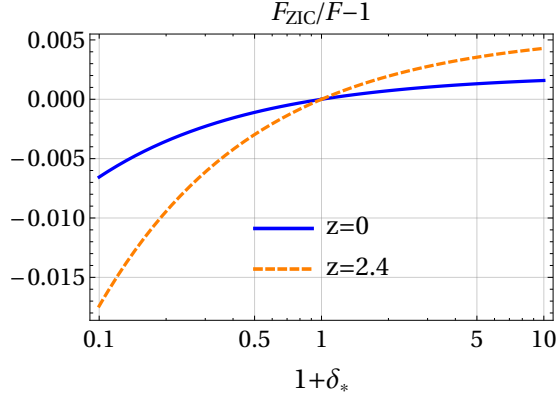


**Figure 22.** Relative shift of the mapping function of spherical collapse assuming Zeldovich initial conditions (ZIC) at  $z_i = 200$  with respect to the exact dynamics.

the relative shift is larger for underdensities and reaches 0.7% (1.7%) at  $1 + \delta_* = 0.1$  for  $z = 0$  ( $z = 2.4$ ).

We can now estimate the effect of transients on the PDF by taking the ratio of the exponential parts with ZIC and in the exact case,

$$\frac{\mathcal{P}_{\text{ZIC}}}{\mathcal{P}} \simeq \exp \left\{ -\frac{1}{2g^2(z)\sigma_{R_*}^2} [F_{\text{ZIC}}^2 - F^2] \right\} \approx \exp \left\{ -\frac{g_i}{5g^3(z)\sigma_{R_*}^2} F^3(\delta_*) \right\}. \quad (\text{H.18})$$

This factor is close to 1 in the central region of the PDF, but quickly deviates from unity at the tails. It is particularly strong for underdensities where the function  $F(\delta_*)$  is large in absolute value (see the left panel of Fig. 15). Also, as expected, the effect is larger for higher redshifts.

In Fig. 23 we compare the correction (H.18) to the residuals between the N-body PDF and the theoretical model constructed in the main text. The latter does not include the effect of transients and thus we expect a systematic difference between the model and the data. The residuals indeed appear to follow the trend implied by Eq. (H.18). However, for cells of radius  $r_* = 7.5 \text{ Mpc}/h$  (left panel) or larger this systematic error is buried under the statistical uncertainty, so we neglect it in our analysis. On the other hand, for  $r_* = 5 \text{ Mpc}/h$  (right panel) the effect of ZIC is statistically significant at strong underdensities. This is consistent with the findings of [46]. We use in the analysis only the part of the data for which the systematic bias (H.18) does not exceed the statistical error. This leads to the cuts  $(1 + \delta_*) > (1 + \delta_*)_{\text{min}}$ , where

$$(1 + \delta_*)_{\text{min}} = \{0.28, 0.36, 0.44, 0.6\} \quad \text{for } z = \{0, 0.5, 1.0, 2.4\}. \quad (\text{H.19})$$

<sup>24</sup>The plot is obtained using the full expressions (H.10), (H.11), (H.6), (H.13). It is well described by the approximate formula (H.17).

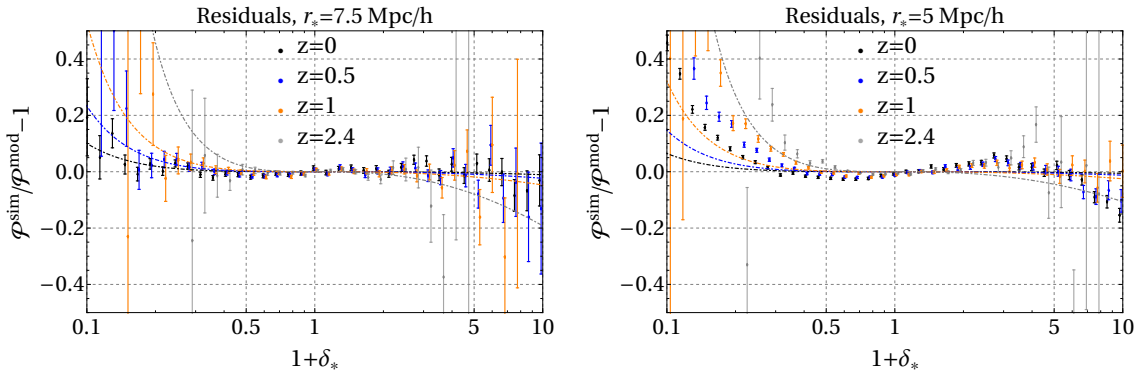


**Figure 23.** The systematic bias in the PDF due to Zeldovich initial conditions (dotted lines). We also show the residuals between N-body data and the theoretical model of the main text (cf. lower panels of Fig. 13). Note that for  $r_* = 5$  Mpc/h (right panel) the model has been constructed by fitting the data in the range  $(1 + \delta_*) > (1 + \delta_*)_{\min}$  with  $(1 + \delta_*)_{\min}$  listed in Eq. (H.19).

A comment is in order. For cells with  $r_* = 5$  Mpc/h the estimate (H.18) correctly captures the qualitative trend of the residuals. However, it cannot fully account for their magnitude, underpredicting them by a factor of a few at strong underdensities. It is important to investigate the origin of this additional discrepancy. There are at least three logical possibilities: large corrections from ZIC to the PDF prefactor; large higher-order corrections to the PDF model; or unknown systematics in the N-body data. We leave this question for future. In this respect it is worth noting that using 2LPT initial conditions, instead of ZIC, strongly suppresses the effects of transients in the simulations [46, 91].

## I Reduced models for counterterm prefactor

In Sec. 4 we have formulated the model for counterterm prefactor with three free fitting parameters: the scaling index  $m$  and the kinetic and potential counterterm amplitudes  $\zeta^{\text{kin}}$ ,  $\zeta^{\text{pot}}$ . In Sec. 5 we have shown that this model well describes the data of N-body simulations. Here we explore the possibility of fitting PDF with a reduced number of parameters by imposing constraints on  $(m, \zeta^{\text{kin}}, \zeta^{\text{pot}})$ . We also comment on the relation of our model to Model 2 of Ref. [71].

As a first test, we perform the fitting procedure when setting either the kinetic or potential counterterm amplitude to zero. The residuals of the fits for the cell radius  $r_* = 10$  Mpc/h are shown in Fig. 24. We found that the both models capture the behaviour of the PDF fairly well. The good quality of the fit is confirmed by the values of  $\chi^2$  listed in Tab. 6. However, the predictions of model parameters deviate significantly. In particular, the value of  $\zeta^{\text{kin}}$  extracted from the  $\zeta^{\text{pot}} = 0$  fit differs from the result using the full theoretical PDF model by more than  $3\sigma$ . Also,

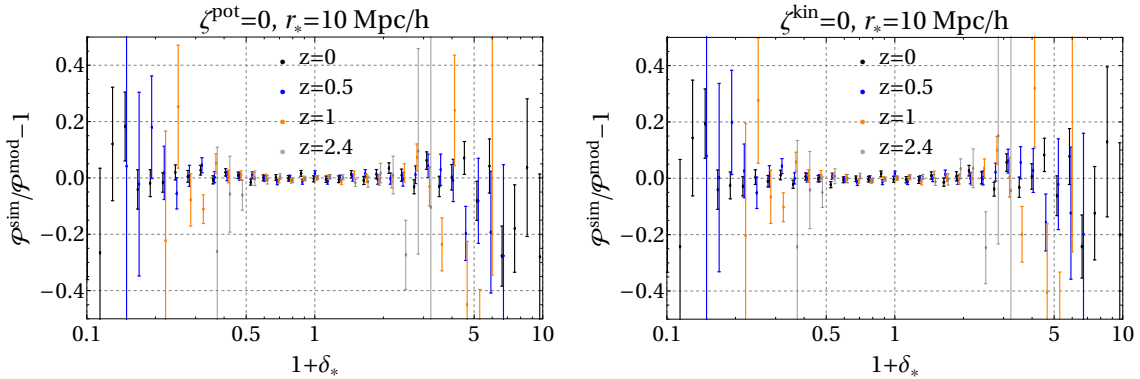


**Figure 24.** Residuals between the PDF extracted from N-body data and the reduced theoretical model with  $\zeta^{\text{pot}} = 0$  (*left*) and  $\zeta^{\text{kin}} = 0$  (*right*) for cell radius  $r_* = 10 \text{ Mpc}/h$ .

Model	$m$	$\zeta^{\text{kin}}$	$\zeta^{\text{pot}}$	$\chi^2/N_{\text{dof}}$	$\gamma_0$
Baseline	$2.14 \pm 0.10$	$0.48 \pm 0.29$	$-2.03 \pm 0.69$	108/110	$1.73 \pm 0.08$
$\zeta^{\text{pot}} = 0$	$2.42 \pm 0.05$	$1.42 \pm 0.06$	—	118/111	$1.95 \pm 0.06$
$\zeta^{\text{kin}} = 0$	$1.97 \pm 0.04$	—	$-3.23 \pm 0.11$	111/111	$1.63 \pm 0.05$
$\zeta^{\text{kin}} = \zeta^{\text{pot}}$	$2.63 \pm 0.07$	$2.68 \pm 0.18$	$2.68 \pm 0.18$	185/111	$2.22 \pm 0.08$

**Table 6.** Best fit parameters of the counterterm models,  $\chi^2$  per number of degrees of freedom, and the derived effective speed of sound  $\gamma_0$ .

the values of  $m$  and  $\gamma_0$  are systematically higher for this fit than in the baseline analysis. The fit  $\zeta^{\text{kin}} = 0$  is closer to the baseline model but gives lower values of  $m$ ,  $\gamma_0$  which are mildly in tension with the ranges extracted from the power spectrum (see Eq. (5.2)).

As a second test, we consider the equal counterterm amplitudes,  $\zeta^{\text{kin}} = \zeta^{\text{pot}}$ . This choice takes place if one renormalizes the stress tensor for short-scale contributions as the whole without splitting the latter into the kinetic and potential parts. The results listed in Tab. 6 reflect that this reduced model fails to reproduce the data with required precision. In particular, it leads to a severe  $4.4\sigma$  tension with the N-body data. It is thus impossible to describe the counterterm stress with a single coefficient. This result confirms that the kinetic and potential counterterms are physically distinct. We do not see any firm reason to discard any of them and recommend keeping  $\zeta^{\text{kin}}$ ,  $\zeta^{\text{pot}}$  as independent free parameters.

Incidentally, the model with  $\zeta^{\text{pot}} = 0$  happens to give a counterterm prefactor similar to Model 2 of Ref. [71]. The latter was proposed as an ad hoc way to take into account the dependence of the shell-crossing scale on the mean density of the cell. In more detail, the counterterm prefactor of Model 2 reads,

$$\mathcal{A}^{\text{ctr}(2)} = \exp\left(-\frac{315\gamma_0}{122\pi}\left(\frac{g(z)}{F'(\delta_*)(1+\delta_*)}\right)^{m-2} \times 2\hat{\lambda} \int \frac{d\mathcal{X}}{\mathcal{X}} q(\mathcal{X})\right), \quad (\text{I.1})$$

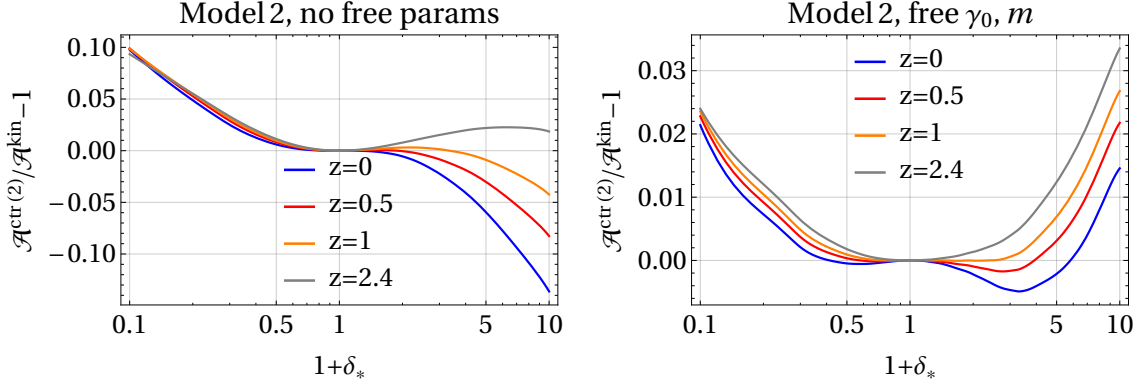


**Figure 25.** The difference between the counterterm prefactor (I.1) from Model 2 of [71] and reduced theoretical model of this paper with  $\zeta^{\text{pot}} = 0$  for cell radius  $r_* = 10 \text{ Mpc}/h$  at various redshifts. *Left:* the parameters of Model 2 are fixed to  $m = 8/3$ ,  $\gamma_0 = 1.95$ . *Right:*  $(m, \gamma_0)$  are fitted from the PDF data with correlated Gaussian priors inferred from the power spectrum fit.

where  $q(\mathcal{z})$  is the WKB function appearing in the short-mode contribution to the prefactor, Eq. (2.25). Following [71], Model 2 uses as input the value  $\gamma_0$  from the fit of the power spectrum and  $m = 8/3$ , and thus does not introduce any new fitting parameters. The ratio between  $\mathcal{A}^{\text{ctr}(2)}$  computed in this way and the best-fit counterterm prefactor with  $\zeta^{\text{pot}} = 0$  is shown on the left panel of Fig. 25. We see that the difference between two models is only about 10% at the tails. As a result, the Model 2 without any free parameters describes the data fairly well, with only a weak  $1.8\sigma$  tension, as follows from the value of  $\chi^2$  listed in the upper row of Table 7. We do not have any physical explanation of this quantitative success. It would be

Model 2	$m$	$\gamma_0$	$\chi^2/N_{\text{dof}}$
No free params	8/3	1.95	134/112
Free $\gamma_0$	8/3	$1.97 \pm 0.06$	134/112
Free $\gamma_0, m$	$2.48 \pm 0.04$	$2.03 \pm 0.06$	120/111

**Table 7.** Parameters of the counterterm prefactor (I.1) from Model 2 of [71] and the quality of the fit to N-body data. Three cases are considered: fixed parameters (first row), one free fitting parameter  $\gamma_0$  (second row), and two free parameters  $\gamma_0, m$  (third row).

interesting to understand if it persists for more general cosmologies, such as, e.g., scaling universes, or is a pure accident of  $\Lambda\text{CDM}$ .

In the spirit of EFT approach to PDF, we can allow the parameters of Model 2 to be determined from the PDF data themselves. A natural extension is to set  $\gamma_0$  as a free parameter. We fit  $\gamma_0$  to the aspherical prefactor extracted from simulations using the procedure described in Sec. 5. We impose the Gaussian prior on  $\gamma_0$  from

the fit of the power spectrum (5.2). The results are presented in the second row of Tab. 7. The quality of the fit does not change and the value of  $\gamma_0$  is entirely consistent with the result inferred from the power spectrum.

Moving one step further we let both parameters ( $m, \gamma_0$ ) to vary freely in the fit. We impose correlated Gaussian priors following from the fit of the power spectrum (5.2). The results listed in Tab. 7 reflect that the quality of the fit improves compared to that in the  $m = 8/3$  scenarios. In particular, Model 2 with free ( $m, \gamma_0$ ) is in  $1.1\sigma$  agreement with the data.<sup>25</sup> On the right of Fig. 25 we plot the relative difference between the best-fit Model 2 (I.1) and the  $\zeta^{\text{pot}} = 0$  result for different redshifts. We find that the Model 2 with free ( $m, \gamma_0$ ) reproduces the kinetic counterterm prefactor with a few per cent precision.

## References

- [1] F. Bernardeau, S. Colombi, E. Gaztanaga and R. Scoccimarro, *Large scale structure of the universe and cosmological perturbation theory*, *Phys. Rept.* **367** (2002) 1 [[astro-ph/0112551](#)].
- [2] D. Baumann, A. Nicolis, L. Senatore and M. Zaldarriaga, *Cosmological Non-Linearities as an Effective Fluid*, *JCAP* **07** (2012) 051 [[1004.2488](#)].
- [3] J. J. M. Carrasco, M. P. Hertzberg and L. Senatore, *The Effective Field Theory of Cosmological Large Scale Structures*, *JHEP* **09** (2012) 082 [[1206.2926](#)].
- [4] E. Pajer and M. Zaldarriaga, *On the Renormalization of the Effective Field Theory of Large Scale Structures*, *JCAP* **08** (2013) 037 [[1301.7182](#)].
- [5] T. Baldauf, L. Mercolli, M. Mirbabayi and E. Pajer, *The Bispectrum in the Effective Field Theory of Large Scale Structure*, *JCAP* **05** (2015) 007 [[1406.4135](#)].
- [6] A. A. Abolhasani, M. Mirbabayi and E. Pajer, *Systematic Renormalization of the Effective Theory of Large Scale Structure*, *JCAP* **05** (2016) 063 [[1509.07886](#)].
- [7] G. Cabass, M. M. Ivanov, M. Lewandowski, M. Mirbabayi and M. Simonović, *Snowmass white paper: Effective field theories in cosmology*, *Phys. Dark Univ.* **40** (2023) 101193 [[2203.08232](#)].
- [8] M. M. Ivanov, *Effective Field Theory for Large Scale Structure*, [2212.08488](#).
- [9] L. Senatore and M. Zaldarriaga, *The IR-resummed Effective Field Theory of Large Scale Structures*, *JCAP* **02** (2015) 013 [[1404.5954](#)].
- [10] T. Baldauf, M. Mirbabayi, M. Simonović and M. Zaldarriaga, *Equivalence Principle and the Baryon Acoustic Peak*, *Phys. Rev. D* **92** (2015) 043514 [[1504.04366](#)].
- [11] D. Blas, M. Garny, M. M. Ivanov and S. Sibiryakov, *Time-Sliced Perturbation Theory II: Baryon Acoustic Oscillations and Infrared Resummation*, *JCAP* **07** (2016) 028 [[1605.02149](#)].

---

<sup>25</sup>For comparison, the baseline theoretical model of this paper shows  $0.6\sigma$  agreement.

- [12] M. M. Ivanov and S. Sibiryakov, *Infrared Resummation for Biased Tracers in Redshift Space*, *JCAP* **07** (2018) 053 [[1804.05080](#)].
- [13] M. Simonović, T. Baldauf, M. Zaldarriaga, J. J. Carrasco and J. A. Kollmeier, *Cosmological perturbation theory using the FFTLog: formalism and connection to QFT loop integrals*, *JCAP* **04** (2018) 030 [[1708.08130](#)].
- [14] T. Nishimichi, G. D’Amico, M. M. Ivanov, L. Senatore, M. Simonović, M. Takada et al., *Blinded challenge for precision cosmology with large-scale structure: results from effective field theory for the redshift-space galaxy power spectrum*, *Phys. Rev. D* **102** (2020) 123541 [[2003.08277](#)].
- [15] T. Steele and T. Baldauf, *Precise Calibration of the One-Loop Bispectrum in the Effective Field Theory of Large Scale Structure*, *Phys. Rev. D* **103** (2021) 023520 [[2009.01200](#)].
- [16] O. H. E. Philcox, M. M. Ivanov, G. Cabass, M. Simonović, M. Zaldarriaga and T. Nishimichi, *Cosmology with the redshift-space galaxy bispectrum monopole at one-loop order*, *Phys. Rev. D* **106** (2022) 043530 [[2206.02800](#)].
- [17] G. D’Amico, L. Senatore and P. Zhang, *Limits on  $w$ CDM from the EFTofLSS with the PyBird code*, *JCAP* **01** (2021) 006 [[2003.07956](#)].
- [18] A. Chudaykin, M. M. Ivanov, O. H. E. Philcox and M. Simonović, *Nonlinear perturbation theory extension of the Boltzmann code CLASS*, *Phys. Rev. D* **102** (2020) 063533 [[2004.10607](#)].
- [19] S.-F. Chen, Z. Vlah, E. Castorina and M. White, *Redshift-Space Distortions in Lagrangian Perturbation Theory*, *JCAP* **03** (2021) 100 [[2012.04636](#)].
- [20] M. M. Ivanov, M. Simonović and M. Zaldarriaga, *Cosmological Parameters from the BOSS Galaxy Power Spectrum*, *JCAP* **05** (2020) 042 [[1909.05277](#)].
- [21] G. D’Amico, J. Gleyzes, N. Kokron, K. Markovic, L. Senatore, P. Zhang et al., *The Cosmological Analysis of the SDSS/BOSS data from the Effective Field Theory of Large-Scale Structure*, *JCAP* **05** (2020) 005 [[1909.05271](#)].
- [22] M. M. Ivanov, M. Simonović and M. Zaldarriaga, *Cosmological Parameters and Neutrino Masses from the Final Planck and Full-Shape BOSS Data*, *Phys. Rev. D* **101** (2020) 083504 [[1912.08208](#)].
- [23] T. Colas, G. D’Amico, L. Senatore, P. Zhang and F. Beutler, *Efficient Cosmological Analysis of the SDSS/BOSS data from the Effective Field Theory of Large-Scale Structure*, *JCAP* **06** (2020) 001 [[1909.07951](#)].
- [24] O. H. E. Philcox, M. M. Ivanov, M. Simonović and M. Zaldarriaga, *Combining Full-Shape and BAO Analyses of Galaxy Power Spectra: A 1.6% CMB-independent constraint on  $H_0$* , *JCAP* **05** (2020) 032 [[2002.04035](#)].
- [25] A. Chudaykin, K. Dolgikh and M. M. Ivanov, *Constraints on the curvature of the Universe and dynamical dark energy from the Full-shape and BAO data*, *Phys. Rev. D* **103** (2021) 023507 [[2009.10106](#)].

- [26] G. D’Amico, Y. Donath, L. Senatore and P. Zhang, *Limits on Clustering and Smooth Quintessence from the EFTofLSS*, [2012.07554](#).
- [27] M. M. Ivanov, *Cosmological constraints from the power spectrum of eBOSS emission line galaxies*, *Phys. Rev. D* **104** (2021) 103514 [[2106.12580](#)].
- [28] S.-F. Chen, Z. Vlah and M. White, *A new analysis of galaxy 2-point functions in the BOSS survey, including full-shape information and post-reconstruction BAO*, *JCAP* **02** (2022) 008 [[2110.05530](#)].
- [29] M. White et al., *Cosmological constraints from the tomographic cross-correlation of DESI Luminous Red Galaxies and Planck CMB lensing*, *JCAP* **02** (2022) 007 [[2111.09898](#)].
- [30] O. H. E. Philcox and M. M. Ivanov, *BOSS DR12 full-shape cosmology:  $\Lambda$ CDM constraints from the large-scale galaxy power spectrum and bispectrum monopole*, *Phys. Rev. D* **105** (2022) 043517 [[2112.04515](#)].
- [31] S.-F. Chen, M. White, J. DeRose and N. Kokron, *Cosmological analysis of three-dimensional BOSS galaxy clustering and Planck CMB lensing cross correlations via Lagrangian perturbation theory*, *JCAP* **07** (2022) 041 [[2204.10392](#)].
- [32] G. Cabass, M. M. Ivanov, O. H. E. Philcox, M. Simonović and M. Zaldarriaga, *Constraints on Single-Field Inflation from the BOSS Galaxy Survey*, *Phys. Rev. Lett.* **129** (2022) 021301 [[2201.07238](#)].
- [33] G. Cabass, M. M. Ivanov, O. H. E. Philcox, M. Simonović and M. Zaldarriaga, *Constraints on multifield inflation from the BOSS galaxy survey*, *Phys. Rev. D* **106** (2022) 043506 [[2204.01781](#)].
- [34] G. Cabass, M. M. Ivanov and O. H. E. Philcox, *Colliders and ghosts: Constraining inflation with the parity-odd galaxy four-point function*, *Phys. Rev. D* **107** (2023) 023523 [[2210.16320](#)].
- [35] A. Chudaykin and M. M. Ivanov, *Cosmological constraints from the power spectrum of eBOSS quasars*, *Phys. Rev. D* **107** (2023) 043518 [[2210.17044](#)].
- [36] T. Baldauf, M. Mirbabayi, M. Simonović and M. Zaldarriaga, *LSS constraints with controlled theoretical uncertainties*, [1602.00674](#).
- [37] A. Chudaykin and M. M. Ivanov, *Measuring neutrino masses with large-scale structure: Euclid forecast with controlled theoretical error*, *JCAP* **11** (2019) 034 [[1907.06666](#)].
- [38] A. Chudaykin, M. M. Ivanov and M. Simonović, *Optimizing large-scale structure data analysis with the theoretical error likelihood*, *Phys. Rev. D* **103** (2021) 043525 [[2009.10724](#)].
- [39] E. Hubble, *The Distribution of Extra-Galactic Nebulae*, *Astrophys. J.* **79** (1934) 8.
- [40] 2DFGRS collaboration, V. Wild et al., *The 2dF Galaxy Redshift Survey: Stochastic relative biasing between galaxy populations*, *Mon. Not. Roy. Astron. Soc.* **356** (2005)

247 [[astro-ph/0404275](#)].

- [41] L. Hurtado-Gil, V. J. Martínez, P. Arnalte-Mur, M. J. Pons-Bordería, C. Pareja-Flores and S. Paredes, *The best fit for the observed galaxy Counts-in-Cell distribution function*, *Astron. Astrophys.* **601** (2017) A40 [[1703.01087](#)].
- [42] A. Repp and I. Szapudi, *Galaxy Bias and  $\sigma_8$  from Counts in Cells from the SDSS Main Sample*, *Mon. Not. Roy. Astron. Soc.* **498** (2020) L125 [[2006.01146](#)].
- [43] DES collaboration, L. Clerkin et al., *Testing the lognormality of the galaxy and weak lensing convergence distributions from Dark Energy Survey maps*, *Mon. Not. Roy. Astron. Soc.* **466** (2017) 1444 [[1605.02036](#)].
- [44] DES collaboration, D. Gruen et al., *Density Split Statistics: Cosmological Constraints from Counts and Lensing in Cells in DES Y1 and SDSS Data*, *Phys. Rev. D* **98** (2018) 023507 [[1710.05045](#)].
- [45] P. A. Burger et al., *KiDS-1000 cosmology: Constraints from density split statistics*, *Astron. Astrophys.* **669** (2023) A69 [[2208.02171](#)].
- [46] C. Uhlemann, O. Friedrich, F. Villaescusa-Navarro, A. Banerjee and S. Codis, *Fisher for complements: Extracting cosmology and neutrino mass from the counts-in-cells PDF*, *Mon. Not. Roy. Astron. Soc.* **495** (2020) 4006 [[1911.11158](#)].
- [47] M. Cataneo, C. Uhlemann, C. Arnold, A. Gough, B. Li and C. Heymans, *The matter density PDF for modified gravity and dark energy with Large Deviations Theory*, *Mon. Not. Roy. Astron. Soc.* **513** (2022) 1623 [[2109.02636](#)].
- [48] A. Gough and C. Uhlemann, *One-Point Statistics Matter in Extended Cosmologies*, *Universe* **8** (2022) 55 [[2112.04428](#)].
- [49] D. Jamieson and M. Loverde, *The position-dependent matter density probability distribution function*, *Phys. Rev. D* **102** (2020) 123546 [[2010.07235](#)].
- [50] S. Matarrese, L. Verde and R. Jimenez, *The Abundance of high-redshift objects as a probe of non-Gaussian initial conditions*, *Astrophys. J.* **541** (2000) 10 [[astro-ph/0001366](#)].
- [51] O. Friedrich, C. Uhlemann, F. Villaescusa-Navarro, T. Baldauf, M. Manera and T. Nishimichi, *Primordial non-Gaussianity without tails – how to measure  $f_{NL}$  with the bulk of the density PDF*, *Mon. Not. Roy. Astron. Soc.* **498** (2020) 464 [[1912.06621](#)].
- [52] O. Leicht, C. Uhlemann, F. Villaescusa-Navarro, S. Codis, L. Hernquist and S. Genel, *Extreme Spheres: Counts-in-cells for 21cm intensity mapping*, *Mon. Not. Roy. Astron. Soc.* **484** (2019) 269 [[1808.09968](#)].
- [53] F. Bernardeau, *The Gravity induced quasi-Gaussian correlation hierarchy*, *Astrophys. J.* **392** (1992) 1.
- [54] F. Bernardeau, *The Nonlinear evolution of rare events*, *Astrophys. J.* **427** (1994) 51 [[astro-ph/9311066](#)].

- [55] P. Valageas, *Dynamics of gravitational clustering. 2. Steepest-descent method for the quasi-linear regime*, *Astron. Astrophys.* **382** (2002) 412 [[astro-ph/0107126](#)].
- [56] P. Valageas, *Dynamics of gravitational clustering v. subleading corrections in the quasi-linear regime*, *Astron. Astrophys.* **382** (2002) 477 [[astro-ph/0109408](#)].
- [57] F. Bernardeau, C. Pichon and S. Codis, *Statistics of cosmic density profiles from perturbation theory*, *Phys. Rev. D* **90** (2014) 103519 [[1310.8134](#)].
- [58] F. Bernardeau and P. Reimberg, *Large deviation principle at play in large scale structure cosmology*, *Phys. Rev. D* **94** (2016) 063520 [[1511.08641](#)].
- [59] C. Uhlemann, S. Codis, C. Pichon, F. Bernardeau and P. Reimberg, *Back in the saddle: Large-deviation statistics of the cosmic log-density field*, *Mon. Not. Roy. Astron. Soc.* **460** (2016) 1529 [[1512.05793](#)].
- [60] C. Uhlemann, E. Pajer, C. Pichon, T. Nishimichi, S. Codis and F. Bernardeau, *Hunting high and low: Disentangling primordial and late-time non-Gaussianity with cosmic densities in spheres*, *Mon. Not. Roy. Astron. Soc.* **474** (2018) 2853 [[1708.02206](#)].
- [61] A. Boyle, C. Uhlemann, O. Friedrich, A. Barthelemy, S. Codis, F. Bernardeau et al., *NuW CDM cosmology from the weak-lensing convergence PDF*, *Mon. Not. Roy. Astron. Soc.* **505** (2021) 2886 [[2012.07771](#)].
- [62] O. Friedrich, A. Halder, A. Boyle, C. Uhlemann, D. Britt, S. Codis et al., *The PDF perspective on the tracer-matter connection: Lagrangian bias and non-Poissonian shot noise*, *Mon. Not. Roy. Astron. Soc.* **510** (2022) 5069 [[2107.02300](#)].
- [63] A. G. Doroshkevich, *Spatial structure of perturbations and origin of galactic rotation in fluctuation theory*, *Astrophysics* **6** (1970) 320.
- [64] L. Hui, L. Kofman and S. F. Shandarin, *Multiple-streaming and the probability distribution of density in redshift space*, *Astrophys. J.* **537** (2000) 12 [[astro-ph/9901104](#)].
- [65] R. K. Sheth, *An Excursion set model for the distribution of dark matter and dark matter halos*, *Mon. Not. Roy. Astron. Soc.* **300** (1998) 1057 [[astro-ph/9805319](#)].
- [66] J. Betancort-Rijo and M. Lopez-Corredoira, *Probability distribution of density fluctuations in the nonlinear regime*, *Astrophys. J.* **566** (2002) 623 [[astro-ph/0110624](#)].
- [67] T. Y. Lam and R. K. Sheth, *Perturbation theory and excursion set estimates of the probability distribution function of dark matter, and a method for reconstructing the initial distribution function*, *Mon. Not. Roy. Astron. Soc.* **386** (2008) 407 [[0711.5029](#)].
- [68] A. Paranjape, T. Y. Lam and R. K. Sheth, *Halo abundances and counts-in-cells: The excursion set approach with correlated steps*, *Mon. Not. Roy. Astron. Soc.* **420** (2012) 1429 [[1105.1990](#)].

- [69] M. Musso and R. K. Sheth, *One step beyond: The excursion set approach with correlated steps*, *Mon. Not. Roy. Astron. Soc.* **423** (2012) L102 [[1201.3876](#)].
- [70] E. Pajer and D. van der Woude, *Divergence of Perturbation Theory in Large Scale Structures*, *JCAP* **05** (2018) 039 [[1710.01736](#)].
- [71] M. M. Ivanov, A. A. Kaurov and S. Sibiryakov, *Non-perturbative probability distribution function for cosmological counts in cells*, *JCAP* **03** (2019) 009 [[1811.07913](#)].
- [72] <https://github.com/Michalychforever/AsPy>.
- [73] HACC collaboration, N. Frontiere, K. Heitmann, E. Rangel, P. Larsen, A. Pope, I. Sultan et al., *Farpoint: A High-resolution Cosmology Simulation at the Gigaparsec Scale*, *Astrophys. J. Supp.* **259** (2022) 15 [[2109.01956](#)].
- [74] D. Blas, M. Garny, M. M. Ivanov and S. Sibiryakov, *Time-Sliced Perturbation Theory for Large Scale Structure I: General Formalism*, *JCAP* **07** (2016) 052 [[1512.05807](#)].
- [75] F. Bernardeau, *The Effects of smoothing on the statistical properties of large scale cosmic fields*, *Astron. Astrophys.* **291** (1994) 697 [[astro-ph/9403020](#)].
- [76] P. Fosalba and E. Gaztanaga, *Cosmological perturbation theory and the spherical collapse model: Part 1. Gaussian initial conditions*, *Mon. Not. Roy. Astron. Soc.* **301** (1998) 503 [[astro-ph/9712095](#)].
- [77] J. J. M. Carrasco, S. Foreman, D. Green and L. Senatore, *The Effective Field Theory of Large Scale Structures at Two Loops*, *JCAP* **07** (2014) 057 [[1310.0464](#)].
- [78] R. E. Angulo, S. Foreman, M. Schmittfull and L. Senatore, *The One-Loop Matter Bispectrum in the Effective Field Theory of Large Scale Structures*, *JCAP* **10** (2015) 039 [[1406.4143](#)].
- [79] S. Foreman and L. Senatore, *The EFT of Large Scale Structures at All Redshifts: Analytical Predictions for Lensing*, *JCAP* **04** (2016) 033 [[1503.01775](#)].
- [80] T. Baldauf, L. Mercolli and M. Zaldarriaga, *Effective field theory of large scale structure at two loops: The apparent scale dependence of the speed of sound*, *Phys. Rev. D* **92** (2015) 123007 [[1507.02256](#)].
- [81] T. Lazeyras and F. Schmidt, *A robust measurement of the first higher-derivative bias of dark matter halos*, *JCAP* **11** (2019) 041 [[1904.11294](#)].
- [82] S. Pueblas and R. Scoccimarro, *Generation of Vorticity and Velocity Dispersion by Orbit Crossing*, *Phys. Rev. D* **80** (2009) 043504 [[0809.4606](#)].
- [83] D. Blas, J. Lesgourgues and T. Tram, *The Cosmic Linear Anisotropy Solving System (CLASS) II: Approximation schemes*, *JCAP* **07** (2011) 034 [[1104.2933](#)].
- [84] K. Yamamoto, M. Nakamichi, A. Kamino, B. A. Bassett and H. Nishioka, *A Measurement of the quadrupole power spectrum in the clustering of the 2dF QSO Survey*, *Publ. Astron. Soc. Jap.* **58** (2006) 93 [[astro-ph/0505115](#)].
- [85] N. Hand, Y. Feng, F. Beutler, Y. Li, C. Modi, U. Seljak et al., *nbodykit: an*

- open-source, massively parallel toolkit for large-scale structure*, *Astron. J.* **156** (2018) 160 [[1712.05834](#)].
- [86] F. Villaescusa-Navarro et al., *The Quijote simulations*, *Astrophys. J. Suppl.* **250** (2020) 2 [[1909.05273](#)].
- [87] A. Repp and I. Szapudi, *The Variance and Covariance of Counts-in-Cells Probabilities*, *Mon. Not. Roy. Astron. Soc.* **500** (2020) 3631 [[2007.00011](#)].
- [88] F. Bernardeau, *Covariances of density probability distribution functions. Lessons from hierarchical models*, *Astron. Astrophys.* **663** (2022) A124 [[2207.02500](#)].
- [89] C. Uhlemann, O. Friedrich, A. Boyle, A. Gough, A. Barthelemy, F. Bernardeau et al., *It takes two to know one: Computing accurate one-point PDF covariances from effective two-point PDF models*, *Open J. Astrophys.* **6** (2022) 2023 [[2210.07819](#)].
- [90] R. Scoccimarro, *Transients from initial conditions: a perturbative analysis*, *Mon. Not. Roy. Astron. Soc.* **299** (1998) 1097 [[astro-ph/9711187](#)].
- [91] M. Crocce, S. Pueblas and R. Scoccimarro, *Transients from Initial Conditions in Cosmological Simulations*, *Mon. Not. Roy. Astron. Soc.* **373** (2006) 369 [[astro-ph/0606505](#)].
- [92] C. Uhlemann, S. Codis, O. Hahn, C. Pichon and F. Bernardeau, *Two is better than one: joint statistics of density and velocity in concentric spheres as a cosmological probe*, *Mon. Not. Roy. Astron. Soc.* **469** (2017) 2481 [[1612.00019](#)].
- [93] A. Boyle, A. Barthelemy, S. Codis, C. Uhlemann and O. Friedrich, *The cumulant generating function as a novel observable to cumulate weak lensing information*, [2212.10351](#).
- [94] A. Banerjee and T. Abel, *Nearest neighbour distributions: New statistical measures for cosmological clustering*, *Mon. Not. Roy. Astron. Soc.* **500** (2020) 5479 [[2007.13342](#)].
- [95] A. Banerjee, N. Kokron and T. Abel, *Modelling nearest neighbour distributions of biased tracers using hybrid effective field theory*, *Mon. Not. Roy. Astron. Soc.* **511** (2022) 2765 [[2107.10287](#)].
- [96] S. Contarini, A. Pisani, N. Hamaus, F. Marulli, L. Moscardini and M. Baldi, *Cosmological constraints from the BOSS DR12 void size function*, [2212.03873](#).
- [97] J. Kim, C. Park, G. Rossi, S. M. Lee and J. R. Gott, III, *The New Horizon Run Cosmological N-Body Simulations*, *J. Korean Astron. Soc.* **44** (2011) 217 [[1112.1754](#)].
- [98] D. J. Eisenstein and W. Hu, *Power spectra for cold dark matter and its variants*, *Astrophys. J.* **511** (1997) 5 [[astro-ph/9710252](#)].
- [99] P. Valageas, *Transients from Zeldovich initial conditions*, *Astron. Astrophys.* **385** (2002) 761 [[astro-ph/0112102](#)].